CONTENTS

Technical Papers

Announcements by IJASC :
Announcement for SDSS 2016
Announcement for ICMS 2016
Announcement for ICSAS 2016

Cover: *1000ton+ temporary steel platform in support of heavy-duty mobile cranes, designed by second-order direct analysis without effective length*

e-copy of IJASC is free to download at "www.ascjournal.com" in internet and mobile apps.

Editors-in-Chief

S.L. Chan, *The Hong Kong Polytechnic University, Hong Kong*

W.F. Chen, *University of Hawaii at Manoa, USA*

R. Zandonini, *Trento University, Italy*

Cover: 1000ton+ temporary steel platform in support of heavy-duty mobile cranes, designed by second-order direct analysis without effective length

e-copy of IJASC is free to download at "www.ascjournal.com" in internet and mobile apps.

Advanced Steel Construction
an international journal

EDITORS-IN-CHIEF

Asian Pacific, African
and organizing Editor
S.L. Chan
*The Hong Kong Polyt. Univ.,
Hong Kong*
Email: ceslchan@polyu.edu.hk

American Editor
W.F. Chen
Univ. of Hawaii at Manoa, USA
Email: waifah@hawaii.edu

European Editor
R. Zandonini
Trento Univ., Italy
Email: riccardo.zandonini@ing.unitn.it

VOLUME 12   NUMBER 1   **MARCH 2016**

Technical Papers

Announcements by IJASC :

Announcement for SDSS 2016
Announcement for ICMS 2016
Announcement for ICSAS 2016

WIND-INDUCED RESPONSE OF LARGE-SPAN STRUCTURES BASED ON POD-PSEUDO-EXCITATION METHOD

Zhongwei Zhao [2], Zhihua Chen [1,2,3], Xiaodun Wang [2, *], HaoXu [2] and Hongbo Liu [2]

[1] *State Key Laboratory of Hydraulic Engineering Simulation and Safety,*
Tianjin University, Tianjin 300072, China
[2] *School of Civil Engineering, Tianjin University, Tianjin 300072, China;*
[3] *Key Laboratory of Coast Civil Structure and Safety of Ministry of Education, Tianjin University,*
Tianjin 300072, China;
*(Corresponding author: E-mail:maodun2004@126.com)

ABSTRACT: This paper proposes a new method to analyze wind-induced response in frequency domain for long-span spatial structures. This method is based on proper orthogonal decomposition (POD) and pseudo-excitation methods, which could significantly reduce computational cost. Based on the POD-pseudo-excitation method and the wind pressure coefficient obtained from a wind tunnel test, ANSYS general purpose software package was developed for the analysis of wind-induced response of YUJIAPU Railway Station Building, which is designed in the form of a conch-shaped single-layer lattice shell. The wind vibration coefficient in wind direction of 0° was obtained. Results obtained by frequency- and time-domain methods were compared. The results were consistent with each other, establishing the foundation for further application of these methods in wind-induced analysis. The relationship between wind-induced response and the frequency of wind load was also determined. This paper provides effective guidance on equivalent wind load.

Keywords: POD-pseudo-excitation method, wind vibration coefficient, wind-induced response, harmonic response analysis, conch-shaped single-layer lattice shell

1. INTRODUCTION

Long-span roofs are widely used in large-scale buildings such as gymnasiums, exhibition centers, airports, and railway stations because such roofs provide a large space without inner columns and offer architects and designers an alternative to regular rectangular building forms. These kinds of roof structures comprise light materials with small damping ratios and low natural frequencies. They are sensitive to wind loading actions because of their light weight and small structural rigidity [1]. Wind-induced response analysis is an important and interesting issue for theoretical study and structural design.

Extensive studies have been conducted and remarkable developments have been achieved on wind resistance of long-span structures. The approach on the effects of wind loads on structures mainly includes time and frequency domain methods. Time–history curves must be obtained using a specified method. The time domain method is adopted because it is easy to understand and use. However, the method requires more computational resources, i.e., high cost and low efficiency. The advantage of the frequency domain method over time the domain method is its high calculation efficiency. The core problem in its application is that a number of modes of vibration rather than only the first mode must be considered in the analysis of wind-induced response particularly for long-span structures. Furthermore, the cross correlation terms between normal modes in a structural response [2], which are often ignored in previous studies, may have to be retained because long-span structures possess closely spaced natural frequencies and normal modes. Simultaneously,

the contribution of high-order modes of vibration to the response of structures is not always less than low-order modes.

YUJIAPU Railway Station building in Tianjin, China has an area of 86200 m². The three-story building with complex roof shapes has two basement floors. The station hall, including waiting and entrance halls, device rooms, and an office, is on the first floor. The platform with three island platforms and six arrival–departure tracks are on the second floor. The building has a conch-shaped single-layer lattice lighting roof. The main members of the entire structure are 72 curved steel box girders that intersect one another, as shown in Figure 4. Figure 5 shows the construction process of the station building that is 142 m in length and 80 m in width, and with vector height of 24 m. A ring beam was set on top and bottom of the shell to connect and constrain the steel box girders.

a)   b)

c)   d)
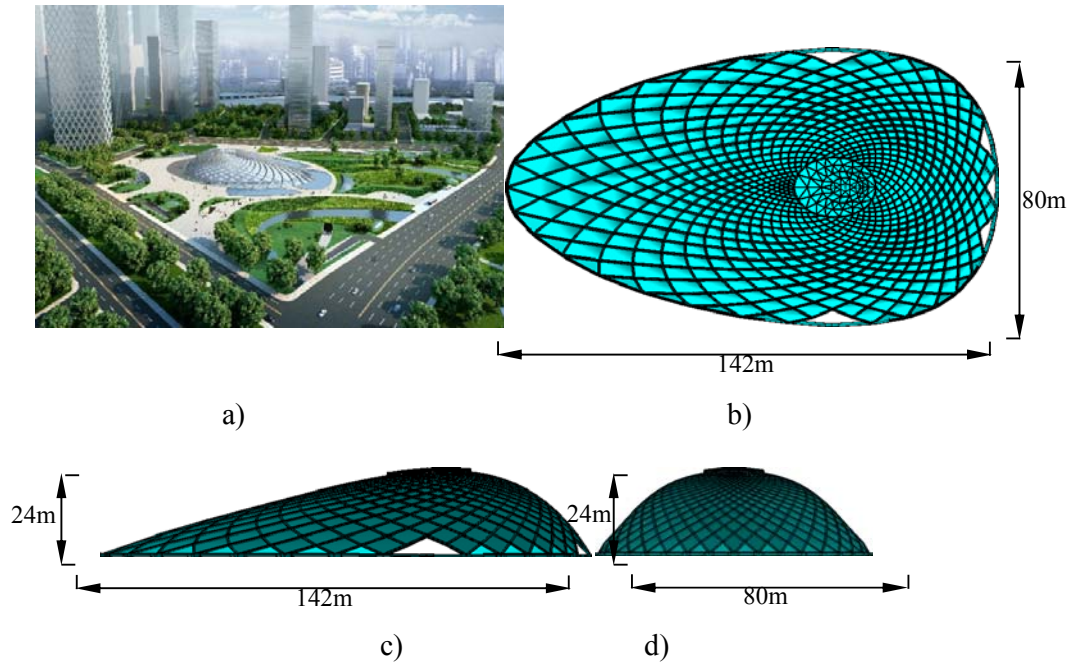
Figure 1. Details of the Structure. a) Aerial View of YUJIAPU Railway Station Building
b) Plan view, c) Lateral View, d) Front View

Studies have been conducted on wind-excited multi-story shear buildings and towers [3-4]. Zhou et al. [5] focused on the wind-induced vibration response of pre-stressed double-layer spherical latticed shell structures by adopting time-domain analysis method. Chen et al. [6] analyzed the wind-induced responses of long-span bridges by considering coupled multimode effect. Lin [7] proposed a pseudo-excitation method to address the dynamic response of structures subject to random seismic excitation. In this method, determining the random response of a structure is converted into finding the response of the structure under a series of harmonic loads, i.e., the so-called pseudo-excitations. Xu et al. [8] decomposed the excitation spectral matrix by LDLT method and analyzed the wind-induced response of high-rise structures. However, these methods are unsuitable for analysis of long-span spatial structures because of computational cost. The background response was significantly higher than the mean response and the resonant response; low-order eigenmodes and vibration modes provided the most important contributions to the wind-induced response [9]. Yang et al. [10] developed a program to analyze the wind-induced vibrations as a result of a combination of wind vibration modes, but did not consider the spatial distribution of wind load. The multi-mode coupling effect was considered in computing the resonant buffeting response and equivalent static wind loads. Zhou and Gu [11] used the modified

SRSS method, but the computational cost was high. Zhou [12] adopted the neural network method to predict the mean wind pressure coefficients and the power spectra of the fluctuating wind pressures on a real large-span roof based on the limited data from the wind tunnel test. However, the data from the wind tunnel test was extremely limited, affecting the accuracy of the neural network method. Yang [13] validated that the background responses were much larger than the resonant responses.

No method was highly efficient and accurate in wind induced analysis and can be conducted in the frequency domain for spatial structures. This paper provides a new method suitable for spatial structures, which can reduce computational cost significantly.

2.   ANALYSIS THEORY

2.1   Pseudo-excitation Method

The pseudo-excitation method proposed by Lin [7-9] was adopted to address the dynamic response of structures subject to random wind load. This method involves the cross-correlation terms between normal modes automatically and considers non-complete correlation among multi-support excitation. The method is equal to complete quadratic combination (CQC) in the mathematical sense, and the computational cost is much less than that of CQC, and even less than the square root of the sum of the squares (SRSS), which cannot consider the cross correlation terms between normal modes. The pseudo-excitation method proved to be an accurate and quick computing method.

Wind load acting on the building surface includes the mean wind loads F and the fluctuating wind loads $F(t)$. The equation of motion of a linear and elastic structure under the action of fluctuating wind forces $F(t)$ in terms of finite element technique can be expressed as

$$M\ddot{Y}(t) + C\dot{Y}(t) + KY(t) = RF(t) \tag{1}$$

where M, C, and K are the $N \times N$ system mass, damping, and stiffness matrices, respectively, $Y(t)$ is the displacement vector, $F(t)$ is the wind force vector of m dimension ($m \times N$), R is the $N \times m$ matrix consisting of 0 or 1, which expands the m-dimensional loading vector into the N-dimensional loading vector, and a dot represents the first-order derivative with respect to time t.

The Fourier transformation of Eq. 1 provides the transfer function between the loading and displacement response.

$$H(iw) = [-w^2M + iwC + K]^{-1} \tag{2}$$

where the superscript -1 indicates the matrix inversion and i is the imaginary unit.

Assuming that the power spectrum of wind load at a certain point is $S_f(w)$, we substitute this random excitation by pseudo harmonic excitation as expressed by Eq. 3.

$$x(t) = \sqrt{S_f(w)}e^{iwt} \tag{3}$$

The steady-state response of structures with certain natural vibration characteristics can be derived as

$$\{y\} = \sum_{j=1}^{q} \gamma_j H_j \{\phi_j\} \sqrt{S_f(w)} e^{iwt} \tag{4}$$

Furthermore, we obtain the power spectral density of response as

$$[S_{yy}(w)] = \{y\}^* \{y\}^T = \sum_{i=1}^{q} \sum_{j=1}^{q} \gamma_i \gamma_j H_i^* H_j \{\phi_i\} \{\phi_j\}^T S_f(w) \tag{5}$$

The pseudo-excitation method is validated to be equal to the CQC method.

2.2   Model of Wind Load Spectrum

This study uses the *Kaimal* wind speed spectrum, which can consider the effect of altitude change as fluctuating wind speed spectrum and is expressed as

$$\begin{cases} S_v(w) = \dfrac{200 u_*^2 \xi}{w(1+50\xi)^{5/3}} \\ u_* = k \bar{v}_{10} / ln(10/z_0), \xi = zw / \bar{v}_z \end{cases} \tag{6}$$

where k, z_0, $\bar{v}_{10}$, u_*, z, and α are *Kaimal* constant, the rough length of ground, mean wind speed of 10 m altitude, wind friction speed, and height of the wind speed, respectively; and w is the frequency of the wind speed.
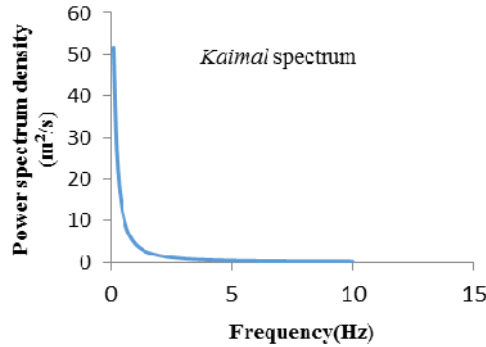
Figure 2. Wind Speed Spectrum at Node 2

The wind speed spectrum shows that the fluctuating wind contains minimal high-frequency components. We assume that the wind-induced response caused by high-frequency components is so small that we can neglect the response when the flexible long-span structures are subjected to high-frequency components. This study examines the relationship between wind-induced response and frequency of wind load to validate whether we can neglect this part of the response.

The wind speed and direction at each point is not synchronous and are even completely independent. The spatial correlation of gusty wind can be divided into lateral and vertical correlations, even before and after correlation. The tests indicate a negative correlation with decay with exponential rates and distance between two nodes. The cross power spectrum can consider this kind of correlation in actual engineering, and the cross power spectrum can be expressed as Eq. 7.

$$S_{vv}(w) = \begin{bmatrix} S_{v_1 v_1} & S_{v_1 v_2} & \cdots & S_{v_1 v_n} \\ S_{v_2 v_1} & S_{v_2 v_2} & \cdots & S_{v_2 v_n} \\ \vdots & \vdots & \ddots & \vdots \\ S_{v_n v_1} & S_{v_n v_2} & \cdots & S_{v_n v_n} \end{bmatrix} \qquad (7)$$

where

$$S_{v_i v_j}(x_1, x_2, y_1, y_2, z_1, z_2, w) = \rho_{ij}(x_1, x_2, y_1, y_2, z_1, z_2, w) \cdot \sqrt{S_{v_i}(x_1, y_1, z_1, w) S_{v_j}(x_1, y_1, z_1, w)} \qquad (8)$$

$$\rho_{ij}(x_1, x_2, y_1, y_2, w) = \exp\left(\frac{-2n \left[C_x^2 (x_i - x_j)^2 + C_y^2 (y_i - y_j)^2 + C_z^2 (z_i - z_j)^2 \right]}{\overline{v_i} + \overline{v_j}} \right) \qquad (9)$$

where $S_{v_i v_j}(x_1, x_2, y_1, y_2, w)$ is the cross power spectrum of nodes i and j; $\rho_{ij}(x_1, x_2, y_1, y_2, w)$ is coherence function; C_x, C_y, and C_z are constants equal to 16, 8, and 10, respectively; $\overline{v_i}$ and $\overline{v_j}$ are mean wind speed at nodes i and j.

2.3   Expression of Wind Load

Natural wind is classified according to frequency into mean and fluctuating winds. The effect of mean wind indicates that long period components are similar to static load, and the dynamic effect should be considered for fluctuating wind. Wind speed and the equivalent nodal load expressed by wind speed are as follows:

$$V(t) = \overline{v} + v(t) \qquad (10)$$

$$
\begin{aligned}
F_i(z,t) \\
= \frac{1}{2} \mu_{si} A_i \rho V^2(t) \\
= \frac{1}{2} \mu_{si} A_i \rho \overline{V}^2 + \mu_{si} A_i \rho \overline{V} v(z,t) + \frac{1}{2} \mu_{si} A_i \rho v(z,t)^2
\end{aligned}
\qquad (11)
$$

where $F_i(z,t)$, μ_{si}, A_i are nodal load, shape coefficient, and tributary area of node i, respectively. $v(z,t)$ is the wind speed at time t, and $\overline{v}$ is the mean wind speed at z altitude.

The first term in Eq. 11 is the equivalent nodal load caused by mean wind. As the fluctuating wind speed is extremely small compared to the mean wind speed, the third term can be ignored. Then, the equivalent nodal load, which is obtained based on quasi-steady assumption of node i can be expressed as follows [10]

$$f_i(t) = \mu_{si} A_i \rho \overline{V_i} v_i(t) = B_i v_i(t) \qquad (12)$$

where

$$B_i = \mu_{si} A_i \rho \overline{V_i} \qquad (13)$$

The direction of $f_i(t)$ is along the normal vector of the surface of structure. Then, $f_i(t)$ is decomposed along the global coordinate through which we obtain an equivalent nodal load expressed in three orthogonal directions.

$$\begin{Bmatrix} f_{ix}(t) \\ f_{iy}(t) \\ f_{iz}(t) \end{Bmatrix} = \begin{Bmatrix} B_i v_{ix}(t) \\ B_i v_{iy}(t) \\ B_i v_{iz}(t) \end{Bmatrix} = \{B_i\} \cdot * \begin{Bmatrix} v_{ix}(t) \\ v_{iy}(t) \\ v_{iz}(t) \end{Bmatrix} \tag{14}$$

where $v_{ix}(t) = \sqrt{v_i(t)^2} \cos\alpha$, $v_{iy}(t) = \sqrt{v_i(t)^2} \cos\beta$, $v_{iz}(t) = \sqrt{v_i(t)^2} \cos\gamma$, α, β, and γ are angles between the normal vector of surface and x-axis, y-axis, and z-axis of global coordinate, ' .* ' is matrix operator of MATLAB, indicating the multiplication of corresponding elements of two matrices with the same number of rows and columns.

The integration of Eq. 14 on all nodes can be written in matrix form as follows:

$$\{(t)\} = [Bv(t)\} \tag{15}$$

where $\{f(t)\} = \{f_{1x}(t), f_{1y}(t), f_{1z}(t) \cdots, f_{nx}(t), f_{ny}(t), f_{nz}(t)\}$ is a $3n \times 1$ matrix; $[B] = diag(\{B\})$ is a $3n \times 3n$ matrix; and $\{B\} = diag(\{B_i\})$, $\{v(t)\} = \{v_{1x}(t), v_{1y}(t), v_{1z}(t) \cdots, v_{nx}(t), v_{ny}(t), v_{nz}(t)\}$ is a $3n \times 1$ matrix.

2.4   Proper Decomposition Technique

Proper decomposition technique is an effective method to analyze random field. This method is used to obtain the intrinsic mode, which represents the spatial distribution pattern of fluctuating wind [14].

The main objective of the proper decomposition technique is to find deterministic function $\Phi(x, y)$, which is best correlated with all the elements of the ensemble of a random field. Given a random pressure $p(x, y, t)$, the maximum projection of $p(x, y, t)$ on the function $\Phi(x, y)$ is sought by considering an inner product

$$\frac{\int p(x, y, z)\phi(x, y)dxdy}{\int \phi(x, y)^2 dxdy} = \max \tag{16}$$

The maximization of the function projection expressed by Eq. 17 is performed in the mean-square sense as follows:

$$\frac{\langle\langle(\int p(x, y, z)\phi(x, y)dxdy)(\int p(x', y', z')\phi(x', y')dx'dy')\rangle\rangle}{\int \phi^2(x, y)dxdy}$$
$$= \lambda > 0 \tag{17}$$

This equation leads to an eigenvalue problem [15],

$$\int R_p(x, y, x', y')\phi(x', y')dx'dy' = \lambda\phi(x, y) \tag{18}$$

where $R_p(x, y, x', y')$ is the space correlation of the pressure $p(x, y, t)$. The integration is performed numerically if a discrete pressure field is specified. When the pressure is given at uniformly spaced locations and a rectangular integration quadrature is employed, Eq. 18 is replaced with a matrix equation.

$$[S_{vv}(w)]\{\phi\} = \lambda\{\phi\} \tag{19}$$

where $[S_{vv}(w)]$ is the Davenport's wind speed spectrum correlation matrix, and $\{\phi\}$ and λ are a vector and a value to be determined. The eigenvalue indicates the degree of similarity between the eigenvector and spatial correlative random wind field.

3.   POD-PSEUDO-EXCITATION METHOD

Xu et al. [10] decomposed the excitation spectral matrix by LDLT method and analyzed the wind-induced response of high-rise structures. However, this method requires considerable computational cost to analyze long-span spatial structures because these kinds of structures often possess thousands of nodes. If the LDLT method is used to decompose this excitation spectral matrix as shown in Eq. 20

$$S_{vv}(w) = [L]^*[D][L]^T \tag{20}$$

then the scale of $[L]$ becomes huge. Every column of $[L]$ is considered as a sub power spectrum of the excitation spectral matrix, and N times for every w should be calculated. N is the number of nodes in the structure. The computation is highly expensive if the LDLT method is adopted. The number of nodes in long-span spatial structures can reach several thousands, implying that they require thousands times of operations for every w and cannot take advantage of the pseudo-excitation method.

This paper combines the proper decomposition technique with the pseudo-excitation method, which is called the POD-pseudo-excitation method, to analyze the wind-induced response.

First, the excitation spectral matrix obtained from Eq. 7 is decomposed with proper decomposition technique, as shown in Eq. 21.

$$S_{vv}(w) = [P]^*[D][P]^T \tag{21}$$

where $[P]$ is the eigen matrix consisting of eigenvector $S_{vv}(w)$, $[D]$ is a real diagonal matrix consisting of eigenvector, ' * ' is matrix conjugate transformation, and ' T ' is matrix transposition.

The nodal force spectrum is obtained using Eqs. 14 and 21.

$$\begin{aligned}
S_f(w) \\
= [B][P]^*[D][P]^T[B]^T \\
= [B][P]^*[\sqrt{D}]^T([B][P][\sqrt{D}])^T
\end{aligned} \tag{22}$$

We assume that $[F] = [B][P][\sqrt{D}]$. Then, every column of $[F]$ is considered as a group of random excitation. The kth pseudo-harmonic excitation can be expressed as

$$\{f_k(t)\} = \{F_k\} \exp(i\omega t) \tag{23}$$

This paper uses large eigenvalues, implying more contributions to structural responses and the corresponding eigenvector in the calculation of wind-induced response of YUJIAPU Railway Station building. The eigenvalue indicates the degree of similarity between the eigenvector and random wind field. Only part of the eigenvalue and the corresponding eigenvectors are used to represent the entire fluctuating wind field. The first 12-order eigenvectors of the wind speed spectrum when w is 0.1 Hz are shown in Figures 3 ($\lambda_1>\lambda_2>\lambda_3>\cdots>\lambda_{n-1}>\lambda_n$). The eigenvectors that correspond to large eigenvalues reflected the holistic distribution characteristics of the wind field, and the eigenvectors reflect the detail with the decrease in eigenvalue.
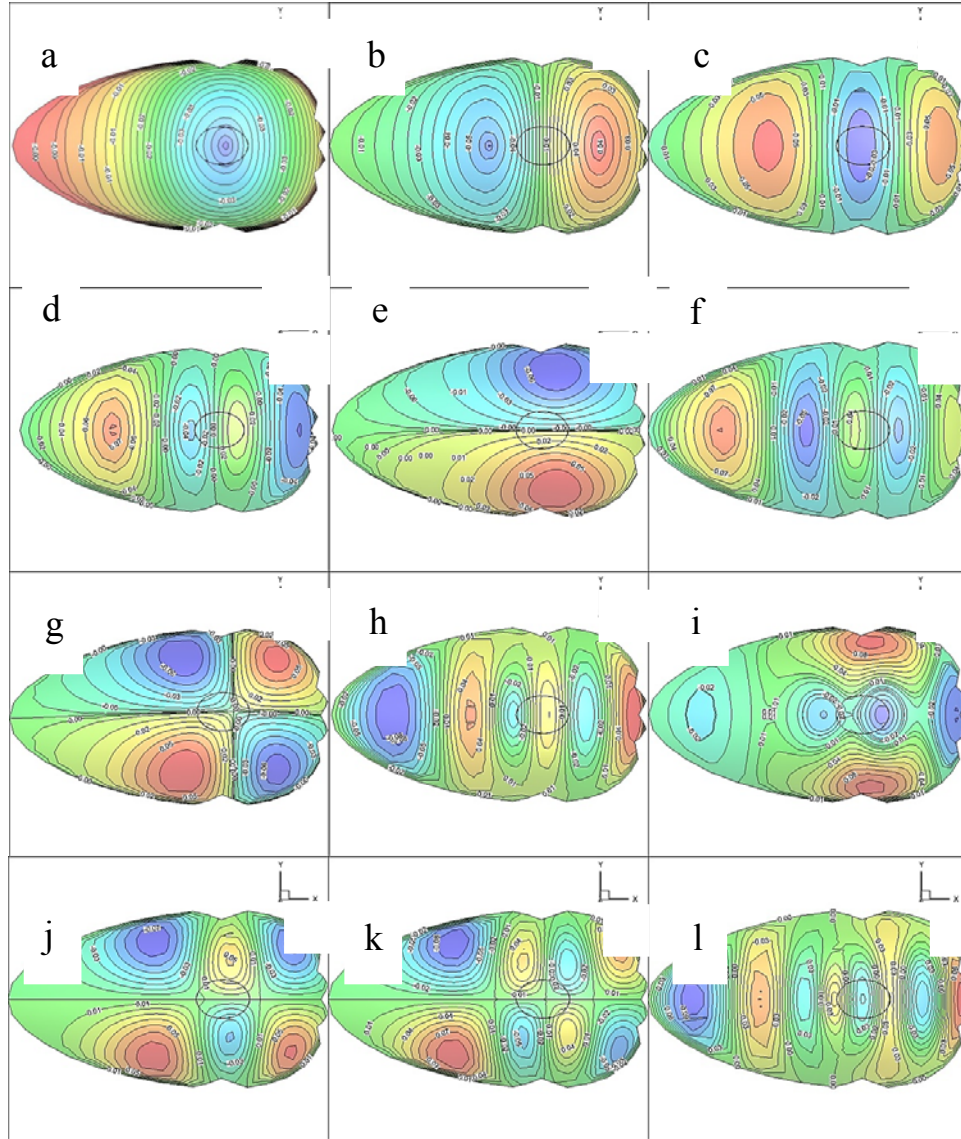
Figure 3. Contour of the First 12-Oorder Eigenvectors of Wind Speed Spectrum (w = 0.1Hz).
(a) eigenvector 1: eigenvalue = 20168, (b) eigenvector 2: eigenvalue = 7609, (c) eigenvector 3: eigenvalue = 3618, (d) eigenvector 4: eigenvalue = 2381, (e) eigenvector 5: eigenvalue = 2283, (f) eigenvector 6: eigenvalue = 1399, (g) eigenvector 7: eigenvalue = 1199, (h) eigenvector 8: eigenvalue = 1011, (i) eigenvector 9: eigenvalue = 784, (j) eigenvector 10: eigenvalue = 780, (k) eigenvector 11: eigenvalue = 666, (l) eigenvector 12: eigenvalue = 552
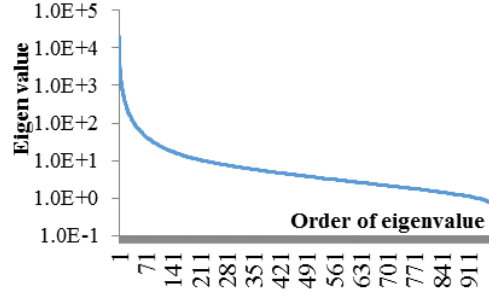
Figure 4. First 12-Order Eigenvalue of Wind Speed Spectrum (w=0.1Hz)

Figure 4 shows the changing trend in eigenvalue with the order. The eigenvalue decreased rapidly with the order, and thus the first r-order eigenvectors and eigenvalues accurately represent the stochastic wind field. Pseudo-harmonic excitation is substituted into the structural vibration differential equation as

$$[M]\{\ddot{u}_k\}+[C]\{\dot{u}_k\}+[K]\{u_k\}=\{f_k(t)\} \tag{24}$$

Rayleigh damping, $C = \alpha[M] +\beta[K]$, is adopted. α and β are constants determined by the following equation:

$\alpha = 2*\omega_1*\omega_2*\xi/(\omega_1+\omega_2)$

$\beta = 2*\xi/(\omega_1+\omega_2)$,

where ω_1 and ω_2 are circular frequency of the first- and second-order modes, and ξ is damping ratio of 0.02 for steel structures.

For each pseudo-excitation vector, a pseudo-displacement response vector, $\{u_k\}$, can be determined by

$$\{u_k\} = \sum_{j=1}^{n} H_j(iw)\{\phi_j\}^T\{f_k(t)\} \tag{25}$$

where n is the number of modes used in calculation. $\{u_k\}$ can be obtained through Eq. 25. Then, the response power spectrum is derived by

$$\{S_u(w)\} = \sum_{k=1}^{r}\{|u_k|\}^2 \tag{26}$$

where r is a parameter to be determined, which indicates the number of group of random excitations to be used in wind-induced response analysis.

The wind vibration coefficient is obtained by Eq. 27.

$$\beta = 1+\frac{\mu\sigma}{\overline{U}} \tag{27}$$

$$\sigma_u = \sqrt{\int_0^{+\infty} S_u(w)dw} \tag{28}$$

where β is the wind vibration coefficients of displacement at a certain node, μ is peak guarantee factor of 3.5, $\bar{u}$ is algebraic average of displacement obtained using time domain analysis, and σ_u is the mean square root value of displacement response.

With the complexity of the conch-shaped single-layer lattice shell, determining the surface normal direction is an intricate process. This paper obtained the response power spectrum by combining the harmonic response analysis module and secondary development of finite element software package ANSYS. The wind vibration coefficient was obtained using MATLAB.

4.   RESULTS AND COMPARISON

4.1   Structural Natural Vibration Characteristics

The software package ANSYS is used to obtain the natural vibration characteristics through modal analysis. The first six-order modes and natural vibration frequency are shown in Figures 7–8.
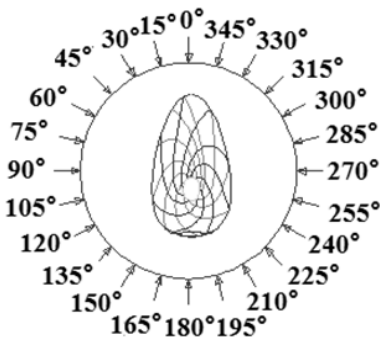
Figure 5. Sketch Map of Wind Direction   Figure 6. Structure Finite Element Model
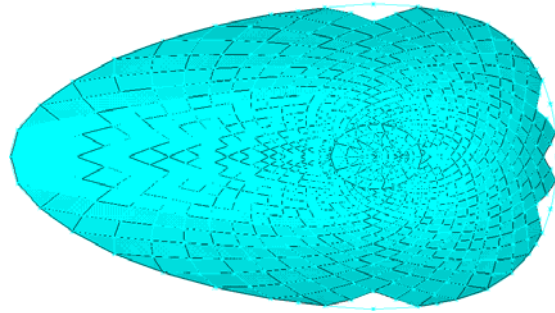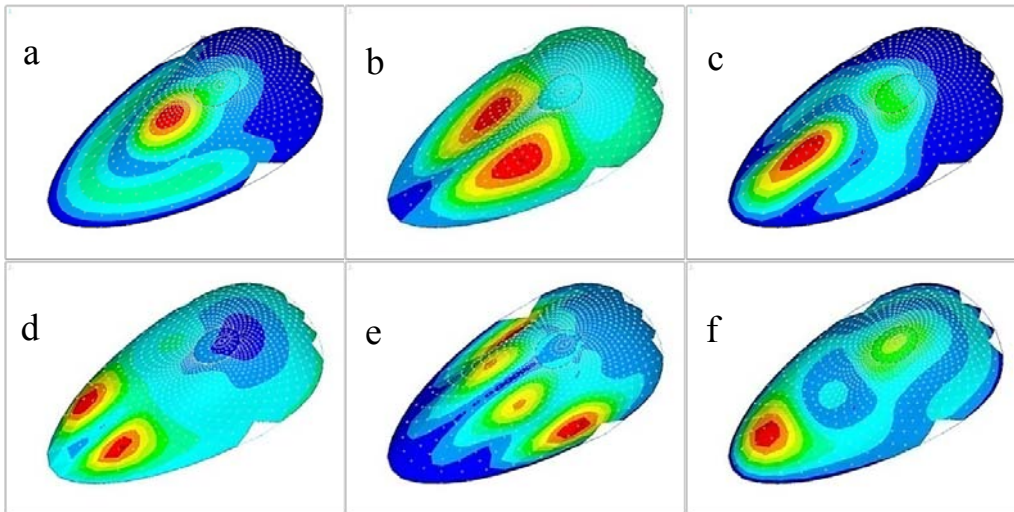
Figures 7. Mode Shapes of the First Six Modes. (a) Mode 1:f1 = 1.562 Hz,
(b) Mode 2:f2 = 1.644 Hz, (c) Mode 3:f3 = 2.113 Hz, (d) Mode 4:f4 = 2.166 Hz,
(e) Mode 5:f5 = 2.303 Hz, (f) Mode 6:f6 = 2.537 Hz.
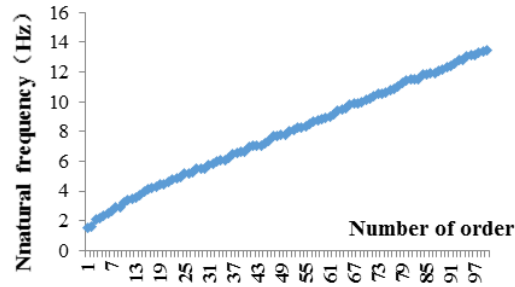
Figure 8. Distribution of the First 100 Natural Frequencies

4.2   Wind Tunnel Test

This study conducts a wind-induced response analysis for YUJIAPU Railway Station building in wind direction of 0°. The wind pressure coefficient obtained through a wind tunnel test is shown in Figure 10. The equivalent nodal wind load was obtained by substituting pressure coefficient into Eq. 12.

Figures 9. Wind Tunnel Test Model (a) Overview, (b) Close-up view
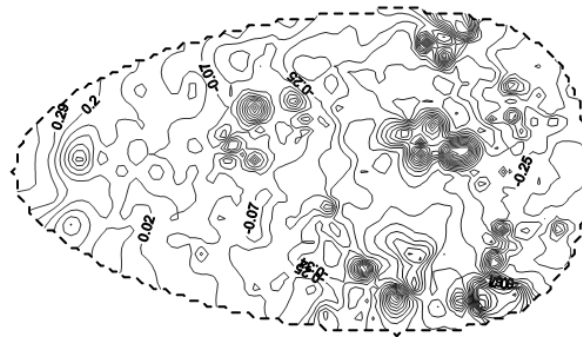
Figure 10. Contour of Pressure Coefficient

4.3   Change of Wind-induced Response with Number of Eigenvectors

For comparison, linear filtering method and the same *Kaimal* spectrum, which were used in POD-pseudo-excitation method generated the wind load time history, which is used in wind-induced response analysis in the time domain. The wind vibration coefficient was obtained with dynamic time history analysis by using ANSYS. Refer to other documents[16-17] for the detailed process of linear filtering method. Figure 11 shows the wind speed time series and power spectrum obtained from the linear filtering method.

(a)   (b)
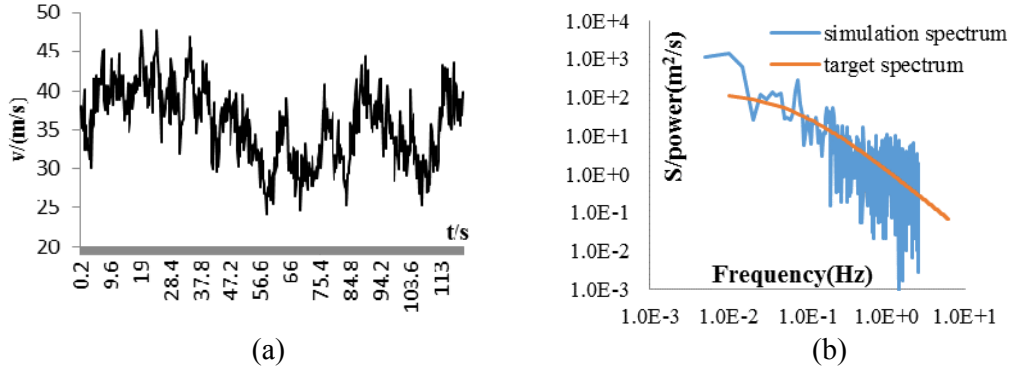
Figure 11. Simulated Wind Speed of Element 2901 (a) Time History of Wind Speed
(b) Comparison of Simulation Spectrum and Target Spectrum

To obtain the minimum r under the condition that satisfies the calculation accuracy, the relationship between wind-induced displacement response and the number of r (i.e., the number of pseudo-excitation groups used in the analysis) were examined, as shown in Figure 13. The mean square deviation of displacement did not change when r reached a certain degree. Thus, the response induced by the random excitation represented by a higher order of eigenvectors can be ignored, and the accuracy of results is not affected.
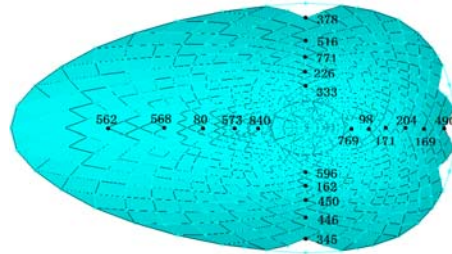
Figure 12. Number of Nodes Located at Typical Position
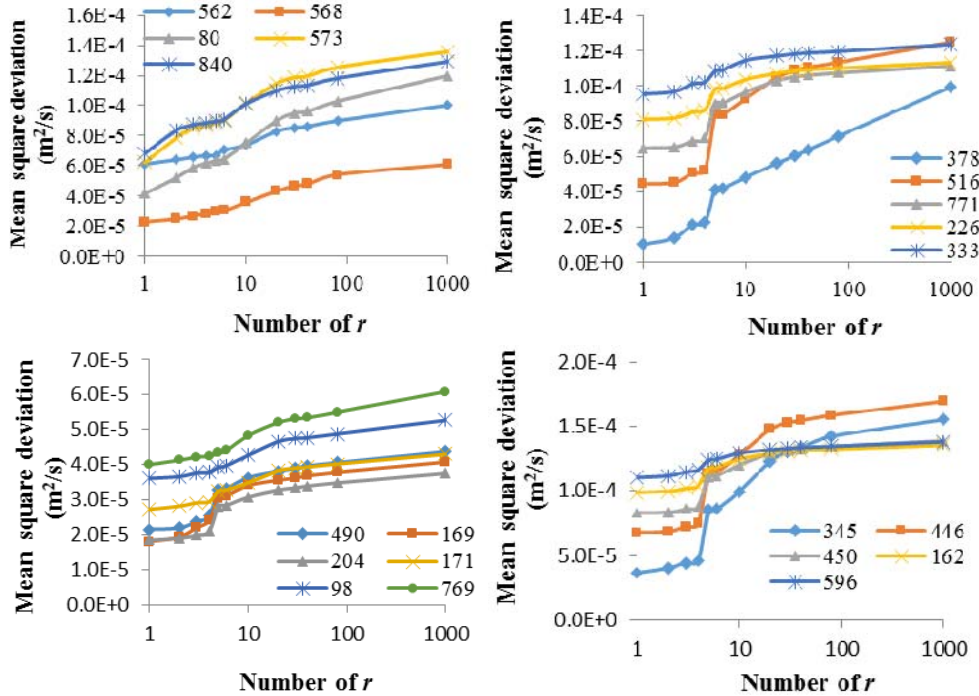
Figure 13. Relationship between Response and Number of r

For the purpose of quantitative research, we assume that $\lambda_{sum} = \sum_{i=1}^{n} \lambda_n$, n is the number of structural nodes for general situation, $\rho_i = \lambda_i / \lambda_{sum}$ which indicates the weight of the ith group of random excitation represented by the ith order eigenvector. Figure 14 shows that the weight of the first 20 groups of random excitation can reach 80%, and the weight of the first 80 groups is 90%. The accuracy of the result was validated and could satisfy the requirement when r is 80. This paper recommends λ_{sum} to be 90% for these kinds of structures, implying that the computational cost can be reduced by 92% without sacrificing accuracy.
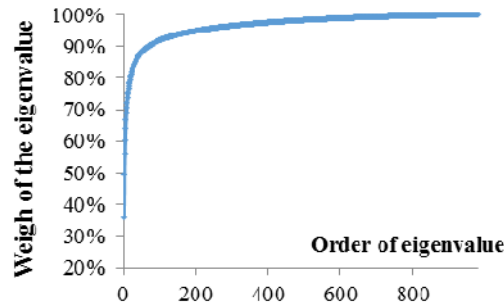
Figure 14. Accumulative Weight Graph of Eigenvalue

4.4   Change in Wind-induced Response with Frequency Range

Figure 2 shows that wind load rarely contains high-frequency components. This study explored the effect of high-frequency components of wind load on the response of long-span spatial structures. Figure 15 illustrates the relationship between the mean square deviation of displacement response and frequency of load. The displacement response has mutations at natural frequency of structure, and this phenomenon is most obvious at the first-order natural frequency. The displacement response is extremely small after the first-order natural frequency.
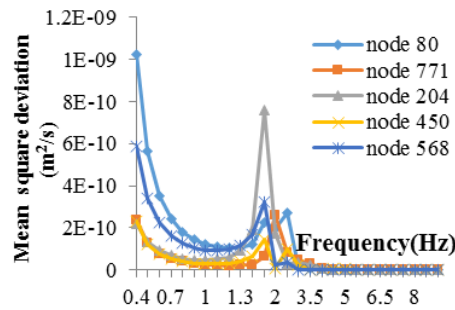
Figure 15. Reflected Power Spectrum Curve of Nodes

Figure 16 shows that the mean square deviation of displacement did not change after the first-order natural frequency. Thus, the high-frequency part of wind load slightly affected the response of long-span spatial structures. The highest frequency of the wind load can be obtained as the first-order natural frequency of long-span spatial structures, which can substantially reduce the computational cost.
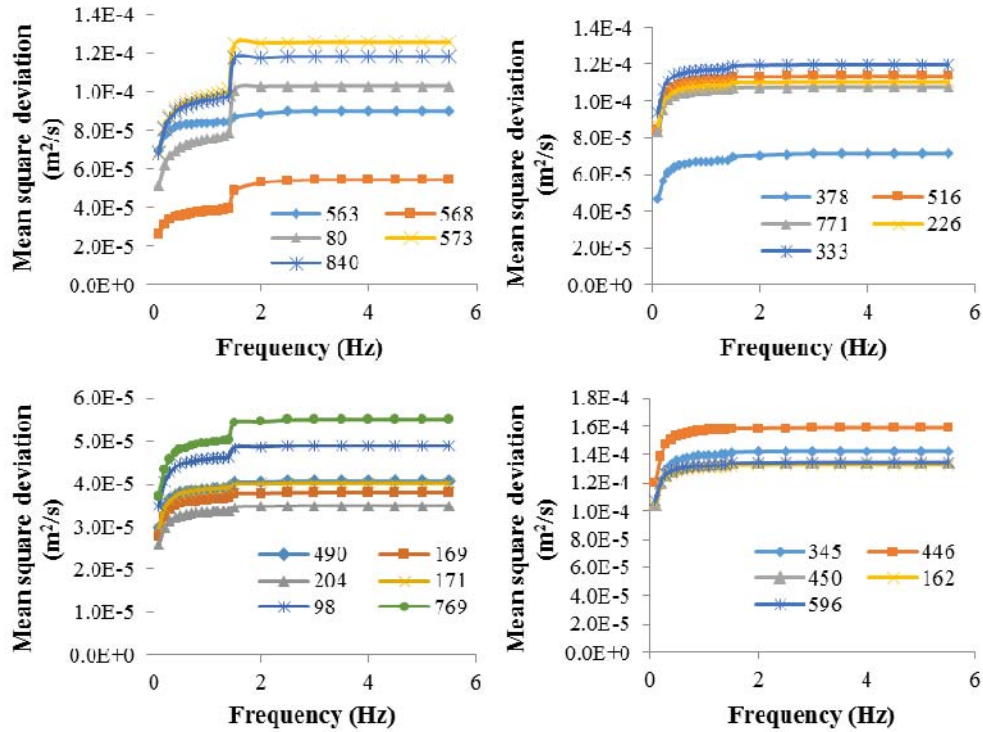
Figures 16. Relationship between Response and Frequency

4.5   Comparison of Results Derived Using Different Methods

To reflect the accuracy and efficiency of the POD-pseudo-excitation method, this paper provides the contour of the wind vibration coefficient calculated by different methods as shown in Figure 17. The results obtained by the LDLT-pseudo-excitation and POD-pseudo-excitation methods were consistent. Therefore, they are equivalent in the mathematical sense. From (b) and (c), we conclude that the first 80 order groups of pseudo-excitation can be used to represent the entire random wind field, guaranteeing the accuracy and substantial reduction of computational cost. Comparison of (a), (b), and (d) shows that the results obtained using the time-domain and frequency-domain methods were consistent, and the computational cost was reduced by 92%, establishing the foundations for research on high-efficiency computational technique in the frequency domain for wind-induced analysis of long-span spatial structures.

5.   CONCLUSIONS

This paper conducted a wind-induced response analysis by using POD-pseudo-excitation method combined with secondary development of ANSYS general purpose software package. Wind vibration coefficient was obtained. Based on an analysis of the results, the following conclusions are presented:

• A new method that can be efficiently used in wind-induced response analysis for long-span spatial structures was proposed. Through the combination of proper decomposition technique and pseudo-excitation method, the computational cost was considerably reduced and the accuracy was validated. This method can be conveniently used by secondary development of mature software package.

• The first-order natural frequency can be used as the upper limit of wind load frequency for the object to reduce computational cost, and the accuracy can be guaranteed for spatial structures.

• Comparison of the results obtained by the time-domain and frequency-domain methods shows that the results indicated were consistent with each other, and the computational cost can be reduced by 92% without sacrificing the accuracy.
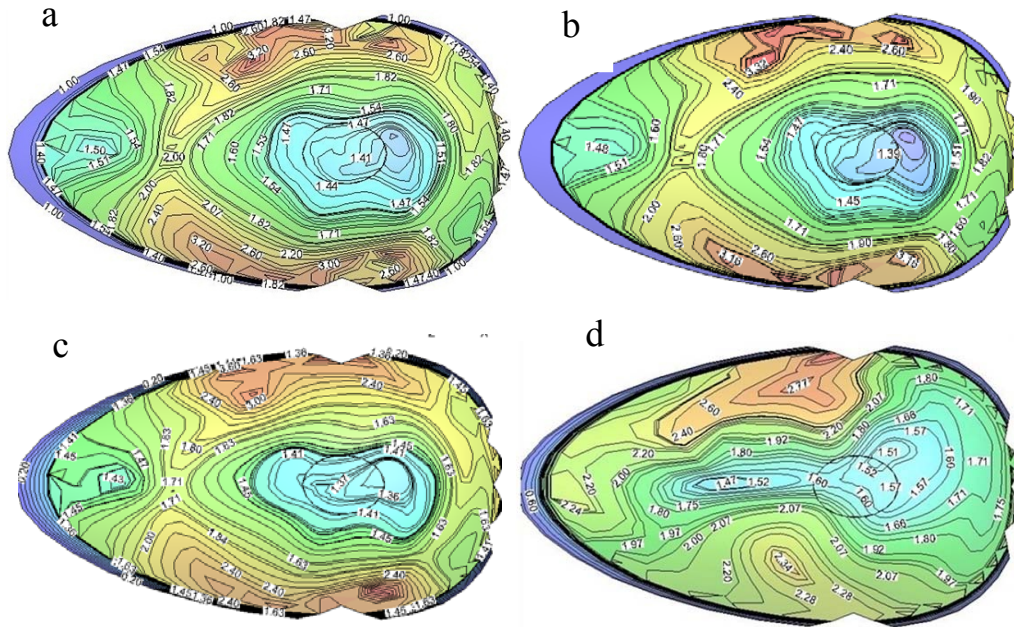
Figures 17. Comparison of Wind Vibration Coefficient. (a) LDLT-pseudo-excitation method, (b) POD-pseudo-excitation method ($r = 980$), (c) POD-pseudo-excitation method ($r = 80$), and (d) dynamic time history analysis.

ACKNOWLEDGEMENT

REFERENCES

[1]   Bian, J.F. and Wei, D.M., "Wind Velocity Time-history Numerical Simulation Theories in Long-span Spatial Structures", Journal of Jinan University, 2005, Vol. 26, No. 1, pp. 87-90.
[2]   Zhang, J.S., Wu, Y. and Shen, S.Z., "Study on Wind-induced Vibration of Single-layer Cylindrical Reticulated Shell Structures", Industrial Construction, 2006, Vol. 36, No. 10, pp. 69-72.
[3]   Samali, B., Yang, J.N. and Yeh, C.T., "Control of Lateral-torsional Motion of Wind-excited Buildings", Journal of Engineering Mechanics, 1985, Vol. 111, No. 6, pp. 777-796.
[4]   Xu, Y.L., Samali, B. and Kwok, K.C.S., "Control of Along-wind Response of Structures by Mass and Liquid Dampers", Journal of Engineering Mechanics, 1992, Vol. 11, No. 81, pp. 20-39.
[5]   Zhou, Z., Li, Z.M., Meng, S.P. and Jing, W., "Wind-Induced Vibration Responses of Prestressed Double-layered Spherical Latticed Shells", International Journal of Steel Structures, 2011, Vol. 11, No. 2, pp. 191-202.

[6]   Chen, S.R., Cai C.S., Chang, C.C. and Gu, M., "Modal Coupling Assessment and Approximated Prediction of Coupled Multimode Wind Vibration of Long-span Bridges", Journal of Wind Engineering and Industrial Aerodynamics, 2004, Vol. 92, No.5, pp. 393-412.

[7]   Lin, J.H., "A Fast CQC Algorithm of PSD Matrices for Random Seismic Responses", Computers and Structures, 1992, Vol. 44, No.3, pp. 683-687.

[8]   Lin, J.H., Sun, D.K., "Application of Pseudo-excitation Method to 3D Buffeting Analysis of the Ting Ma Long-span Suspension Bridge", Journal of Dalian University of Technology, 1999, Vol. 39, No. 2, pp. 172-179.

[9]   Lin, J.H., Zhang, W.S. and Li, J.J., "Structural Response to Arbitrarily Coherent Stationary Random Excitations", Computers & Structures, 1994, Vol. 50, No. 5, pp. 629-634.

[10]   Xu, Y.L, Zhang, W.S., Ko, J.M and Lin, J.H., "Pseudo-excitation Method for Vibration Analysis of Wind-excited Structures", Journal of Wind Engineering and Industrial Aerodynamics, 1999, Vol. 83, No. 1, pp. 443-454.

[11]   Chen, B., Yang, Q.S. and Wu, Y., "Wind-Induced Response and Equivalent Static Wind Loads of Long Span Roofs", Advances in Structural Engineering, 2012, Vol. 15, No. 7, pp. 1099-1114.

[12]   Yang, Q.S. and Tian, Y.J., "Wind-induced Responses of Beijing National Stadium",Wind and Structures,2011, Vol.14, No.3, pp.239-252.

[13]   Zhou, X.Y. and Gu, M., "an approximation method for computing the dynamic responses and equivalent static wind loads of large-span roof structures", International Journal of Structural Stability and Dynamics, 2010, Vol.10, No.5, pp. 1141-1165.

[14]   Bienkiewicz, B., Tamura, Y., Ham, H.J., Ueda, H. and Hibi, K., "Proper Orthogonal Decomposition and Reconstruction of Multi-channel Roof Pressure", Journal of Wind Engineering and Industrial Aerodynamics, 1995, Vol.54, No. 55, pp. 369-381.

[15]   Chen, B., Wu, Y. and Shen, S.Z., "The Principle and Application of Ritz-POD Method", Chinese Journal of Computational Mechanics, 2007, Vol. 24, No. 4, pp. 499-504.

[16]   Zhang, W.F., Ma, C.H. and Xiao Y., "Some Issues on AR Models for Wind Field Simulation", Chinese Journal of Computational Mechanics, 2009, Vol. 26, No. 1, pp. 124-130.

[17]   Yuan, B., Ying, H.Q. and Xu, J.W., "Simulation of Turbulent Wind Velocity Based on Linear Filter Method and MATLAB Program Realization", Structural Engineers, 2007, Vol. 23, No. 4, pp. 55-61.

FORCE FINDING OF SUSPENDED-DOMES
USING BACK PROPAGATION (BP) ALGORITHM

Jiamin Guo [1,*], Xingfei Yuan [2], Zhixin Xiong [1] and Shilin Dong [2]

[1] *School of Ocean Science and Engineering, Shanghai Maritime University, Shanghai 200135, China*
[2] *Department of Civil Engineering, Zhejiang University, Hangzhou 310058, China*
*(Corresponding author: E-mail: guojiamin@zju.edu.cn)

ABSTRACT: Force finding is a key step when designing a suspended-dome. To give a general simple method for force finding, this report accomplished research on the application of a BP network to force finding of a suspended-dome under a certain tension process. First, this paper gives three typical states of the construction process, and then, it selects the internal force in the hoop cables at the initial state as the input data and the initial strain of the active element at the zero state as the output data. Then, a three-layer BP network was developed for force finding of the suspended-dome model. Second, this paper presents a method for restricting the training set range, in which 1000 sets of patterns were generated by the finite element software ANSYS. Then, we randomly selected 19 groups of training data from 1000 sets of samples to train the BP network and predicted the results of force finding. Last, this paper combines GA with BP to predict the results of force finding. The results show that the BP network can solve the force-finding problem accurately and effectively when the training samples are sufficient. The prediction stability of the BP network and the prediction precision can be significantly enhanced after the initial weights and the thresholds are optimized by a GA.

1.   INTRODUCTION

Tensegrity structures, which consist of continuous tension elements and discontinuous compression elements, were proposed by Fuller, and the first tensegrity structure was designed by Snelson in 1948. To date, the tensegrity concept has become a basic principle of nature and has been applied to so many fields of science that perhaps it is losing its main meaning (Gómez [1]). With respect to the basis of the tensegrity concept, Geiger invented the cable dome, which includes a compressed ring in the boundary of a tensegrity structure (Pellegrino [2]). Since then, the first cable dome was designed by Geiger: for the Olympics in Seoul (1986), followed by the Redbrid Arena in Illinois (1988), the Florida Suncoast Dome in St. Petersburg (1988), and the Taoyuan Arena in Taiwan (1993). At the same time, its large hoop beam and its difficult construction has constrained its widespread application. In 1993, Kawaguchi et al[3] introduced the single-layer latticed shell into the cable dome and invented the suspended-dome, which take advantage of both structural systems (Chen et al. [4]). As an improved cable dome, suspended-dome replaces the upper cables of the cable dome with a single-layer latticed shell that can provide a certain initial stiffness, and as a result, its construction is simplified. Suspended-dome is also an improved single-layer latticed shell with a lower cable-strut, which can strengthen the upper shell.

Suspended-dome consists of the compression-only vertical struts, the tension-only hoop cables and radial cables. Since it was proposed, suspended-dome has been attracting much attention from both researchers and engineers. These investigators have performed some theoretical and experimental research on the structural mechanical properties, including construction simulation and morphological analysis.

Kang and Chen [5] noted that the lower cable-strut could reduce the internal force of a single-layer latticed shell. Additionally, model tests on a small-scale suspended-dome indicated that the stability and the rigidity have been improved greatly compared with the single-layer latticed shell (Kawaguchi et al. [6]). In addition, The internal force flow in suspended-dome could be built in a closed loop, thus making the structure a self-equilibrated system, and a weak boundary bearing system becomes possible (Zhang et al. [7]). Dong et al.[8] studied tension schemes by an experimental model and noted that the construction difficulty is lower than the cable domes and that tensioning radial cables is better than tensioning hoop cables. These favorable properties make suspended-dome an ideal choice for many applications. In Japan, the Hikarigaoka Dome and the Fureai Dome have been constructed. In China, suspended-dome was employed in structures for the Olympics in Beijing (2008), the Olympic Sports Centre's Gymnasium in Changzhou, and the Olympic Centre in Jinan (2009).

In practical design and analysis, the determination of the initial configuration and the initial prestress is of great importance for suspended-dome structures; this analysis approach is known as morphological analysis. Much research on the morphology of tensegrity structures has been performed[9, 10]. However, few studies have been performed for suspended-dome structures. A simplified strategy for force finding analysis of suspended-domes based on the local analysis method was present (Cao and Zhang [11]), but the present strategy did not consider the influence of the actual construction process. Zhuo et al. [12] studied the control algorithm of tension force on the basis of the measured internal forces in the actual construction and gave the tension force correction calculation method. However, the developed methods appear to be inconvenient for engineers to operate. Based on the known parameters, the morphological analysis of the suspended-dome was classified into three categories: form finding, force finding and form and force finding, but they cannot be described by an algorithm that is based on mathematical concepts (Guo et al [13]).

The back propagation algorithm (BP) has a vigorous ability to solve problems that cannot be described in terms of a mathematical concept. After McCulloch and Pitts (1943) introduced models of neurological networks, Rumelhart and McClelland developed the back-propagation of error learning procedure (abbreviated: BP), and realized the concept that non-linearly separable problems could be solved by multilayer perception. From that time on, the multi-layered network trained by the back-propagation algorithm has been applied extensively to solve various engineering problems [14, 15]. In the following, this paper will focus on the force finding of a suspended-dome under conditions of different tension processes by using a BP neural network.

2.   FORCE FINDING

During the overall construction, suspended-dome will experience three typical states: the zero state, initial state and loading state [16]. The structure will include different loads under different states. This paper selects the initial strain to simulate pre-stress on a numerical model. For practical projects and numerical models, the state parameters and the loads that were considered under different states are described in detail in Tables 1-2.

Table 1. Three Typical States and State Parameters for Practical Projects

Typical states	Loads considered			State parameters	
	pre-stress	self-weight	outer loads	geometry	force
Zero state(Z)	×	×	×	G_Z	F_Z
Initial state(I)	√	√	×	G_I	F_I
Loading state(L)	√	√	√	G_L	F_L

Note: × = excluding the corresponding generalized loads; √ = including the corresponding generalized loads.

Table 2. Three typical states and state parameters for a numerical model

Typical states	Loads considered			Solving state	State parameters	
	Initial strain	self-weight	outer loads		geometry	force
Zero state(Z)	√	×	×	Before solving	G_Z	F_Z
Initial state(I)	√	√	×	Solution is done	G_I	F_I
Loading state(L)	√	√	√	Solution is done	G_L	F_L

There are six state parameters (G_Z, F_Z; G_I, F_I; G_L, F_L) at three different states in Tables 1-2. To build a numerical model, G_Z and F_Z at the zero state are the two essential parameters. Thus, the determination of G_Z and F_Z is a key step for the following design and analysis. The determination of G_Z or F_Z is so-called form finding and force finding, respectively. Because of the rigid upper latticed shell, the discrepancy of geometric configurations between the zero state and the initial state is rather slight, and therefore, form finding analysis is usually a dispensable for the sake of simplification of the design (Cao and Zhang [11]). In this paper, the geometric configuration at the zero state (G_Z) is taken as a known parameter that is equal to the geometric configuration from the architectural drawings. When the geometric configurations at the zero state (G_Z) and the internal force at the initial state or loading state (F_I or F_L) are known, this paper will mainly study the force finding, which is the problem of determining the initial strain F_Z at the zero state.

The pre-stress in the suspended-dome will appear only if the structure is tensioned according to a certain tension process; thus, the tension process should be considered during the force finding. During practical construction, we directly apply the force to the tension elements, which are so-called active tension elements, according to the given construction process. Other elements are so-called passive tension elements, which include the components of a single-layer latticed shell. For the numerical model, we apply the internal force to the active elements according to the given construction process at the zero state. In other words, the construction process will determine the components on which the internal force will be applied at the zero state. Thus, the upper force-finding problem can be described as follows.

$$\begin{cases} F_I(orF_L) = \Psi(F_Z) \\ s.t. \text{ special } construction\ process \end{cases} \tag{1}$$

Because the upper function Ψ cannot be described in terms of a mathematical concept, force finding of a suspended-dome is in a problem category that cannot be formulated as an algorithm. Thus, F_Z cannot be calculated by Ψ^{-1}. In reference (Guo et al [13]), F_Z was solved by Newton iteration. However, the associated developed methods are inconvenient for engineers to operate.

From Eq. 1, we can see that we input any F_Z that conforms to a special construction process; then, the corresponding F_I (or F_L) can be output. This paper will use the BP network to address the upper fuzzy function between F_Z and F_I (or F_L).

3.   BP NEURAL NETWORKS

Artificial neural networks (ANN) consist of very simple but numerous nerve cells that work massively in parallel and that have the capability to learn. The main characteristics of ANNs are self-organization learning capability, generalization capability and fault tolerance. An ANN has an excellent ability to learn and to describe the highly nonlinear and strongly coupled relationships between multiple-input and multiple-output variables (Kriesel [17]). The basic structure of the neuron is shown in Figure 1.
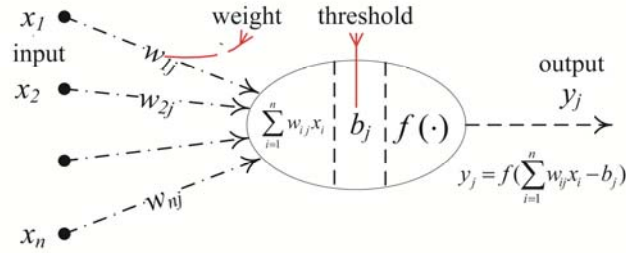
Figure 1. The Basic Structure of the Neuron

where x_n is the nth input signal, w_{nj} is the connection weight from the nth input neuron to the jth neuron, b_j is the threshold value of the jth neuron, and y_j is the output signal of the jth neuron. The neuron output signal y_j is calculated by the activation function, as follows:

$$y_j = f(\sum_{i=1}^{n}(w_{ij}x_i) - b_j) \tag{2}$$

Many types of activation functions have been proposed, among which the most popular activation function for back-propagation networks (BP) is the sigmoid, which is expressed as follows:

$$f(x) = \frac{1}{1 + e^{-cx}} \tag{3}$$

In this study, the value of the parameter c is 1.

The BP neural network is a multilayer feed forward network, whose basic network structure for the upper force finding can be built as shown in Figure 2.
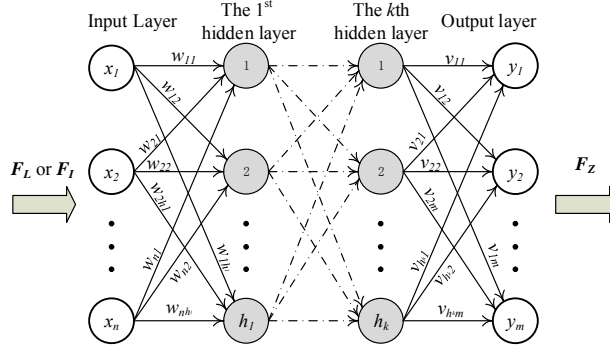
Figure 2. The Structure of the BP Network

The network with *n* input and *m* output neurons is clearly delineated: there is one input layer, one output layer and one or more hidden layers. Each layer consists of several neurons, and the layers are interconnected by sets of correlation weights. In the BP neural network, the error at the output layer propagates backwards to the input layer through one or more hidden layers to obtain the desired outputs.

The processes of the BP network for solving the force finding include the following three steps:

Step 1: Establishing the network

The number of the input and output neurons (*n, m*) and the hidden layer (*k*) is first determined according to a practical tension process.

Then, the number of units in *i*th hidden layer (h_i) is determined according to the number of the input and output neurons. Gao [18] studied many practical examples on calculating the number of units in the hidden layer and gave a fitting empirical formula by the least square method, as follows. The empirical formula will be used in this paper.

$$h_i = \sqrt{0.43mn + 0.12m^2 + 2.54n + 0.77m + 0.35} + 0.51 \tag{4}$$

Last, the connection weights (w_{ij}) and the thresholds (b_j) are initialized to values between -1 and +1, randomly.

Step 2: Training the network

Training the network is the process of repeatedly modifying the connection weights (w_{ij}) and the thresholds (b_j) according to the difference between the output patterns and the desired output patterns until the optimal weights and thresholds appear. The detailed process of training the network is the following: First, we can obtain a training set that consists of input patterns $[X]_{a \times n}$ and the corresponding output patterns $[Y]_{a \times m}$ by experiments or numerical analysis. Then, we apply the inputs to the network and compute the prediction outputs $[P]_{a \times m}$. We compare $[P]_{a \times m}$ with $[Y]_{a \times m}$ and provide the error vector. Last, we change the weights (w_{ij}) and the thresholds (b_j) based on the error vector. Generally, the training will stop when the error is small enough.

Step 3: Generalization (or Prediction)

The most interesting characteristic of neural networks is their capability to familiarize with problems by means of training and, after sufficient training, to be able to solve unknown problems of the same class. Thus, we can utilize the trained network to generalize the results of force finding, corresponding to the known values $\tilde{N}$. If the prediction errors do not meet the allowable value ε, then we should expend the scale of the training patterns and then repeat the above steps, namely, step 2 and step 3.

The initial weights and thresholds will influence the training difficulty and generalization error because they are random numbers mentioned in step 1. Thus, this paper will use a Genetic Algorithm (GA) to optimize the initial weights and thresholds of the BP network.

The optimization starts from the first population that consists of many randomly generated individuals, which include the weights and the thresholds of the BP network arranged in linear succession. Then, the BP network with different individuals is trained by input data $[X]_{a \times n}$ and output data $[Y]_{a \times m}$, and the absolute error between the output $[Y]_{a \times m}$ and the prediction output

$[P]_{a \times m}$ for different individuals is calculated and set as the individual fitness. The fitness of the optimal individual is minimal among all of the individuals. Subsequently, a Roulette Wheel Selection generates a new population. Some of the individuals undergo transformations by means of crossover and mutation. This process occurs when moving from the current population to the next population and constitutes one generation in the genetic algorithm evolutionary process. After some generations, the program converges to a feasible solution in which the best individual represents a near-to-optimum solution.

The BP network and the GA were programmed and executed by using the neural network toolbox and GA toolbox of the MATLAB (version 7.14, 2012a) software. All of the input and output data were generated by ANSYS software. The whole process described above is summarized in the flowchart of Figure 3.
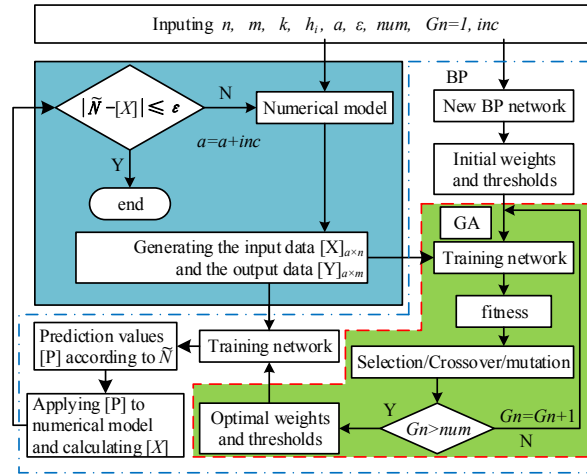
Figure 3. Flowchart of Force Finding for the Suspended-dome with BP

4.   AN ILLUSTRATIVE EXAMPLE

The numerical model shown in Figure 4 is selected as an illustrative example, which considers a span and rise of 122 m and 12.2 m, respectively. Its lower cable-strut arrangement is a rib pattern that includes three rings of cables and struts. In addition, the concrete lattice pattern of the upper single-layer latticed shell is a hybrid pattern that combines the Keiwitt pattern with a sunflower pattern. Table 3 presents the cross-sectional area and the material properties of radial cables, hoop cables, struts and all components in the single-layer latticed shell. This paper assumes that the internal forces of the hoop cables at an initial state from the outermost to the innermost ring are 2500kN (H1), 1000kN (H2), and 500kN (H3), respectively. In other words, the F_I of the suspended-dome is a known value that can be expressed as $\tilde{N} = [2500\text{kN}, 1000\text{kN}, 500\text{kN}]$, and the geometry configuration at the zero state (G_Z) is described in Figure 4. The numerical model will be analyzed by the ANSYS program. The element types for the components in the numerical model are also listed in Table 3. In the following research, the suspended-dome will be constructed by three different tension processes: tensioning hoop cables, tensioning radial cables and jacking struts.

Table 3. Geometrical and Material Properties for the Components of the Numerical Model

Members	Sectional area /m^2	density / kg / m^3	Young's modulus E/ pa	Element type
H1	0.01124	6.55×10^3	1.9×10^{11}	Link10
H2	0.00562	6.55×10^3	1.9×10^{11}	Link10
H3	0.00285	6.55×10^3	1.9×10^{11}	Link10
R1	0.00562	6.55×10^3	1.9×10^{11}	Link10
R2	0.00285	6.55×10^3	1.9×10^{11}	Link10
R3	0.00285	6.55×10^3	1.9×10^{11}	Link10
S1	0.004662	7.85×10^3	2.06×10^{11}	Link8
S2	0.004662	7.85×10^3	2.06×10^{11}	Link8
S3	0.004662	7.85×10^3	2.06×10^{11}	Link8
Single layer latticed shell	Ø377×12	7.85×10^3	2.06×10^{11}	Beam188
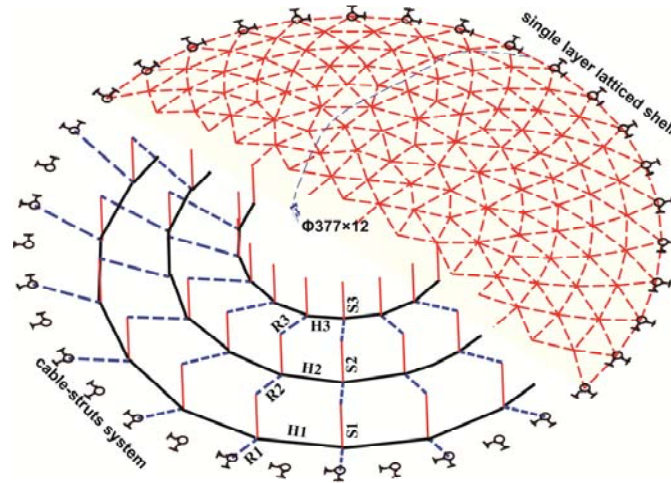
(a) Numerical model (perspective view), (S=Struts, H=Hoop cables and R=Radial cables)
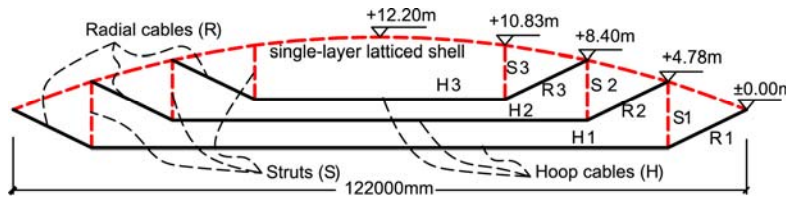
(b) Numerical model (vertical view)

Figure 4. Numerical Model of Suspended-dome

During the force finding, the internal force at the zero state will be simulated by the initial strains, which are applied only to the corresponding active tension elements; these elements are hoop cables, radial cables and struts for tensioning the hoop cables, radial cables and jacking struts.

According to the known parameters and the construction process, the initial strain at the zero state and the internal force at the initial state are selected as the input data and the output data for the BP network, respectively. The detailed sources of the input data and the output data under different tension processes are listed in Table 4.

Table 4. Input and Output Data under Different Construction Processes

Construction process	Input data F_I(internal forces)			Output data F_Z (initial strains)		
Tensioning hoop cables	H1	H2	H3	H1	H2	H3
Tensioning radial cables	H1	H2	H3	R1	R2	R3
Jacking struts	H1	H2	H3	S1	S2	S3

From Table 4, we can symbolize the input data and the corresponding output data as follows:

$$[X]_{a \times 3} = \begin{bmatrix} F_I^1, & F_I^2, & F_I^3 \end{bmatrix}_a \tag{5}$$

$$[Y]_{a \times 3} = \begin{bmatrix} F_z^1, & F_z^2, & F_z^3 \end{bmatrix}_a \tag{6}$$

where a is the data size.
A simple three-layered neural network with an input layer, a hidden layer and an output layer is adopted in this paper. According to Eq. 4, the number of units in the hidden layer is set to 5. Thus, the structure of the BP network for force finding is 3×5×3.

Generally, the training data (the input and the output) for the BP network can be randomly generated according to the given tension process. At the same time, to allow the training data, especially the input data, approach the known values of $\tilde{N}$, this paper restricts the range of the training data by the following process:

Step 1: this paper gives the initial range of the output data $[Y]_{a \times 3} = \begin{bmatrix} F_z^1, & F_z^2, & F_z^3 \end{bmatrix}_a$ for the corresponding active elements, as follows:

$$\beta \frac{1 \times 10^4}{EA_i} \le F_z^i \le \gamma \frac{1 \times 10^4}{EA_i} \quad (i = 1, 2, 3)$$
$$\left| EA_1 F_z^1 \right| > \left| EA_2 F_z^2 \right| > \left| EA_2 F_z^3 \right| \tag{7}$$

where E and A_1, A_2, A_3 are the young's modules and sectional area of the corresponding active elements, and β and γ are the random values. Here, this paper allows $\beta=1$, $\gamma=20$ for tensioning the hoop cables and the radial cables and $\beta=-20$, $\gamma=-1$ for the jacking struts.

Step 2: this paper generates training data in the upper range and obtains the prediction values $^pF_z^i$ that correspond to the known values $\tilde{N}$.

Step 3: the new range for the training data is given as follows:

$$\eta_1 \, ^pF_z^i \le F_z^i \le \eta_2 \, ^pF_z^i \quad (i = 1, 2, 3)$$
$$\left| EA_1 F_z^1 \right| > \left| EA_2 F_z^2 \right| > \left| EA_3 F_z^3 \right| \tag{8}$$

where η_1 and η_2 are random values. Here, this paper allows $\eta_1=0.9$ and $\eta_2=1.1$ for tensioning the hoop cables and the radial cables and $\eta_1=1.1$, $\eta_2=0.9$ for the jacking struts.

According to the upper process, this paper first generated 100 patterns randomly according to step 1, some of which were listed in Table 5.

Then, this paper applied the training data to the network without optimizing by the GA and predicted the output data that corresponds to the known input data $\tilde{N}$ five times, according to the scheme in Figure 3. During the prediction, the BP network will be trained by the Levenberg-Marquardt method, which is a perfect approach for small-size networks. Additionally, the technical parameters of the BP network are set as: net.trainParam.lr=0.01 and net.trainParam.goal=0.0000001. The active function in the hidden layer will adopt the tan-sigmoid transform function (tansig()), and the output layer is the linear function (purelin()). The prediction results that correspond to the three different construction processes at the zero state are summarized in Table 6.

Table 5. Partial Training Samples for Three Different Construction Processes

construction process	NO	input data /kN			output data/($\times 10^4$/EA$_j$)		
		H1	H2	H3	H1	H2	H3
Hoop	1	13710.230	5978.154	3340.706	1709.632	968.652	837.188
	2	12515.590	6849.735	4264.299	1415.498	1274.050	1121.364
	…	…	…	…	…	…	…
	99	8778.814	3883.778	1332.480	1091.725	697.483	241.485
	100	15291.340	7851.650	2534.924	1830.718	1519.926	442.369
		H1	H2	H3	R1	R2	R3
Radial	1	9452.421	4886.658	2713.418	1709.632	968.652	837.188
	2	8927.791	5775.201	3503.986	1415.498	1274.050	1121.364
	…	…	…	…	…	…	…
	99	6091.049	3188.418	1079.992	1091.725	697.483	241.485
	100	10741.470	6587.421	2079.908	1830.718	1519.926	442.369
		H1	H2	H3	S1	S2	S3
Struts	1	2020.409	831.240	281.247	-1207.785	-941.683	-379.918
	2	2946.826	1206.958	379.722	-1817.063	-1354.235	-429.386
	…	…	…	…	…	…	…
	99	2432.193	976.260	486.024	-1478.619	-978.630	-911.769
	100	3051.062	1401.979	688.145	-1773.837	-1626.241	-1268.992

Table 6. The prediction value under different construction processes

Prediction times	Tension hoop cable/($\times 10^4$/EA$_j$)			Tension radial cable/($\times 10^4$/EA$_j$)			Jack struts/($\times 10^4$/EA$_j$)		
	H1	H2	H3	R1	R2	R3	S1	S2	S3
1	304.78	160.90	132.53	474.26	170.61	156.38	-1524.88	-995.28	-937.98
2	307.00	163.35	135.33	474.09	171.69	156.57	-1524.51	-995.61	-938.10
3	347.04	218.33	156.33	473.30	165.53	163.50	-1524.46	-996.00	-936.93
4	299.93	165.92	132.39	473.69	169.49	157.095	-1524.72	-995.45	-938.07
5	300.24	143.12	134.26	471.85	176.55	149.67	-1525.38	-995.60	-937.26

Table 6 shows that the results from the different prediction times are different. To find out the accuracy of the prediction values, this paper applied the prediction values $[P]_{5\times3}$ in Table 6 to the numerical model and output the corresponding internal force of the hoop cable at the initial state $\left[{}^P F_I^1, \quad {}^P F_I^2, \quad {}^P F_I^3 \right]_{5\times3}$. The relative errors between the prediction value $\left[{}^P F_I^1, \quad {}^P F_I^2, \quad {}^P F_I^3 \right]_{5\times3}$ and the known value $\tilde{N}$ under three different construction processes are obtained by the following Eq. 9. And, the results of the relative errors are shown in Table 7.

$$Error = |(P - \tilde{N}) / \tilde{N}| \times 100 \tag{9}$$

Table 7. The Prediction Errors of Three Different Construction Processes for Different Times

Prediction times	Tension hoop cable/(%)			Tension radial cable/(%)			Jack struts/(%)		
	H1	H2	H3	H1	H2	H3	H1	H2	H3
1	0.9604	1.9414	0.1525	0.4593	1.4835	0.3039	0.0009	0.0065	0.0026
2	1.8016	3.1890	1.6394	0.5156	1.7977	0.1188	0.0140	0.0007	0.0057
3	17.0820	27.2459	20.7601	0.0739	0.3013	2.0867	0.0161	0.0052	0.0692
4	0.0839	2.8397	0.0245	0.2980	1.1473	0.1452	0.0053	0.0025	0.0040
5	1.5764	4.1127	1.5597	0.3570	2.6503	2.5837	-0.0281	-0.0161	0.0388

Table 7 shows that the prediction errors are different after each prediction. Moreover, the partial prediction errors are large, such as 27.2459%, 20.7601% and 17.0820%. Thus, this paper selected the prediction values that correspond to the minimal prediction errors for the new range. From Table 7, we can see that the minimal prediction errors for tensioning hoop cables, radial cables and jacking struts appear in the 1st prediction, 4th prediction and 5th prediction, respectively. Additionally, the corresponding prediction values in Table 6 will be applied to Eq. 8 to obtain the new range for the training data. According to the new range, this paper generates 1000 patterns for three different construction processes randomly. Partial patterns from different construction processes are listed in Table 8.

Table 8. Partial Training Samples under Tensioning Radial Cable

Construction process	NO	Input data /kN			Output data/($\times 10^4$/EA$_j$)		
		H1	H2	H3	H1	H2	H3
Hoop	1	2680.105	1079.136	529.696	325.409	169.461	140.069
	2	2501.329	1047.818	479.478	298.013	175.046	122.271
	…	…	…	…	…	…	…
	999	2324.651	965.419	507.561	275.263	154.616	141.659
	1000	2376.157	969.901	477.306	284.363	154.926	127.860
		H1	H2	H3	R1	R2	R3
Radial	1	2414.133	987.197	497.898	452.023	167.222	159.386
	2	2396.334	964.696	464.533	451.746	162.410	144.450
	…	…	…	…	…	…	…
	999	2410.120	999.108	491.172	449.055	172.979	155.047
	1000	2395.793	965.541	457.816	451.619	163.387	140.965
		H1	H2	H3	S1	S2	S3
Struts	1	2444.214	1021.781	482.025	-1463.575	-1091.760	-875.070
	2	2479.843	999.123	481.570	-1508.682	-1014.435	-883.092
	…	…	…	…	…	…	…
	999	2573.127	988.632	469.207	-1599.524	-944.116	-844.347
	1000	2672.678	1012.820	488.722	-1673.499	-941.794	-885.315

To know the influence of the sample size on the prediction accuracy of the BP network, this paper selected the training data from 1000 patterns in sequence and created 19 groups of training data whose sizes are 10, 20, 30, 40, 50, 60, 70, 80, 90, 100, 200, 300, 400, 500, 600, 700, 800, 900, and 1000. Then, this paper applied these 19 groups of training data to the network without optimizing with the GA and predicted the output data that corresponds to the known input data $\tilde{N}$ according to the scheme in Figure 3. The partial prediction results, which are found from the samples of different sizes, correspond to three different construction processes at the zero state and are summarized in Table 9.

Table 9. The Prediction Values under Different Construction Processes

sample size	Tension hoop cable/($\times 10^4$/EA$_j$)			Tension radial cable/($\times 10^4$/EA$_j$)			Jack struts/($\times 10^4$/EA$_j$)		
	H1	H2	H3	R1	R2	R3	S1	S2	S3
10	276.606	149.411	148.956	458.904	163.600	156.247	-1538.206	-1045.117	-986.046
20	302.812	155.153	134.301	473.350	165.249	158.512	-1524.708	-995.024	-937.805
...	...	...	...	...	...	...	...	...	...
90	302.632	155.236	134.411	473.556	165.361	158.476	-1524.820	-995.431	-937.949
...	...	...	...	...	...	...	...	...	...
500	302.629	155.235	134.415	473.575	165.365	158.479	-1524.829	-995.443	-937.997
...	...	...	...	...	...	...	...	...	...
900	302.637	155.229	134.420	473.561	165.364	158.474	-1524.711	-995.430	-938.017
1000	302.627	155.237	134.412	473.558	165.359	158.477	-1524.810	-995.424	-937.989

Similar to the above process, this paper applied the prediction values $[P]_{19\times3}$ in Table 9 to the numerical model and output the corresponding internal force of the hoop cable at the initial state $\left[\begin{array}{ccc} {}^pF_I^1, & {}^pF_I^2, & {}^pF_I^3 \end{array}\right]_{19\times3}$. The results of the relative errors are shown in Figure 5.
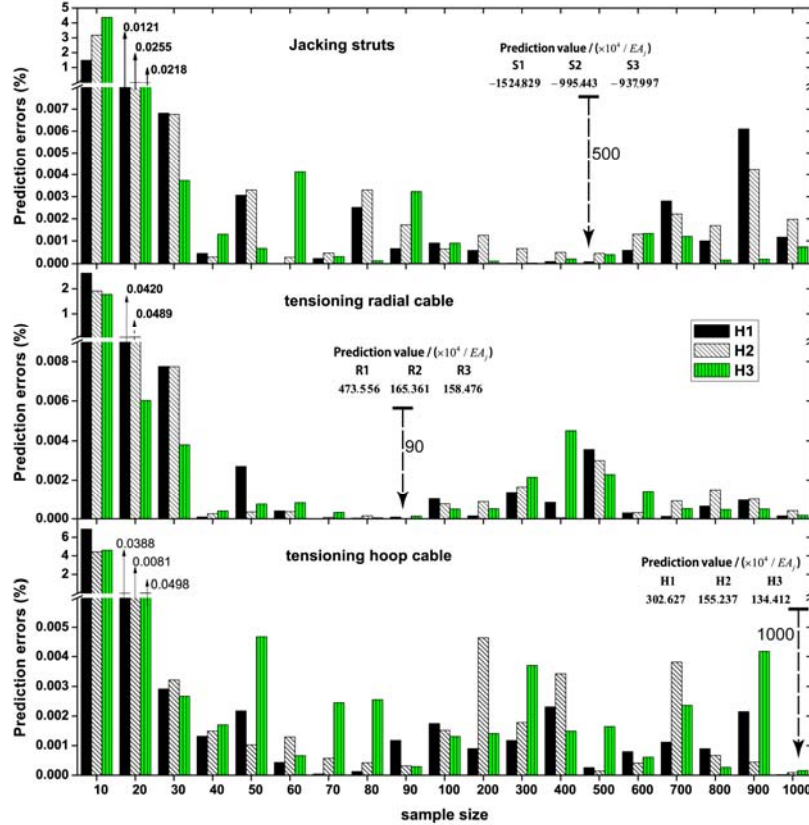
Figure 5. Distribution of the Prediction Errors from Different Construction Processes

The prediction errors in Figure 5 are significantly less than those in Table 7. Thus, the method for determining the range for the training data according to the previous prediction values is helpful for enhancing the prediction precision. At the same time, Figure 5 shows that the increase in the training sample size can generally enhance the prediction precision. The prediction errors are significantly reduced with the increase in the training sample size when the sample size is less than 40. However, after the sample size reaches a certain value, such as 50, the influence of the sample size on the prediction errors will decrease. When the sample size is equal to or greater than 50, the prediction errors of the tensioning hoop cables, tensioning radial cables and jacking struts are less than 0.005%,

0.005%, and 0.006%, respectively. In general, the BP network can accurately predict the results of the force finding for the suspended-dome. At the same time, from Figure 5, we can see that the prediction errors are minimal when the sample size is 1000, 90, and 500 for the tensioning hoop cables, radial cables and jacking struts. The corresponding results of the force finding are listed in Table 9. The sample size that corresponds to the minimal prediction error is not always the maximal size of 1000. At the same time, Table 6 and Table 7 show that the same network and same training data gained different prediction results after each prediction, and the prediction errors vary from 0.0245% to 27.2459%. The main cause of this result is that the random numbers initialized the connection weights and thresholds for the training.

To evaluate the influence of the initial weights and thresholds on the prediction, in this study, we selected 1000 sample data on tensioning the radial cables and used the genetic algorithm (GA) mentioned in section 4 to optimize the 30 weights and eight thresholds of the BP. Then, we trained and predicted the values that correspond to the known values 10 times, according to the scheme in Figure 3.

During the optimization, we took the sum of the errors between the output data and the corresponding prediction values as the fitness of the optimization, which can be expressed as follows:

$$f(i) = \sum_{l=1}^{s} \sum_{j=1}^{3} \left(\left| {}^{i}F_z^{jl} - {}_{p}^{i}F_z^{jl} \right| \right) \tag{10}$$

Each run of the GA is conducted for 40 ($i=1,2,\cdots40$) generations while using a population size of 80 ($s=80$). Proportional selection is employed to probabilistically select genotypes for crossover and mutation. Two pairs for a pairwise single-point crossover operation and uniform mutation operations were used. The crossover rate and the mutation rate were empirically set to 0.3 and 0.2.

We also applied 1000 sample data to the network without optimizing by the GA to predict the output data that corresponds to the known input data 10 times. The goal in this case was to compare the prediction results between the BP optimized by GA and the BP without optimization. The prediction values from only the BP network and the BP network optimized by the GA are summarized in Table 10.

Table 10. The Prediction Value for Tensioning Radial Cables by BP and BP+GA

| times | Initial strain at the zero state /($\times10^4$/EA$_j$) | | | | | |
| | BP | | | BP+GA | | |
	R1	R2	R3	R1	R2	R3
1	473.5541	165.3572	158.4735	473.5555	165.3614	158.4769
2	473.5494	165.3471	158.4798	473.5536	165.3606	158.4799
3	473.5671	165.3658	158.4801	473.5561	165.3612	158.4764
4	473.5581	165.3546	158.4758	473.5553	165.3614	158.4769
5	473.5534	165.3614	158.4744	473.5537	165.3604	158.4801
6	473.5567	165.3695	158.4839	473.5561	165.3612	158.4765
7	473.5598	165.3539	158.4807	473.5556	165.3613	158.4769
8	473.5498	165.3392	158.4725	473.5560	165.3612	158.4764
9	473.5593	165.3605	158.4756	473.5560	165.3612	158.4764
10	473.5502	165.3603	158.4795	473.5516	165.3602	158.4804
Mean value(μ)	473.5558	165.3570	158.4776	473.5549	165.3610	158.4777
standard deviation(σ)	0.0056	0.0089	0.0037	0.0015	0.0004	0.0017

Table 10 shows that the prediction values are different each time. In other words, the BP network with the same structure and the same training data has different prediction errors after different trainings. At the same time, we can see that the standard deviation σ of BP+GA is significantly less than that of BP. Thus, the prediction stability of the BP network will be improved after optimization by GA.

To know the prediction errors from BP and BP+GA, we applied the prediction values in Table 10 to the numerical model and obtained the internal force at the initial state; then, we calculated the relative errors by Eq. 9. The prediction errors are shown in Figure 6.
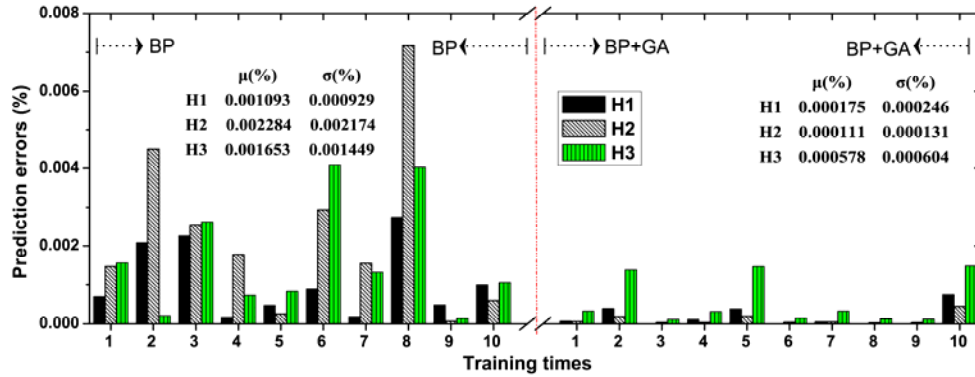
Figure 6. Prediction Errors of BP and BP+GA for Different Times

Figure 6 shows that the prediction errors are different even though the network structure and the training data are the same, especially for the prediction from BP without optimization by GA. The uniformity of the results is significantly improved after the initial weights and thresholds are optimized. The corresponding standard deviation σ was reduced by 26.48%, 6.03% and 41.68% after optimization. The mean values μ of the prediction errors also decreased by 16.01%, 4.86% and 34.97%. In general, the BP network optimized by GA became more accurate and stable for prediction. The optimization by GA, however, requires much more calculation time.

5.   CONCLUSIONS

Based on this study, a method for the force finding of suspended-dome and some advice on the application of BP in the force finding can be obtained. The conclusions and suggestions are as follows:

(1) The construction process should be considered during the force finding of the suspended-dome because the appearance of pre-stress in the suspended-dome is related to it.

(2) The BP network can address the force finding of the suspended-dome, which is a problem category that cannot be formulated as an algorithm.

(3) A BP network can accurately predict the results of the force finding for the suspended-dome, and the prediction accuracy will become higher and higher while there is an increase in the training data size. Restricting the range of the training data according to the previous prediction results can also increase the prediction precision significantly.

(4) Prediction results from the BP are different after repeated prediction regardless of its unchanged structure and training data because the initial weights and thresholds are generated randomly. After the initial weights and thresholds are optimized by the GA, the uniformity and the stability of the prediction results will be improved significantly. However, the optimization procedure will cost much more time.

(5) The BP network for force finding in this paper is a small-scale network. For a large-scale network, the determination of its network structure, especially the number of hidden layers and the node for each hidden layer, must be further studied.

ACKNOWLEDGEMENTS

REFERENCES

[1]   Gómez, J.V., "Tensegrity Structures and their Application to Architecture", MS thesis, School of Architecture, Queen's University Belfast, 2004.

[2]   Pellegrino, S., "A Class of Tensegrity Domes", International Journal of Space Structures,1992, Vol. 7, No. 2, pp.127-143.

[3]   Kawaguchi, M., Abe, M. and Hatato, T., "On a structural system "suspen-dome " System", Proceedings of IASS Symposium, Marid, Spain, 1993, pp. 523-530.

[4]   Chen, Z.H., Wu, Y.J. and Yin, Y., et al, "Formulation and application of multi-node sliding cable element for the analysis of Suspen-Dome structures", Finite Elements in Analysis and Design, 2010, Vol. 46, No. 9, pp. 743-750.

[5]   Kang, W.J., Chen, Z.H. and Lam, H.F., et al, "Analysis and Design of the General and Outmost-ring Stiffened Suspendome Structures", Engineering Structures, 2003, Vol. 25, No. 13, pp. 1685-1695.

[6]   Kawaguchi, M., Abe, M. and Tatemichi, I., "Design, Test, and Realization of "Suspend-Dome" System", Journal of IASS, 1999, Vol. 40, No. 131, pp. 179-192.

[7]   Zhang, Z.H., Cao, Q.S. and Dong, S.L., "Structural Design of a Practical Suspendome", Advanced Steel Construction, 2008, Vol. 4, No. 4, pp. 323–340.

[8]   Dong, S.L., Yuan, X.F. and Guo, J.M. et al, "Experimental Research on Tension Process of Suspen-dome Structural Model", Spatial Structure, 2008, Vol. 14, No. 4, pp. 57-62.

[9]   Tibert, A.G. and Pellegrino, S., "Review of Form-finding Methods for Tensegrity Structures", International Journal of Space Structures, 2003, Vol. 18, No. 4, pp. 209-223.

[10]   Xu, X. and Luo, Y.Z., "Form Finding of Tensegrity Systems Using Simulated Annealing Algorithm", Journal of structural engineering, ASCE, 2010, Vol. 136, No. 8, pp. 1027-1031.

[11]   Cao, Q.S. and Zhang, Z.H., "A Simplified Strategy for Force Finding Analysis of Suspendomes", Engineering Structures, 2010, Vol. 32, No. 1, pp. 306-318.

[12]   Zhuo, X., Zhang, G.F. and Ishikawa, K., et al, "Tensile Force Correction Calculation Method for Prestressed Construction of Tension Structures", Journal of Zhejiang University, 2008, Vol. 9, No 9, pp. 1021-1027.

[13]   Guo, J.M., Dong, S.L. and Yuan, X.F., "Morphological Analysis of Suspend-dome Structures and Its Practical Analysis Method", China Civil Engineering Journal, 2009, Vol. 41, No. 12, pp.1-7. (in Chinese).

[14]   Tsai, C.P., Lin, C. and Shen, J.N., "Neural Network for Wave Forecasting Among Multi-stations", Ocean Engineering, 2002, Vol. 29, No. 13, pp. 1683-1695.

[15]   Xu, J.X., Zhao, J.C., and Wang, W.Z., et al., "Prediction of Temperature of Tubular Truss under Fire Using Artificial Neural Networks", Fire. Safety Journal, 2013, Vol. 56, pp. 74-80.

[16]   CECS 212-2006, "Technical Specification for Pre-stressed Steel Structure" China Plan Press, Beijing, 2006. (in Chinese).

[17]   Kriesel, D., "Neural Networks", Dkriesel.com, 2005.

[18]   Gao, D.Q., "On Structures of Supervised Linear Basis Function Feed Forward Three-layer Neural Networks", Chinese Journal Computer, 1998, Vol. 21, No. 1, pp. 80-86. (in Chinese).

SIMPLE APPROACH FOR PERFORMANCE-BASED FIRE SAFETY DESIGN OF CIRCULAR CFT COLUMNS IN LARGE ENCLOSURE

Ruolin Wang [1] , Chao Zhang [2,*] and Guo-qiang Li [3]

[1] School of Civil Engineering, Wuhan University, Wuhan, China, 430072
[2] College of Civil Engineering, Tongji University, 1239 Siping Road, Shanghai 200092, China
[3] Sate Key Laboratory for Disaster Reduction in Civil Engineering, Tongji University, China
*(Corresponding author: E-mail: 08_chao_zhang@tongji.edu.cn))

ABSTRACT: The usage of concrete filled steel tubular (CFT) columns in large space buildings is increasing. Flashover is unlikely to happen in a large enclosure and the localized fire model is preferable to model the fire environment in a large enclosure fire. This paper proposed a simple approach to evaluate the fire resistance of circular CFT columns in localized fires. Simple model was provided to calculate the column temperatures in a localized fire. The concept of equivalent fire severity or time equivalent was used to correlate the localized fires with the standard fire. The simple model used in the Chinese code was used to calculate the load capacity of the circular CFT columns subjected to the equivalent standard fire exposure. The proposed approach, by correlating real fires with the standard fire, only includes heat transfer analysis and avoids the complex structural analysis, which provides an easy and efficient way for performance-based fire safety design. A case study is also provided to demonstrate the application of the approach.

Keywords: Concrete filled steel tubular (CFT) columns, Fire resistance, Large enclosure, Localized fires, Simple method, Time equivalent, Performance-based design

1.   INTRODUCTION

Concrete-filled steel tubular (CFT) columns have many advantages, including high load carrying capacity, fast construction, small cross-section, and high fire resistance. These attractions have enabled CFT columns to be used in many large space, and high-rise buildings [1].

Traditionally, the fire resistance of CFT columns is determined by a standard fire resistance test conducted on an isolated member subjected to a specified heating such as ASTM E119, ISO834. The standard fire resistance test is time consuming and expensive, and the dimension of the test specimen is limited by the size of the furnace. As an alternative to the test method, calculation approaches are also developed to assess the fire resistance of CFT columns [1-5]. Lie and Chabot [2] developed a mathematical model to calculate the temperatures and fire resistance of circular CFT columns. In the model, the cross-section area of the column was subdivided into a number of concentric layers to calculate the column temperatures, and a finite difference method was applied to solve the heat transfer equations. The strength and stiffness was calculated by subdividing the cross-section area into a number of annular elements. The representative temperature of an element was taken as the average temperature of the layer in which the element was located. In the Eurocode EC4-1-2 [3], a simple model is provided in the Annex H to calculate the fire resistance of CFT columns by subdividing the cross-section area into several elements and respectively calculate the strength and stiffness accordingly. Kodur [4] proposed a simplified equation based on the results of parameter studies supported by an experimental program on circular and square CFT columns under fire. The equation is widely used in North America, and it directly provides the fire

resistance time of the column in minutes as a function of different parameters such as the concrete strength, the column diameter and effective length, the type of concrete filling, cross-sectional shape and percentage of steel reinforcement [5]. Han and co-workers [1] proposed a formulation to determine the strength index of CFT columns based on regression analysis of the results of parametric and experimental studies. The formulation is incorporated in the Chinese technical code CECS200 [6] for fire safety design [7].

The behavior of a real fire is complex, which depends on many parameters such as active fire detection and suppression systems (smoke detector and sprinkler), fire loads (amount and distribution), combustion, ventilation, compartment size and geometry, and thermal properties of compartment boundaries [8]. In large enclosures, flashover (which is the rapid transition between a local fire and a general conflagration within a compartment when all fuel surfaces are burning [9]) is unlikely to happen, and the potential fires are characterized as pre-flashover or localized fires [10]. The current methods to calculate the fire resistance of CFT columns are developed for post-flashover fires, and there is no available simple method for calculation in localized fires.

This paper proposes a simple method to evaluate the fire resistance of circular CFT columns in localized fires. Simple model to calculate the temperatures of circular CFT columns in localized fires was provided. The concept of equivalent fire severity or time equivalent was used to relate real fires with a standard fire. The simple method given in CECS200 [6] was applied to calculate the fire resistance of circular CFT columns in the standard fire. A case study for the performance-based fire safety design of the circular CFT columns in a railway station building was presented to demonstrate the application of the proposed method.

2.   LARGE ENCLOSURE FIRE

2.1   Localized Fire Model

Localized fire model is used to model the fire environment in a large enclosure. As shown in Figure 1, a localized fire is loosely divided into the lower combustion (flame) and the upper non-combustion (plume) regions. The ceiling jet is also illustrated.
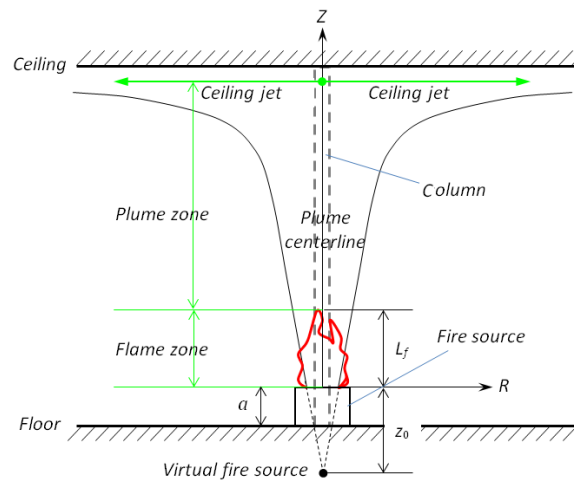
Figure 1. Illustration of a Localized Fire Model

The centerline gas temperature, T_g, in a localized fire is calculated by [10]

$$T_g = 20 + \min(\Delta T_{plume}, \Delta T_{flame}) \tag{1}$$

where ΔT_{plume} is the plume centerline temperature increment calculated by [11]

$$\Delta T_{plume} = 20 + 0.25(1000 \dot{Q}_c)^{2/3} (z - z_0)^{-5/3} \tag{2}$$

and ΔT_{flame} is the flame centerline temperature increment, as calculated by Quintiere and Grove [12]. For simple calculation [13]

$$\Delta T_{flame} = 1500(1 - \chi_r) \tag{3}$$

where $\dot{Q}_c = (1 - \chi_r)\dot{Q}$ is the convective part of the heat release rate (*HRR*) of the fire source, in which $\dot{Q}$ is the *HRR* of the fire source and χ_r is the radiative fraction. For situations where χ_r is unknown, the flame centerline temperature may be simply taken as 900 °C as in EC1-1-2 [11]. z_0 is the height of the virtual fire source, calculated by

$$z_0 = -1.02D + 0.083\dot{Q}^{2/5} \tag{4}$$

where $D = \sqrt{4A/\pi}$ is the equivalent diameter of the fire, in which A is the area of the fire source.

Eq. 3 assumes that all of the air entrainment into the flame zone is completely consumed. However, in practice, with increasing height the amount of air entrainment will become more than that of the air required for reaction and the exceeded air will cool the flame zone temperature.

2.2   Heat Release Rate and Fire Duration

Heat release rate (*HRR*) is the most import variable in measuring fire severity. The *HRR* of a real fire can be measured by cone calorimeter. In design work, the Natural Fire Safety Concept (*NFSC*) is widely used to represent the fire conditions [11,14-17]. As shown in Figure 2, the *NFSC* fire is assumed to be t-square in the growth stage and decay stage begins at the time when 70% of design fire load is consumed.
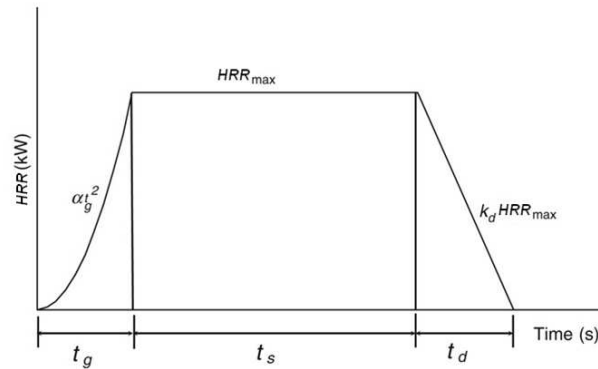
Figure 2. Illustration of the *HRR* History in a NFSC Fire

In a *NFSC* fire, at the growth stage, the *HRR* is given by

$$HRR = \alpha t^2 \tag{5}$$

the fire growth time, t_g, is given by

$$t_g = \sqrt{\frac{HRR_{max}}{\alpha}} \tag{6}$$

and the fuel energy consumed at the fire growth stage, Q_g, is

$$Q_g = \int_0^{t_g} \alpha t^2 dt = \frac{\alpha t_g^3}{3} \tag{7}$$

where α is the fire intensity coefficient, taken as 0.00293 kW/s^2, 0.0117 kW/s^2 and 0.0466 kW/s^2 for slow, medium and fast growth fires, respectively.

The duration time of steady burning in a *NSFC* fire is given by

$$t_s = \frac{0.7 q_f A_f - Q_g}{HRR_{max}} \tag{8}$$

and the duration of decaying stage is given by

$$t_d = \frac{0.6 q_f A_f}{HRR_{max}} \tag{9}$$

where q_f, A_f are design fire load density and floor area, respectively; and HRR_{max} is the maximum heat release rate. In EC1-1-2 [11], values for fire load density and maximum heat release rate per unit area for various occupancies are provided.

The total duration time of an NFSC fire is given by

$$t_f = t_g + t_s + t_d \tag{10}$$

3.   TEMPERATURE OF CIRCULAR CFT COLUMNS

In current structural fire design codes, there is no calculation approach to predict the temperature of circular CFT columns in a localized fire. Here, the simplifications and assumptions for calculation in post-flashover fires [8,18-19] were applied to calculate the temperature of a circular CFT column fully engulfed in a localized fire,

- The temperature of the gas surrounding a column is calculated by Eq. 1;
- For calculating radiative heat transfer from a fire to the column surface, the surrounding gas and the exposed surface are represented as infinitely parallel grey planes, and the view factor is, therefore, taken as 1;
- The convective heat transfer from a fire to the column surface is calculated by Newton's law of cooling.

Correspondingly, the heat flux to an exposed column surface is

$$\dot{q}''_{net} = \dot{q}''_{c} + \dot{q}''_{r} \tag{11}$$

where $\dot{q}''_{c}$ and $\dot{q}''_{r}$ are convective and radiative heat fluxes, calculated by

$$\dot{q}''_{c} = h_{c}(T_{g} - T_{surf}) \tag{12}$$

and

$$\dot{q}''_{r} = \varepsilon_{res}\sigma[(T_{g} + 273)^{4} - (T_{surf} + 273)^{4}] \tag{13}$$

where h_{c} is the convective heat transfer coefficient, taken as 9 W/(m²K) for localized fires [11]; T_{surf} is the column surface temperature; ε_{res} is the resultant emissivity at the exposed surface; and σ is the Stefan-Boltzmann constant. For calculating in a standard fire, the gas temperature T_{g} is taken as the fire temperature.

Ignoring the thermal conduction along column length, the temperatures in a cross section of the circular CFT column are calculated by solving the two-dimensional heat conduction equation under the heat flux boundary condition below,

$$-k_{s}\frac{\partial T}{\partial s}(0,t) = \dot{q}''_{net} \tag{14}$$

where s denotes the inward radial direction; and k_{s} is the thermal conductivity of the steel. At the steel-concrete interface, temperature continuity is assumed. The cross sections engulfed by flame have the maximum temperatures.

Although the correlations in Eq.1 are derived for a localized fire that is burning without obstruction (like a column), the above approach is recommended for simple calculation because of the following reasons:

- The approach is conservative. The gas temperatures in a horizontal plane of a fire plume decrease with plume radius. The approach uses the maximum gas temperature at the plume center for calculation. Also, ignoring the thermal conduction along column length yields higher maximum cross section temperatures [20].
- The present of the circular CFT column does not affect the flame temperature, ΔT_{flame} in Eq.1, although it affects the plume temperature.

4.   FIRE RESISTANCE OF CFT COLUMNS IN THE STANDARD FIRE

The calculation method proposed by Han et al. [1] is incorporated in the Chinese code CECS200 [6] to evaluate the fire resistance of CFT columns.

In [6], a strength index, k_{t}, is defined to quantify the strength of the CFT columns subjected to standard fire, which is expressed as

$$k_t = \frac{N_u(t)}{N_u} \tag{15}$$

where $N_u(t)$ is the ultimate strength corresponding to the fire resistance time t of the CFT columns; and N_u is the ultimate strength of the CFT columns at normal temperatures, which can be calculated using the equations given by design codes.

For the CFT columns without fire protection, the strength index can be calculated by the following expressions as [1]

$$k_t = \frac{1}{1 + at_0^{2.5}}, \quad \text{for} \quad t_0 \leq t_1 \tag{16a}$$

$$k_t = \frac{1}{bt_0 + c}, \quad \text{for} \quad t_1 < t_0 \leq t_2 \tag{16b}$$

$$k_t = kt_0 + d, \quad \text{for} \quad t_0 > t_2 \tag{16c}$$

with
$$a = (-0.13\lambda_0^3 + 0.92\lambda_0^2 - 0.39\lambda_0 + 0.74)(-2.85D_0 + 19.45)$$
$$b = D_0^{-0.46}(-1.59\lambda_0^2 + 13.0\lambda_0 - 3.0); \quad c = 1 + at_1^{2.5} - bt_1; \quad d = 1/(bt_2 + c) - kt_2$$
$$k = (0.02\lambda_0^3 - 0.31\lambda_0^2 + 1.46\lambda_0 + 0.03)(0.01D_0^3 - 0.12D_0^2 + 0.48D_0 - 0.59)$$
$$t_1 = (0.0072D_0^2 - 0.02D_0 + 0.27)(-0.0131\lambda_0^3 + 0.17\lambda_0^2 - 0.72\lambda_0 + 1.49)$$
$$t_2 = (0.01D_0^2 - 0.03D_0 + 0.39)(-0.03\lambda_0^3 + 0.31\lambda_0^2 - 1.12\lambda_0 + 1.89)$$
$$t_0 = t/100; \quad D_0 = D_c/400; \quad \lambda_0 = \lambda/40$$

where D_c is the diameter of the circular section; and λ is the slenderness ratio.

Taking Eq. 10 into Eq. 9, we obtain the ultimate strength $N_u(t)$ of the unprotected CFT columns corresponding to fire resistance time t.

5.   TIME EQUIVALENT METHOD

The concept of equivalent fire severity, commonly referred as time equivalent, is used to relate the severity of an expected real fire to the standard fire. So that results or methods based on the standard fire can be extended to realistic fires. To date, a number of methods and empirical formulae have been developed for evaluating the equivalent fire severity. These methods include equal area method, maximum temperature method, minimum load capacity concept and energy based method [14,21]. Take the maximum temperature method for example, as illustrated in Figure 3, the equivalent time of a real fire is the time when a structural element is subjected to the standard fire exposure that would give the same critical temperature as the maximum temperature the structural element will get when subjected to the real fire exposure.

In CECS200 [6] and in EC1-1-2 [11], equations based on the maximum temperature method are recommended to calculate the time equivalent. Those equations, however, are developed for calculation in fully-developed compartment fires in which the gas temperatures are approximately uniform because of flashover. In this study, the maximum temperature method was applied to calculate the time equivalent in localized fires.
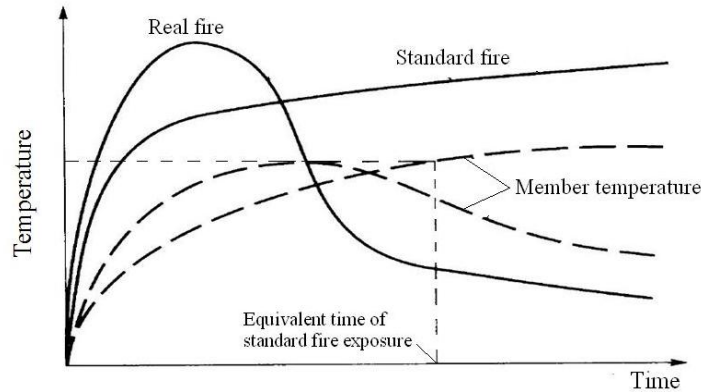
Figure 3. Illustration of the Maximum Temperature Method to Calculate Time Equivalent

Therefore, the fire resistance of a circular CFT column in a large enclosure can be evaluated by following the steps given below:

- Step 1: Determine the design fire scenarios (e.g. fire load density, fire type, *HRR*, location and area of the fire load) by fire risk analysis;
- Step 2: Calculate the fire durations (by Eq. 10) and gas temperatures (by Eq. 1) in the design fires;
- Step 2: Calculate the temperatures of the column in the design fires and obtain the maximum temperature time curve in design fires;
- Step 3: Calculate the temperature of the column in the standard fire and obtain the equivalent standard fire exposure time by maximum temperature method;
- Step 4: Calculate the strength index of the circular CFT column k_t by Eq. 16;
- Step 5: Calculate the ultimate strength of the column in the design fire $N_u(t)$ from Eq. 9 (The ultimate strength of the column at normal temperature N_u is calculated separately);
- Step 6: Check the load bearing capacity of the circular CFT column in the design fires by comparing $N_u(t)$ with the action force in the design fire P_T. If $N_u(t)$ is greater than P_T, the circular CFT column has sufficient load capacity in the design fire scenario and can be left unprotected; and if $N_u(t)$ is less than P_T, the circular CFT column has insufficient load capacity and should be protected.

6.   A CASE STUDY

Problem: Figure 4 shows the bird view of a railway station building in China. The building has a construction area of about 182340 m² and a height of about 56.6 m. Circular CFT columns were used to support the roof structure of the building. The dimensions of the circular CFT columns are 16 m (height) × 1600 mm (diameter) × 60 mm (tube thickness). The filled concrete is plain weight normal concrete (NWC). Performance-based approach was approved and used in the fire safety design of the building. By fire risk analysis, the most hazard fire to the circular CFT columns is a shopping center fire. Determine the strength index of the column in the design fire.

Solution:

1) Calculate the fire duration time t_f. For shopping center, the floor fire load density is taken as $q_f = 1300$ MJ/m² according to CECS200 [6], and the fire intensity coefficient and the maximum heat release rate are $\alpha = 0.0466$ kW/s², $HRR_{max} = 250$ kW/m² according to EC1-1-2 [11]. Therefore,

$$t_g = \sqrt{\frac{HRR_{max}}{\alpha}} = \sqrt{\frac{250}{0.0466}} = 73 \text{ s}$$

$$t_s = \frac{0.7q_f A_f - Q_g}{HRR_{max}} = \frac{0.7 \times 1300 \times 1000 - 1/3 \times 250 \times 73}{250} = 3616 \text{ s}$$

$$t_d = \frac{0.6q_f A_f}{HRR_{max}} = \frac{0.6 \times 1300 \times 1000}{250} = 3120 \text{ s}$$

$$t_f = t_g + t_s + t_d = 73 + 3616 + 3120 = 6809 \text{ s}$$

2) Calculate the temperature of the circular CFT column in the design fire. The finite element method (FEM) program ANSYS is used to solve the heat transfer problem. 2D thermal solid element PLANE55 and thermal surface effect element SURF151 as used in a previous work [18] were applied in the numerical simulations. Figure 5 shows the FE model for the circular CFT column. Using symmetry, a partial section instead of the whole section was considered. A constant flame temperature of 900 ºC was used for the duration of the design fire. Figure 6 shows results for temperature distributions in the circular CFT column when exposed to the design fire.

3) Calculate the equivalent standard fire duration time t_{eq}. As shown in Figure 7, by maximum temperature method $t_{eq} = 86$ min. Figure 8 compares the temperature distributions in the circular CFT column exposed to the design fire and the standard ISO 834 fire. The steel temperatures are approximately equal in the two fires, while the concrete temperatures in the design fire are slightly higher than those in the standard ISO 834 fire. Considering the concrete temperatures were comparatively low, and many conservative assumptions were used in the calculation, an equivalent standard fire duration time of 90 min was used to calculate the strength index of the column in fire condition.

4) Calculate the strength index. Taking $t = 90$ min, $D_c = 1600$ mm and $\lambda = 4L/D = 40$ into Eq. 16, we get $t_0 = 0.9$, $D_0 = 4$, $\lambda_0 = 1$, $t_1 = 0.283$, $t_2 = 0.452$, $k = 0.06$, $a = 9.18$, $b = 4.44$, $c = 0.133$, $d = 0.44$, and $k_t = 0.494$.

Figure 4. A Railway Station Building in China

The above calculation shows that by using performance-based approach, the fire resistance requirement for the circular CFT columns was reduced from 3.0 h as specified in the prescriptive code to 1.5 h. By comparing the design load with the load bearing capacity of the circular CFT columns in the design fire, the CFT columns without fire protection were found to have sufficient fire resistance.
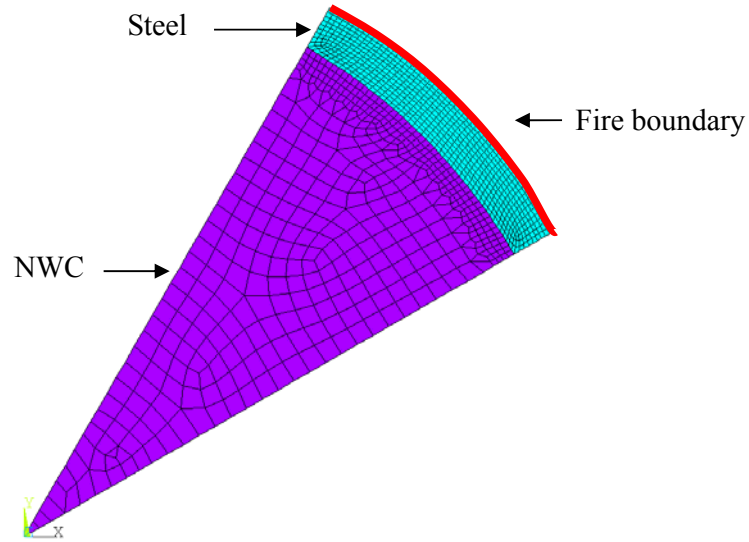
Figure 5. FEM Model for Heat Transfer Analysis

(a) 900 s

(b) 1800 s

(c) 3600 s

(b) 6809 s
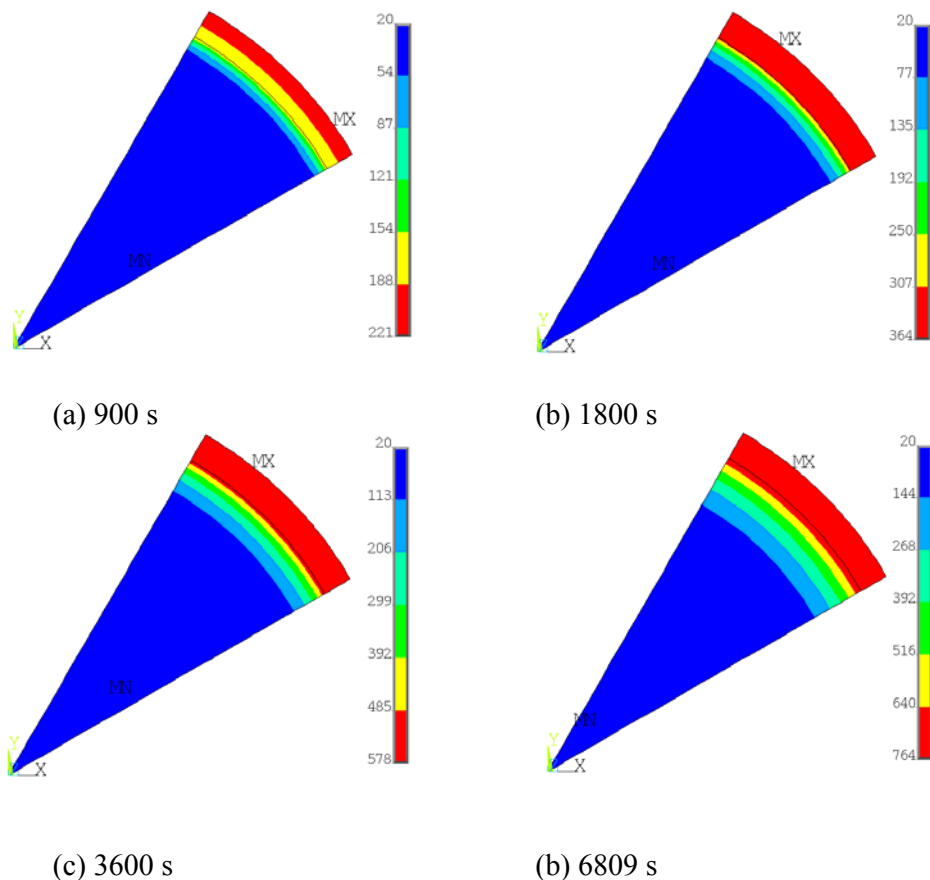
Figure 6. Temperature Distributions in the Circular CFT Column Exposure to the Design Fire
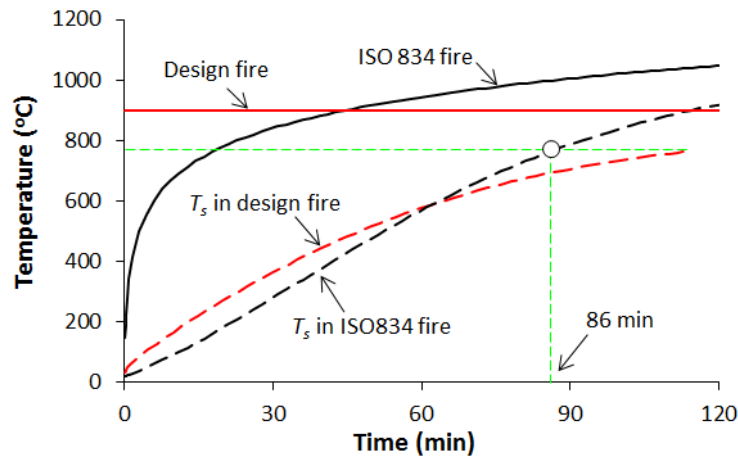
Figure 7. The Equivalent Standard Fire Exposure Time Determined by t-equivalence
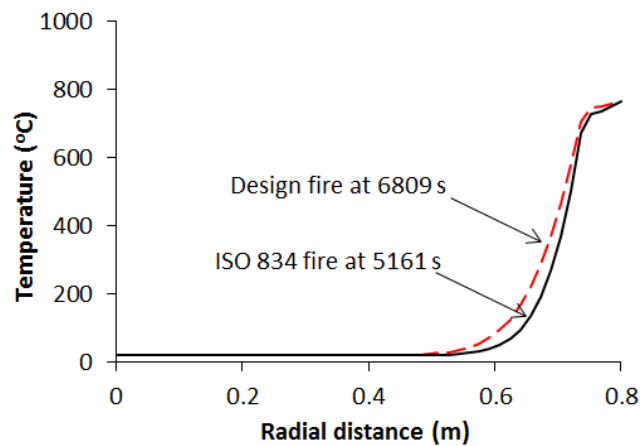
Figure 8. Temperature Distributions along the Radius

7.   CONCLUSIONS AND SUGGESTIONS

The usage of concrete filled steel tubular (CFT) columns in large space buildings is rapidly increasing in recent years. There are many situations in which the performance-based methods (PBM) are applied to do the fire safety design of large space buildings. The interest in the use and development of simple methods for calculating the fire resistance of CFT columns is growing, due to the application of PBM. This paper proposed a simple approach to calculate the fire resistance of circular CFT columns in localized fires. The theory and assumptions of the approach are stated, and the usage of the approach is demonstrated by a case study example.

The approach uses the concept of equivalent fire severity to correlate localized fires with the standard fire. The time equivalent is calculated by the maximum temperature method which is used in both the Chinese and the European codes. Although the fire performance of a circular CFT column is affected by many parameters, the limiting or critical (steel) temperature method is used in practice to evaluate fire resistance of circular CFT columns, e,g. [22]. Therefore, the proposed approach which is also based on the limiting (steel) temperature method is recommended for simple calculations. Users, however, are advised to check the safety of results by, for example, comparing the temperature distributions in the cross section.

ACKNOWLEDGEMENTS

REFERENCE

[1]   Han, L.H., Zhao, X.L., Yang, Y.F. and Feng, J.B., "Experimental Study and Calculation of Fire Resistance of Concrete-filled Hollow Steel Columns", Journal of Structural Engineering - ASCE, 2003, Vol. 129, pp. 346-56.

[2]   Lie, T.T. and Chabot, M., "A Method to Predict the Fire Resistance of Circular Concrete Filled Hollow Steel Columns. Journal of Fire Protection Engineering, 1990, Vol. 2, pp. 111-26.

[3]   EC4-1-2. Eurocode 4 – Design of Composite Steel and Concrete Structures – Part 1-2: General Rules – Structural Fire Design. British Standards, 2005.

[4]   Kodur, V.K.R., "Performance-based Fire Resistance Design of Concrete-filled Steel Columns", Journal of Constructional Steel Research, 1999, Vol. 51, pp. 21-36.

[5]   Espinos, A., Romero, M.L. and Hospitaler, A., "Simple Calculation Model for Evaluating the Fire Resistance of Unreinforced Concrete Filled Tubular Columns", Engineering Structures, 2012, Vol. 42, pp. 231-44.

[6]   China Association for Engineering Construction Standardization (CECS200), Technical Code for Fire Safety of Steel Structure in Buildings (in Chinese), Beijing, China Planning Press, 2006.

[7]   Li, G.Q. and Zhang, C., "The Chinese Performance-based Code for Fire-resistance of Steel Structures", International Journal of High-Rise Buildings, 2013, Vol. 2, pp. 123-30.

[8]   Zhang, C. and Li, G.Q., "Modified One Zone Model for Fire Resistance Design of Steel Structures", Advanced Steel Construction, 2013, Vol. 9, pp. 284-99.

[9]   Drysdale, D., "An Introduction to Fire Dynamics, 2nd edition, John Wiley and Sons, 1999.

[10]   Zhang, C., and Li, G.Q., "Fire Dynamic Simulation on Thermal Actions in Localized Fires in Large Enclosure", Advanced Steel Construction, 2012, Vol. 8, pp. 124-36.

[11]   EC1-1-2. Eurocode 1: Actions on Structures – Part 1-2: General Rules – Actions on Structures Exposed to Fire, British Standards, 2002.

[12]   Quintiere, J.G. and Grove, B.S., "A Unified Analysis for Fire Plumes", 27th Symposium (International) on Combustion, The Combustion Institute, 1998, pp. 2757-66.

[13]   Zhang, C., and Li, G.Q., Simple Formulae for Calculating the Gas Temperature in Large Enclosure Fire Environment", Fire Safety Science, 2012, pp. 2175-82. (In Chinese)

[14]   Li, G.Q. and Zhang, C., "Simple Approach for Calculating Maximum Temperature of Insulated Steel Memebrs in Natural-fires", Journal of Constructional Steel Research, 2012, Vol. 71, pp. 404-10.

[15]   Zhang, C., Li, G.Q. and Usmani, A., "Simulating the Behavior of Restrained Steel Beams to Flame Impingement from Localized-fires", Journal of Constructional Steel Research, 2013, Vol. 83, pp. 156-65.

[16]   Zhang, C., Gross, J.L. and McAllister, T.P., "Lateral Torsional Buckling of Steel W-beams Subjected to Localized Fires", Journal of Constructional Steel Research, 2013, Vol. 88, pp.330-8.

[17]   Zhang, C., Gross, J.L., McAllister, T.P. and Li, G.Q., "Behavior of Unrestrained and Restrained Bare Steel Columns Subjected to Localized Fire", Journal of Structural Engineering –ASCE, 2014. Doi: 10.1061/(asce)st.1943-541X.0001225

[18]   Li, G.Q. and Zhang, C., "Thermal Response to Fire of Uniformly Insulated Steel Members: Background and Verification of the Formulation Recommended by Chinese Code CECS200", Advanced Steel Construction, 2010, Vol. 6, pp. 788-802.

[19]   Zhang, C., Li, G.Q. and Wang, Y.C., "Sensitivity Study on Using Different Formulae for Calculating the Temperature of Insulated Steel Members in Natural Fires", Fire Technology, 2012, Vol. 48, pp. 343-66.

[20]   Zhang, C. and Usmani, A., "Heat Transfer Principles in Thermal Calculation of Structures in Fire", Fire Safety Journal, 2015, Vol.78, pp. 85-95.

[21]   Buchanan, A.H., "Structural Design for Fire Safety", John Wiley and Sons Ltd., 2002.

[22]   Rush, D., Bisby, L. and Jowsey, A., "Evaluating Design Guidance for Intumescent Fire Protection of Concrete Filled Steel Hollow Sections", Proceedings of the 8th International Conference on Structures in Fire (SiF'14), Shanghai, China, June 2014, pp.1071-8.

EXPERIMENTAL STUDY ON
CONFINED BUCKLE PROPAGATION

Peter Stephan [1], Casey Love [1], Faris Albermani [1, *] and Hassan Karampour [2]

[1] *School of Civil Engineering, The University of Queensland, Australia 4072*
[2] *School of Engineering, Griffith University, Australia 4222*
**(Corresponding author: E-mail: f.albermani@uq.edu.au)*

ABSTRACT: Results from hyperbaric chamber tests of confined buckle propagation using 3m long aluminium pipes with three different D/t ratios are presented and discussed. A new testing method, confined ring squash test, is proposed to estimate the confined buckle propagation pressure. The proposed confined ring squash test gives a reasonable estimate of the confined buckle propagation pressure and is a much expedient test to implement in comparison to hyperbaric chamber test.

1.   INTRODUCTION

Buckle propagation is a snap through phenomenon where a local collapse once initiated may propagate rapidly along the structure with catastrophic consequences. The propagation pressure P_p is substantially lower than the pressure required for the initiation of local collapse, the initiation pressure P_I, [1]. The propagation pressure is a vital design criterion in many engineering applications such as deep subsea pipelines [2-6], heat exchangers and penstocks in hydroelectric power plants [7]. Figure 1 shows a typical propagation response obtained from testing aluminium pipes in a hyperbaric chamber [4]. The response is depicted in terms of the applied hydrostatic pressure vs the pipe's volume change. The propagation response is characterised by the initiation and propagation pressures (P_I and P_p) and by the dog-bone deformation that propagates along the pipe as shown in Figure 1. The elastic collapse pressure, P_c , represents an upper-bound on P_I and the pressure from a   ring collapse mechanism, P_{PM}, gives a lower-bound on P_p [2]. These two pressures, P_c and P_{PM}, are given by

$$P_c = \frac{2E}{\left(1-v^2\right)}\left(\frac{t}{D}\right)^3$$

(1)

$$P_{PM} = \pi\sigma_y \left(\frac{t}{D}\right)^2$$

(2)

where E, v, and σ_y are the elasticity modulus, Poisson's ratio and yield stress of the material, respectively, and D and t are the pipe's diameter and wall thickness.

Another form of buckle propagation is the confined buckle propagation which can be observed when a pipe is confined (without a mechanical connection) in a close-fit rigid medium and is subjected to hydrostatic pressure. Shell liners in wells and underground shafts and slip-on buckle

arrestor used in subsea pipelines are some examples where confined buckle propagation may take place [8, 9]. The confined buckle propagation response is characterised by the confined initiation and confined propagation pressures (P_{lc} and P_{pc} respectively) and by the U-shape (rather than a dog-bone) deformation that propagates along the confined pipe as shown in Figure 2.
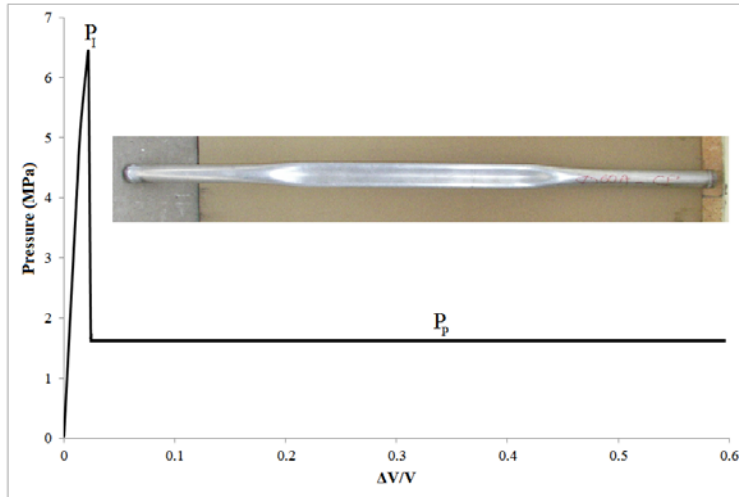
Figure 1. Buckle Propagation (Unconfined) with Dog-bone Deformation

Figure 2. Confined Buckle Propagation with the U-mode Shape of Deformation

In this work, experimental investigation is conducted using 3m long aluminium pipes with outer diameter of 76.2mm (length-to-diameter ratio, L/D=39.4) and three different diameter-to-thickness (D/t) ratios (16.2, 23.8 and 47.6) as shown in Table 1. Three tensile coupon tests were conducted for each D/t and the average obtained material properties are listed in Table 1.

Table 1. Material and Section Properties of the Test Specimens

D/t	Alloy	D (mm)	t (mm)	E (GPa)	E'/E (%)	σ_y (MPa)
16.2	6060-T591	76.2	4.7	69.0	0.65	76.7
23.8	6063-T4	76.2	3.2	69.0	0.68	75.7
47.6	6060-T5	76.2	1.6	69.0	0.4	212.7

A 2m long seamless steel pipe with inner diameter of 77.9mm and 5.5mm wall-thickness is used for confining the aluminium pipe as shown in Figure 3. This gives 0.85mm clearance around the aluminium pipe along the 2m long confined length with the remaining 1m length of the aluminium pipe is left unconfined. The flexural rigidity ratio of the confining steel pipe to the confined aluminium pipe ranges from around 5 to 118 (depending on D/t of the aluminium pipe and assuming the same Poisson's ratio for steel and aluminium).

Figure 3. Some of the 3m long Aluminium Pipes used in the Test,
One of them is shown with 2m Long confining steel pipe

2.   HYPERBARIC CHAMBER TEST OF CONFINED BUCKLE PROPAGATION

A 4m long stiff hyperbaric chamber with 173mm internal diameter is used in this test as shown in Figure 4. The chamber is rated for 20 MPa internal pressure [4]. A volume-controlled pressurization with a high pressure pump is used to obtain buckle propagation under quasi-static steady-state conditions. The 3m long aluminium pipe specimen is sealed by welding a thick cap at each end. The outer wall of the aluminium pipe is lubricated and the pipe is inserted inside the 2m long confining steel pipe. Two valves are connected at one end of the aluminium pipe through the stiff cap as shown in Figure 4. One valve is used for bleeding the aluminium pipe while filling it with water before testing commence. The second valve is used to vent the aluminium pipe specimen to the atmosphere through an umbilical connected through the chamber's wall. This second valve and umbilical are also used to collect water flow from the aluminium pipe specimen during buckle propagation. The amount of water flow from the aluminium pipe corresponds to volume change during buckle propagation. The aluminium pipe specimen with the confining steel pipe around it are inserted in the chamber then the aluminium pipe is filled with water and vented through the chamber wall. The chamber is sealed, filled with water then gradually pressurised.

Three control tests were conducted first (one for each D/t) to determine the propagation response of the aluminium pipes without the confining steel pipe. In these tests, 3m long intact (as is) aluminium pipe specimens were used. The experimental propagation response obtained from these control tests is shown in Figure 5 and the obtained P_I and P_p are listed in Table 2 together with the lower-bound P_{PM} from Eq. 2. Figure 5 shows a typical propagation response with steady increase in pressure as the chamber is gradually pressurized until the initiation pressure P_I is reached when a section along the aluminium pipe specimen collapses leading to a significant drop in chamber's pressure and steady flow of water from within the vented pipe specimen. By maintaining a slow rate of pressurizing, the chamber's pressure is stabilized at the propagation pressure, P_P, with the

dog-bone buckle longitudinally propagating along the pipe accompanied by steady flow of water from within the vented pipe specimen. Figure 6a shows the three pipes at the end of the test, the extent of the dog-bone buckle propagation is clearly seen in this Figure.
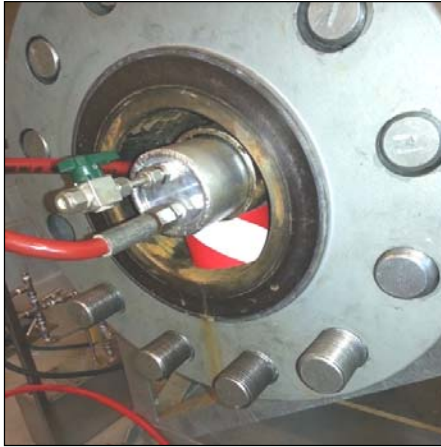
Figure 4. The Hyperbaric Chamber used in the Test
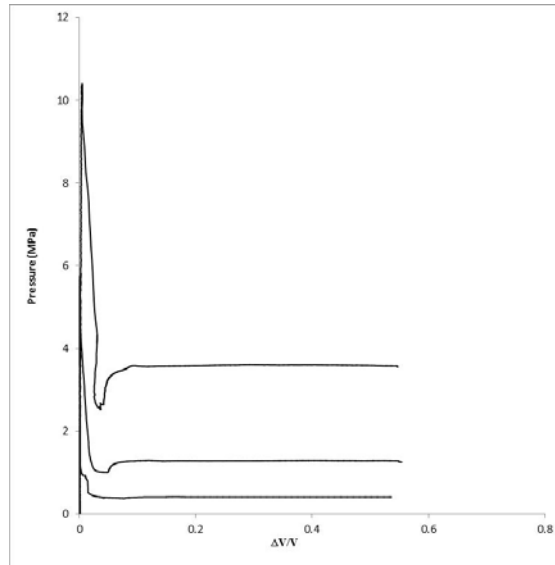
Figure 5. Buckle Propagation Response (Unconfined) from Control Tests

Table 2. Buckle Propagation (Unconfined) Test Results

D/t	Buckle propagation (unconfined) (MPa)			
	P_I	P_p	P_{PM} (eq 2)	P_{PM}/P_p
16.2	10.4	3.6	0.92	0.26
23.8	5.8	1.3	0.42	0.32
47.6	1.5	0.4	0.29	0.72

(a)
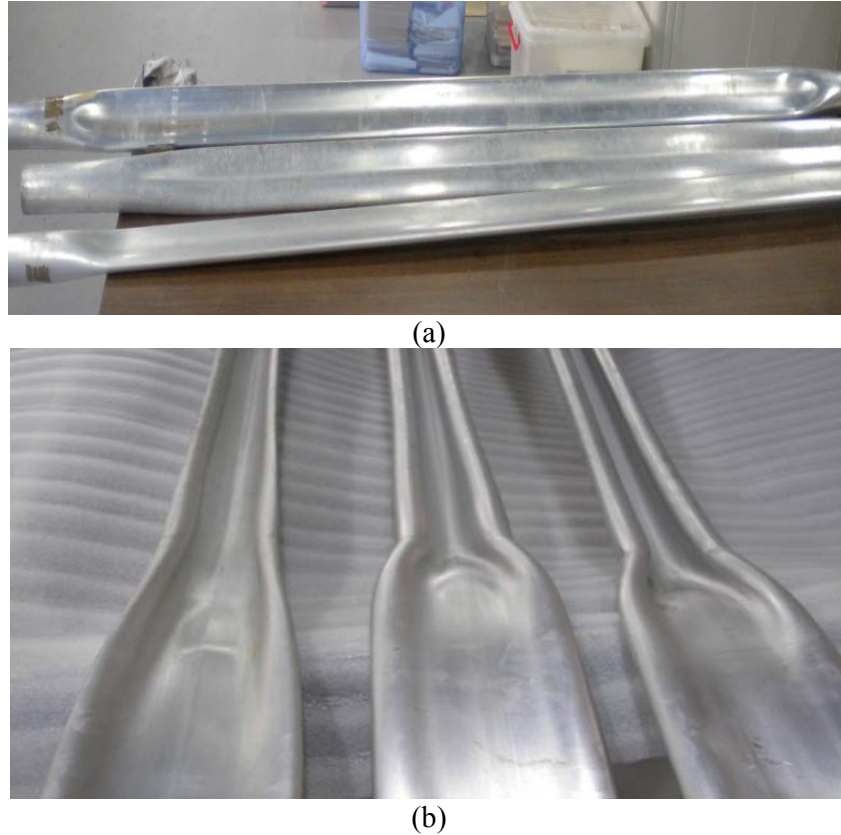
(b)
Figure 6. Deformed Specimens after Buckle Propagation; a) Unconfined, b) Confined

Similar test protocol as described above is followed for the confined buckle propagation. The 3m long aluminium pipe specimen was lubricated and inserted inside the 2m long confining steel pipe prior to inserting in the hyperbaric chamber. In order to insure that buckle propagation initiates at the unconfined region of the aluminium pipe, a small dent is imposed mid-way at the unconfined 1m long section of the aluminium pipe specimen. The ovalization caused by the dent is expressed as an ovalization ratio Ω and maintained at around 7% for all the test specimens. The ovalization ratio is taken as:

$$\Omega = \frac{D_{max} - D_{min}}{D_{max} + D_{min}} \tag{3}$$

where D_{max} and D_{min} are the maximum and minimum measured outer diameter of the dented aluminium pipe.

Eight confined tests were conducted in the hyperbaric chamber, these consist of three tests for each of D/t=47.6 and 23.8 and two tests for D/t=16.2. However, two tests for D/t=47.6 sprung a leak at the weld of the stiff end cap as the buckle start penetrating the confined section. For this reason these two tests were disregarded.

The experimental confined propagation response from the remaining six tests is shown in Figure 7 and the average obtained characteristic pressures (P_I, P_p, P_{Ic} and P_{pc}) are listed in Table 3.   In these tests, the buckle is initiated first (P_I) at the unconfined region of the aluminium pipe where the dent is imposed. The dog-bone deformation propagates at P_p along the unconfined length until it approaches the confined region. A noticeable build-up of pressure inside the chamber is observed. When the pressure inside the chamber reaches the confined initiation pressure P_{Ic}, the buckle

transforms from a dog-bone to a U-shape and penetrates through the confined region. The U-shaped buckle propagates along the confined aluminium pipe at the confined propagation pressure P_{pc}. The transition of the buckle from a dog-bone to a U-shape can be seen in Figure 6b. Due to the acute imperfection sensitivity of buckle initiation (in contrast to buckle propagation [2-4]), the P_I shown in Table 3 for the dented specimens is less than that shown in Table 2 for the intact pipes. In order to align the curves for different D/t ratios shown in Figure 7, the change in volume ΔV (X-axis) is normalised by the change in the specimen's volume, $\tilde{V}$, at P_{Ic}.
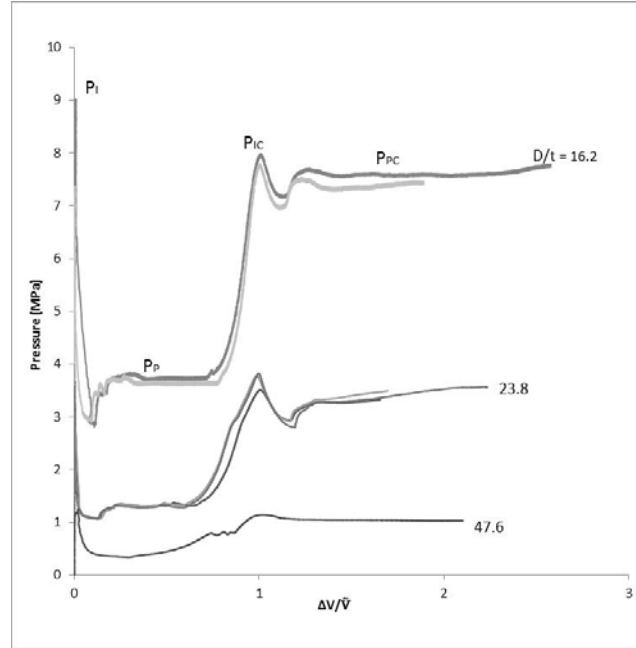
Figure 7. Confined Buckle Propagation Test Results

3   RING COLLAPSE MECHANISM

Assuming elastic perfectly plastic material, a ring collapse mechanism with two plastic hinges and reverse curvature of a semi-circular profile can be used to approximate the U-shaped confined propagation buckle pressure [8]. Accordingly, the confined propagation pressure from the ring collapse mechanism, P_{pcM}, is given by

$$P_{pcM} = 4\,\sigma_y \left(\frac{t}{D}\right)^2 = \frac{4}{\pi} P_{PM} \tag{4}$$

The results from eq 4 for the three D/t ratios used in the hyperbaric chamber tests are listed in Table 2, these results grossly underestimate P_{pc}.

The experimental results from the hyperbaric chamber tests for unconfined P_p and confined P_{pc} propagation pressures (Table 3) can be represented by a power law relationship [9]

$$\frac{P}{\sigma_y} = A \left(\frac{t}{D}\right)^{\beta} \tag{5}$$

Where P above corresponds to either P_p or P_{pc}. The values of A and β, respectively, from best fits of

the hyperbaric chamber results are 124.98 and 2.815 for unconfined P_p and 203.23 and 2.703 for confined P_{pc}.

The experimental propagation pressure (unconfined and confined, Tables 2 and 3) together with the results from Eqs. 2, 4 and 5 are shown in Figure 8. It is clear from this Figure that Eqs. 2 and 4 provide lower-bound estimate for the unconfined and confined propagation pressures, respectively. Due to the larger energy required for deformation in the confined U-shaped buckle in comparison to the unconfined dog-bone shape, P_{pc} is significantly higher than P_p, particularly at higher D/t range, as can be seen in Figure 8 and Table 3.
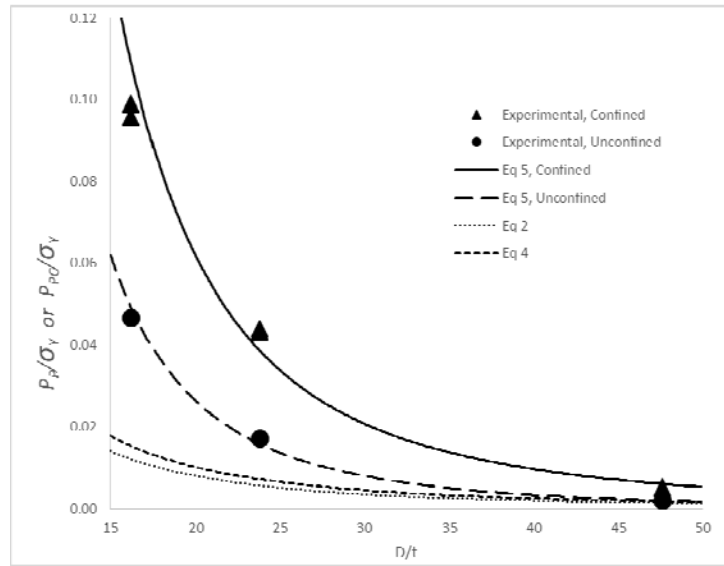
Figure 8. Summary of Experimental, Power-law Relation and Analytical Results of Buckle Propagation Pressure (Unconfined and Confined)

Table 3. Confined Buckle Propagation Test Results

D/t	Confined Buckle Propagation (MPa)						P_{Ic}/P_I	P_{pc}/P_p	P_{pcM}/P_{pc}	P_{pcR}/P_{pc}
	P_I	P_p	P_{Ic}	P_{pc}	P_{pcM} (eq 4)	P_{pcR}				
16.2	8.2	3.6	7.9	7.5	1.17	7.09	0.96	2.08	0.16	0.95
23.8	3.8	1.3	3.7	3.3	0.53	2.37	0.97	2.54	0.16	0.72
47.6	1.3	0.4	1.2	1.1	0.38	0.71	0.92	2.75	0.35	0.65

4   CONFINED RING SQUASH TEST (CRST)

The ring squash test (RST, Figure 9) has been shown to be a simple and expedient test to conduct that gives a lower bound estimate of unconfined propagation pressure [2, 4, 10]. In this test a short segment of the pipe with a length around *2-3D* is diametrically compressed between two semi-cylindrical rigid indenters of the same diameter and length as the pipe being tested. From the RST, and using equilibrium considerations and energy balance approach, a good estimate of propagation pressure P_p can be calculated as described by Albermani et al [2].

Figure 9. Ring Squash test (RST)

In this work, the RST has been modified to determine the confined propagation pressure, P_{pc}, as shown in Figure 10. A *2D* long segment of the aluminium pipe is positioned inside a semi-cylindrical solid confinement of the same diameter, *D,* as the pipe specimen and diametrically compressed by a solid semi-cylindrical indenter with a diameter of (*D-4t*). The length of each of the semi-cylindrical solid confinement and indenter is the same as the pipe specimen (*2D*).
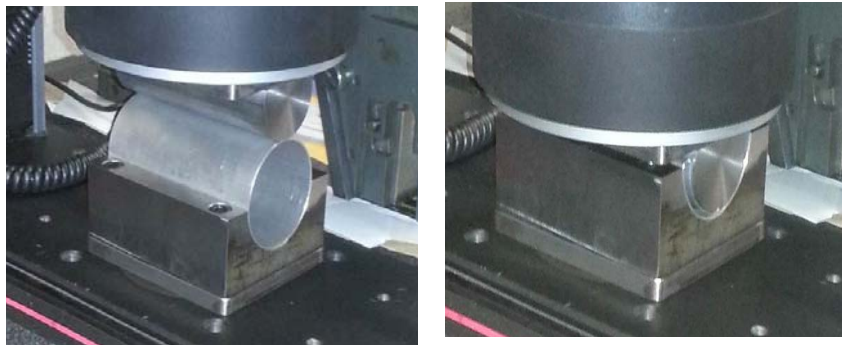
Figure 10. Confined Ring Squash Test (CRST)

Three CRST were conducted for each of the *D/t* ratios given in Table 1 (a total of nine tests). The experimental load-displacement response from these tests is shown in Figure 11. The sharp rise in the response seen for *D/t* 23.8 and 47.6 at displacement around 70mm is due to touchdown at the end of the test. In contrast, the drop in the response just before the end of the test seen for *D/t* 16.2 is due to fracture of the pipe wall at one of the fold lines of the U-shape. Figure 12 shows the nine test samples after the CRST.

By using an energy balance approach [2], an estimate of the confined propagation pressure from CRST, P_{pcR}, can be obtained. This is done by calculating the area, Λ, under the experimental load-displacement curve (Figure 11) and the change in the specimen's cross-section area, ΔA, during the CRST (from circular to U-shape)

$$P_{pcR} = \frac{\Lambda}{(\Delta A)\lambda} \tag{6}$$

where λ is the length of the test specimen ($\lambda=2D$ in the current tests).
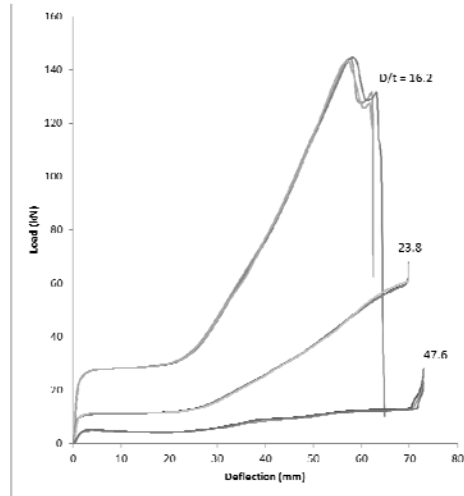
Figure 11. CRST Test Results

The average P_{pcR} obtained from the CRST is listed in Table 3 (average of three tests per D/t). It is clear that the CRST provides a much better estimate of the confined propagation pressure than the ring collapse mechanism (Eq. 4).

Figure 12. Test Samples (D/t: 16.2, 23.8 and 47.6) after the CRST

5   DISCUSSION

Hyperbaric chamber test results of confined propagation buckling show that the propagation buckle transforms from dog-bone to U-shape and penetrates through the confinement as seen in Figure 6b. The obtained confined initiation pressure, P_{Ic}, is 92-97% of the unconfined initiation pressure, P_I, depending on D/t ratio (Table 3). On the other hand, the confined propagation pressure, P_{pc}, is more than two times P_p. This indicates that, for the combination of D/t aluminium pipes with steel confinement used in these tests, once a buckle is initiated at P_I away from confinement, it will propagates through the confinement since P_{Ic}/P_I is less than one, regardless of P_{pc}/P_p.

As can be seen in Figures 2 and 6b, the pathological deformation experienced by the pipe as the confined U-shape buckle propagates, highlights the complex loading and mechanisms involved in confined propagation. The length, l_I, of the transition zone from dog-bone to U-shape buckle (Figure 6b) was measured for all the specimens used in the hyperbaric chamber tests. This length increases nearly linearly with D/t as can be seen in Figure 13 with l_I/D range from *0.5-1*.

Another transition zone at the U-shaped wave front was also measured (Figure 2). The length of this transition zone, l_2, is taken as the distance between the crest of the collapse to the point of first contact of the opposite walls [9]. This length also increases nearly linearly with D/t as can be seen in Figure 13 with l_2/D range from 2.4-3.9.   This indicates that l_2 for confined propagation buckling is shorter than that for unconfined buckling where l_2/D is expected to be in the range of 5-11 and vary nonlinearly with D/t [3, 4, 10]. The shorter l_2 indicates that higher longitudinal stretching is involved in confined buckle propagation than in the unconfined one.

The range of P_{pc}/P_p ratio given in Table 3 is 2.08-2.75, with higher ratio at higher D/t. A similar trend was observed in a previous data set using stainless steel tubes [9]. The higher longitudinal stretching expected in confined propagation could be the reason for this trend since the contribution of energy dissipation by stretching in comparison to circumferential bending increases at higher D/t.

Unlike the ring collapse mechanism (Eq. 4), the proposed confined ring squash test, CRST, gives reasonable estimate (65-95%, Table 3) of the confined propagation pressure. The CRST is a simple and expedient test to conduct in comparison to the more demanding hyperbaric chamber test.
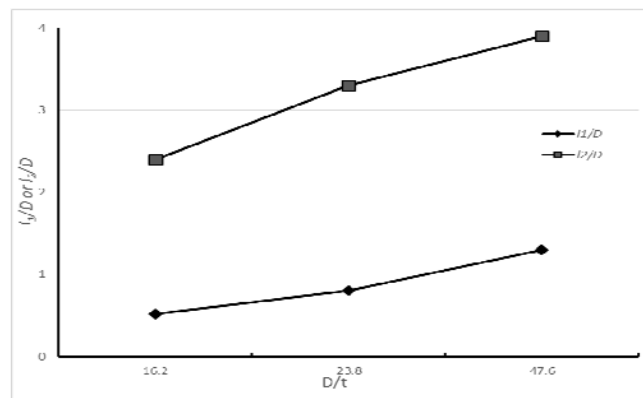
Figure 13. Transition Zone Length, *l1* and *l2*, for Different *D/t*

ACKNOWLEDGMENT

REFERENCES

[1]   Kyriakides, S, "Propagation Instabilities in Structures", Advances in Applied Mechanics, 1994, Vol. 30, pp. 67-189.
[2]   Albermani, F., Khalilpasha, H. and Karampour, H., "Propagation Buckling in Deep Sub-sea Pipelines", Engineering Structures, 2011, Vol. 33, No. 9, pp. 2547-53.
[3]   Khalilpasha, H. and Albermani, F., "Textured Deep Subsea Pipelines", International Journal of Mechanical Sciences, 2013, Vol. 68, pp. 224-235.
[4]   Khalilpasha, H. and Albermani, F., "Hyperbaric Chamber Test of Subsea Pipelines. Thin-Walled Structures, 2013, Vol. 71, pp. 1-6.
[5]   Karampour, H. and Albermani, F., "Buckle Interaction in Deep Subsea Pipelines", Thin-Walled Structures, 2013, Vol. 72, pp. 113-120.

[6]   Karampour, H. and Albermani, F., "Experimental and Numerical Investigations of Buckle Interaction in Subsea Pipelines", Engineering Structures, 2014, Vol. 66, pp. 81-88.

[7]   Zaras, J., "Analysis of an Industrial Piping Installation under Buckling Propagation", Thin-Walled Structures, 2008, Vol. 46, pp. 855-59.

[8]   Tam, C.K.W. and Croll, J.G.A., "An Improvement of the Propagation Buckle Performance of Subsea Pipelines", Thin-Walled Structures, 1986, Vol. 4, pp. 423-48.

[9]   Kyriakides, S. and Lee, L.H., "Buckle Propagation in Confined Steel Tubes", International Journal of Mechanical Sciences, 2005, Vol. 47, pp. 603-20.

[10]   Kamalarasa, S. and Calladine, C.R., "Buckle Propagation in Submarine Pipelines", International Journal of Mechanical Sciences, 1988, Vol. 30, No. 3/4, pp. 217-28.

A NUMERICAL METHOD FOR FREE VIBRATION OF AXIALLY LOADED COMPOSITE TIMOSHENKO BEAM

Aleksandar Prokić * , Miroslav T. Bešević and Martina Vojnić-Purčar

Faculty of Civil Engineering, University of Novi Sad, Kozaračka 2a, 24000 Subotica, Serbia
*(Corresponding author: E-mail: aprokic@eunet.rs)

ABSTRACT: In this paper, a numerical method is employed to study the free vibration of axially loaded composite Timoshenko beam. The problem is governed by a set of coupled second-order ordinary differential equations of motion, under different boundary conditions. The method is based on numerical integration rather than the numerical differentiation since the highest derivatives of governing functions are chosen as the basic unknown quantities. The kernels of integral equations turn out to be Green's function of corresponding equation with homogeneous boundary conditions. The accuracy of the proposed method is demonstrated by comparing the calculated results with those available in the literature. It is shown that good accuracy can be obtained even with a relatively small number of nodes.

1.   INTRODUCTION

Composite thin-walled beams are widely used as structural elements in many types of structures. Compared to standard construction materials, composite materials present many advantages, e.g. light weight, corrosion resistance, low thermal expansion, and excellent fatigue characteristics in the direction of the fibers. Because of their practical importance the accurate prediction of the dynamic behavior of such constructions is an important part of engineering analysis.

When cross-sectional dimensions are large or higher frequencies are studied in the vibration analysis of the composite beams, the effects of shear deformation and rotary inertia should be taken into account, i.e. Timoshenko's beam model should be used. The effect of axial load adds some additional terms to the equations of motion of the Timoshenko beam and so they become more complicated to solve and numerical methods have to be applied. Numerical methods such as finite element (Reddy [17], Vo et al. [18], Borbon et al. [6]) finite difference (Fule and Zhi-zhong [8], Ansari et al. [1]) differential quadrature (Mirtalaie et al. [13], Rajasekeran [16]), the dynamic stiffness matrix (Benerjee [2 3], Li et al. [11], Pagani et al. [14]) and some other methods (Biscontin et al. [5], Berczynski and Wroblewski [4], Pan et al. [15], Liu et al. [12]) have been used in solving free vibration problems of structures.

In this study a numerical method is developed for free vibration analysis of an axially loaded composite Timoshenko beam with bending-torsional coupling. The highest derivatives in the differential equations are chosen as the basic unknowns of the problem, as it was first proposed by Hajdin [9], and the unknowns are determined through the corresponding integral equations. In the formation of integral equations we use methods that are well known to engineers from the theory of structures, as Green's functions are nothing more than well-known influence function of a beam. Finally, by the application of the numerical integration it is possible to replace that equations into linear algebraic equations from which can be obtained a characteristic equation of natural

frequencies, for different boundary conditions. With a relatively small number of points it can be achieved satisfactory accuracy of the results.

2.   THEORETICAL CONSIDERATIONS

A straight Timoshenko beam of length l with a solid rectangular cross-section is considered. A constant axial load P is assumed to act through the centroid (mass centre) of the cross section. P is considered to be positive when it is compressive. The flexural displacement, in the y direction and the torsional rotation about the z-axis are denoted by $v(z,t)$ and $\varphi(z,t)$ respectively, where z and t denote distance from the origin and time. The rotation of the cross-section about the y-axis due to flexure alone is denoted by $\psi(z,t)$.

The governing partial differential equations of motion of the axially loaded Timoshenko beam exhibiting coupled flexure–torsion free natural vibration are given by Kaya and Ozgumus [10]

$$EI_y\psi'' + kFG(v' - \psi) + K\varphi'' - \rho I_y\ddot{\psi} = 0$$
$$kFG(v'' - \psi') - m\ddot{v} - Pv'' = 0 \tag{1}$$
$$K\psi'' - P\left(\frac{I_s}{m}\right)\varphi'' + GJ\varphi'' - I_s\ddot{\varphi} = 0$$

where primes and dots denote differentiation with respect to coordinate z and time t, respectively; ρ is the material density; F the cross sectional area; I_y the second moment of inertia of the beam cross section about the y-axis; $m = \rho F$ is the mass per unit length; I_s the polar mass moment of inertia per unit length about the z-axis. EI_y, GJ, K and kGF are the flexural rigidity, torsional rigidity, flexure–torsion coupling rigidity and shear rigidity of the composite beam, respectively. Eqs. 1 together with appropriate end conditions (z = 0 and z = l) completely define the coupled bending–torsion free vibration of an axially loaded uniform Timoshenko beam.

If a sinusoidal variation of $v(z,t), \psi(z,t)$ and $\varphi(z,t)$ with circular frequency ω, is assumed, then

$$v(z,t) = V(z)\sin\omega t$$
$$\psi(z,t) = \Psi(z)\sin\omega t \tag{2}$$
$$\varphi(z,t) = \Phi(z)\sin\omega t$$

where $V(z), \Psi(z)$ and $\Phi(z)$ are the amplitudes of the sinusoidal varying vertical displacement, flexural rotation and torsion rotation, respectively.

Substituting Eqs. 2 into Eqs. 1, equations of motion can be rewritten as follows:

$$EI_y\Psi'' + kFG(V' - \Psi) + K\Phi'' + \rho I_y\omega^2\Psi = 0$$
$$kFG(V'' - \Psi') + m\omega^2 V - PV'' = 0 \tag{3}$$
$$K\Psi'' - P\left(\frac{I_s}{m}\right)\Phi'' + GJ\Phi'' + I_s\omega^2\Phi = 0$$

or in the matrix form

$$\mathbf{A}q'' + \mathbf{B}q' + \left(\mathbf{C} + \omega^2\mathbf{D}\right)q = 0 \tag{4}$$

where displacement state vector **q,** consisting of 3 displacement parameters, is defined by

$$\mathbf{q} = \begin{bmatrix} q_1 \\ q_2 \\ q_3 \end{bmatrix} = \begin{bmatrix} V(z) \\ \Psi(z) \\ \Phi(z) \end{bmatrix} \tag{5a}$$

and matrices **A**, **B**, **C** and **D** are as follows

$$\mathbf{A} = \begin{bmatrix} & EI_y & K \\ kGF - P & & \\ & K & GJ - P\left(\dfrac{I_s}{m}\right) \end{bmatrix} \quad \mathbf{B} = \begin{bmatrix} kFG & & \\ & -kFG & \\ & & \end{bmatrix} \quad \mathbf{C} = \begin{bmatrix} -kFG & & \\ & & \\ & & \end{bmatrix} \tag{5b}$$

$$\mathbf{D} = \begin{bmatrix} & \rho I_y & \\ m & & \\ & & I_s \end{bmatrix}$$

3.   INTEGRAL EQUATION METHOD

The second derivatives of any component q_i $(i = 1, 2$ and $3)$ of vector **q** shall be denoted

$$q_i'' = -p_i(z) \tag{6}$$

In addition to differential Eq. 6 the following boundary conditions are given

$$for\ z = 0 \quad \begin{cases} q_i = q_{i0} \\ q_i' = q_{i0}' \end{cases} \tag{7}$$

The solution to Eq. 6 may be written as (Byron and Fuller [7])

$$q_i(z) = \int s(z,\varsigma) p_i(\varsigma) d\varsigma + q_{i0}' z + q_{i0} \tag{8}$$

where ς is the integration variable and $s(s,\varsigma)$ is Green's function corresponding to the differential Eq. 6, which obeys homogeneous boundary conditions Eq. 7. Function $s(s,\varsigma)$, known as kernel of integral Eq. 8, is defined by

$$s(z,\varsigma) = \begin{cases} -(z-\varsigma) & \varsigma \le z \\ 0 & \varsigma > z \end{cases} \tag{9}$$

If $p_i(z)$ is understood as external transverse load distributed along the axis of the beam, q_{i0} and q_{i0}' as a bending moment and a transversal force, respectively, at the left end of the beam, and $q_i(z)$ as bending moment along the beam, than integral Eq. 8 defines the dependence between the cross section forces and external load of the fictitious cantilever beam of length l, fixed at the right end,

Figure 1. From this it follows that Green's function is the influence function for the bending moment of a cantilever beam, well known to civil engineering.
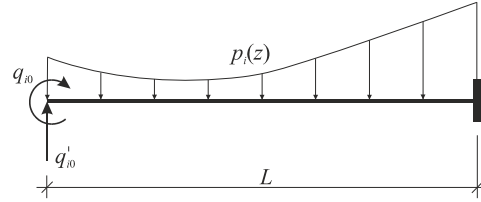
Figure 1. Fictitious Cantilever Beam

Differentiating Eq. 8 we get

$$q_i'(z) = \int s'(z,\varsigma) p_i(\varsigma) d\varsigma + q_{i0}' \tag{10}$$

where is

$$s'(z,\varsigma) = \begin{cases} -1 & \varsigma \leq z \\ 0 & \varsigma > z \end{cases} \tag{11}$$

influence function for transversal force of the cantilever beam.

4.   NUMERICAL SOLUTION

The values of definite integral in Eq. 8 can be expressed approximately, using method for numerical integration.

Unknown function $p_i(z)$, which by static analogy with beam in bending represents the load, will be replaced with an equivalent static forces $P_{i,k}$ concentrated at selected points (nodes) k ($k = 0$, 1, 2,.., M-1) of the equidistant spacing λ, so that the bending moments at these points, due to a given distributed load, are the same as the moments due to concentrated forces, Figure 2. In the case when the given load changes linearly from node to node, expressions for the concentrated forces are given by the following expressions

$$P_{i,0} = \frac{\lambda}{6}\left(2p_{i,0} + p_{i,1}\right)$$
$$P_{i,k} = \frac{\lambda}{6}\left(p_{i,k-1} + 4p_{i,k} + p_{i,k+1}\right) \tag{12}$$
$$P_{i,M} = \frac{\lambda}{6}\left(p_{i,M-1} + 2p_{i,M}\right)$$

where $p_{i,k}$ are the ordinates of function $p_i(z)$ at selected points k. Expressions Eq. 12 are well known in structural mechanics where a process of reducing a distributed load to equivalent concentrated forces is often employed.
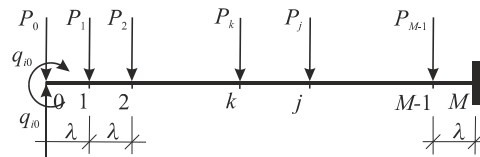
Figure 2. Substituting Concentrated Forces

Eq. 8, taking into account their static sense, can be now represented in matrix form as

$$
\begin{bmatrix} \mathbf{q}_1 \\ \mathbf{q}_2 \\ \mathbf{q}_3 \\ \vdots \\ \mathbf{q}_M \end{bmatrix} = \begin{bmatrix} \lambda\mathbf{I} & & & \cdots & \\ 2\lambda\mathbf{I} & \lambda\mathbf{I} & & \cdots & \\ 3\lambda\mathbf{I} & 2\lambda\mathbf{I} & \lambda\mathbf{I} & \cdots & \\ \vdots & \vdots & \vdots & \ddots & \vdots \\ M\lambda\mathbf{I} & (M-1)\lambda\mathbf{I} & (M-2)\lambda\mathbf{I} & \cdots & \lambda\mathbf{I} \end{bmatrix} \begin{bmatrix} \mathbf{P}_0 \\ \mathbf{P}_1 \\ \mathbf{P}_2 \\ \vdots \\ \mathbf{P}_{(M-1)} \end{bmatrix} + \begin{bmatrix} \lambda\mathbf{I} & \mathbf{I} \\ 2\lambda\mathbf{I} & \mathbf{I} \\ 3\lambda\mathbf{I} & \mathbf{I} \\ \vdots & \vdots \\ M\lambda\mathbf{I} & \mathbf{I} \end{bmatrix} \begin{bmatrix} \mathbf{q}_0' \\ \mathbf{q}_0 \end{bmatrix}
\tag{13}
$$

where $\mathbf{q}_j$ ($j = 1, 2,\ldots, M$) and $\mathbf{P}_k$ ($k = 0, 2,\ldots, M\text{-}1$) are the vectors of nodal "bending moments" and "concentrated forces" of the fictitious cantilever beam, all of which, in general, has three components.

Substituting Eqs. 12 to Eq. 13 we obtain

$$\mathbf{Q} = \mathbf{SP} + \mathbf{LQ}_0 \tag{14}$$

or explicitly

$$
\underbrace{\begin{bmatrix} \mathbf{q}_1 \\ \mathbf{q}_2 \\ \mathbf{q}_3 \\ \vdots \\ \mathbf{q}_j \\ \vdots \\ \mathbf{q}_M \end{bmatrix}}_{\mathbf{Q}} = \underbrace{\begin{bmatrix} (S_{11}+\bar{S}_{11})\mathbf{I} & \bar{S}_{12}\mathbf{I} & & \cdots & & \cdots & \\ (S_{21}+\bar{S}_{21})\mathbf{I} & (S_{22}+\bar{S}_{22})\mathbf{I} & & \cdots & & \cdots & \\ (S_{31}+\bar{S}_{31})\mathbf{I} & (S_{32}+\bar{S}_{32})\mathbf{I} & S_{33}\mathbf{I} & \cdots & & \cdots & \\ \vdots & \vdots & \vdots & \ddots & \vdots & \ddots & \vdots \\ (S_{j1}+\bar{S}_{j1})\mathbf{I} & (S_{j2}+\bar{S}_{j2})\mathbf{I} & S_{j3}\mathbf{I} & \cdots & S_{jj}\mathbf{I} & \cdots & \\ \vdots & \vdots & \vdots & \ddots & \vdots & \ddots & \vdots \\ (S_{M1}+\bar{S}_{M1})\mathbf{I} & (S_{M2}+\bar{S}_{M2})\mathbf{I} & S_{M3}\mathbf{I} & \cdots & S_{Mj}\mathbf{I} & \cdots & S_{MM}\mathbf{I} \end{bmatrix}}_{\mathbf{S}} \underbrace{\begin{bmatrix} \mathbf{p}_1 \\ \mathbf{p}_2 \\ \mathbf{p}_3 \\ \vdots \\ \mathbf{p}_j \\ \vdots \\ \mathbf{p}_M \end{bmatrix}}_{\mathbf{P}} + \underbrace{\begin{bmatrix} \lambda\mathbf{I} & \mathbf{I} \\ 2\lambda\mathbf{I} & \mathbf{I} \\ 3\lambda\mathbf{I} & \mathbf{I} \\ \vdots & \vdots \\ j\lambda\mathbf{I} & \mathbf{I} \\ \vdots & \vdots \\ M\lambda\mathbf{I} & \mathbf{I} \end{bmatrix}}_{\mathbf{L}} \underbrace{\begin{bmatrix} \mathbf{q}_0' \\ \mathbf{q}_0 \end{bmatrix}}_{\mathbf{Q}_0}
\tag{15}
$$

where

$$
S_{jk} = \begin{cases} -\lambda^2/6 & j = k \\ 0 & j < k \\ -(j-k)\lambda^2 & j > k \end{cases}
$$

$$
\bar{S}_{jk} = \begin{cases} -\left(j-\dfrac{1}{3}\right)\lambda^2 & k = 1 \\ \dfrac{1}{2}\left(j-\dfrac{1}{3}\right)\lambda^2 & k = 2 \end{cases}
\tag{16}
$$

Performing the Eq. 14 the ordinate of function $p_i(z)$ at point $k = 0$ (p_{i0}) is determined by linear extrapolation, so that $p_{i0} = 2p_{i1} - p_{i2}$.

Differentiating Eq. 14 with respect to z, and applying the previous transformations, in a similar way we obtain

$$\mathbf{Q}' = \mathbf{S}'\mathbf{P} + \mathbf{L}'\mathbf{Q}_0 \tag{17}$$

or in a developed form

$$
\underbrace{\begin{bmatrix} \mathbf{q}'_1 \\ \mathbf{q}'_2 \\ \mathbf{q}'_3 \\ \vdots \\ \mathbf{q}'_j \\ \vdots \\ \mathbf{q}'_M \end{bmatrix}}_{\mathbf{Q}'} = \underbrace{\begin{bmatrix} (S'_{11}+\bar{S}'_{11})\mathbf{I} & \bar{S}'_{12}\mathbf{I} & & \cdots & & \cdots & \\ (S'_{21}+\bar{S}'_{21})\mathbf{I} & (S'_{22}+\bar{S}'_{22})\mathbf{I} & & \cdots & & \cdots & \\ (S'_{31}+\bar{S}'_{31})\mathbf{I} & (S'_{32}+\bar{S}'_{32})\mathbf{I} & S'_{33}\mathbf{I} & \cdots & & \cdots & \\ \vdots & \vdots & \vdots & \ddots & \vdots & \ddots & \vdots \\ (S'_{j1}+\bar{S}'_{j1})\mathbf{I} & (S'_{j2}+\bar{S}'_{j2})\mathbf{I} & S'_{j3}\mathbf{I} & \cdots & S'_{jj}\mathbf{I} & \cdots & \\ \vdots & \vdots & \vdots & \ddots & \vdots & \ddots & \vdots \\ (S'_{M1}+\bar{S}'_{M1})\mathbf{I} & (S'_{M2}+\bar{S}'_{M2})\mathbf{I} & S'_{M3}\mathbf{I} & \cdots & S'_{Mj}\mathbf{I} & \cdots & S'_{MM}\mathbf{I} \end{bmatrix}}_{\mathbf{S}'} \underbrace{\begin{bmatrix} \mathbf{p}_1 \\ \mathbf{p}_2 \\ \mathbf{p}_3 \\ \vdots \\ \mathbf{p}_j \\ \vdots \\ \mathbf{p}_M \end{bmatrix}}_{\mathbf{P}} + \underbrace{\begin{bmatrix} \mathbf{I} & \\ \mathbf{I} & \\ \mathbf{I} & \\ \vdots & \vdots \\ \mathbf{I} & \\ \vdots & \vdots \\ \mathbf{I} & \end{bmatrix}}_{\mathbf{L}'} \begin{bmatrix} \mathbf{q}'_0 \\ \mathbf{q}_0 \\ \mathbf{Q}_0 \end{bmatrix} \tag{18}
$$

where

$$
S'_{jk} = \begin{cases} -\lambda/2 & j=k \\ 0 & j<k \\ -\lambda & j>k \end{cases}
$$

$$
\bar{S}'_{jk} = \begin{cases} -\lambda & k=1 \\ \lambda/2 & k=2 \end{cases}
\tag{19}
$$

Also, from Eq. 6 it follows

$$
\mathbf{Q}'' = -\mathbf{P} \tag{20}
$$

Conditions that differential equations of motion of the axially loaded Timoshenko beam, Eqs. 4, are satisfied at all discrete points j ($j=1, 2,..., M$), can be expressed as

$$
\mathbf{A}^*\mathbf{Q}'' + \mathbf{B}^*\mathbf{Q}' + \left(\mathbf{C}^* + \omega^2\mathbf{D}^*\right)\mathbf{Q} = \mathbf{0} \tag{21}
$$

where

$$
\mathbf{A}^*\left(\mathbf{B}^*,\mathbf{C}^*,\mathbf{D}^*\right) = \begin{bmatrix} \overset{1}{\mathbf{A}(\mathbf{B},\mathbf{C},\mathbf{D})} & \overset{2}{} & \overset{\cdots}{} & \overset{M}{} \\ & \mathbf{A}(\mathbf{B},\mathbf{C},\mathbf{D}) & & \\ & & \ddots & \\ & & & \mathbf{A}(\mathbf{B},\mathbf{C},\mathbf{D}) \end{bmatrix} \begin{matrix} 1 \\ 2 \\ \vdots \\ M \end{matrix} \tag{22}
$$

Substituting Eqs. 14, 17 and 20 into Eq. 21 yields

$$
\left[-\mathbf{A}^* + \mathbf{B}^*\mathbf{S}' + \left(\mathbf{C}^* + \omega^2\mathbf{D}^*\right)\mathbf{S}\right]\mathbf{P} + \left[\mathbf{B}^*\mathbf{L}' + \left(\mathbf{C}^* + \omega^2\mathbf{D}^*\right)\mathbf{L}\right]\mathbf{Q}_0 = \mathbf{0} \tag{23}
$$

from which we obtain

$$
\mathbf{P} = -\mathbf{K}^{-1}\bar{\mathbf{L}}\mathbf{Q}_0 \tag{24}
$$

where

$$\mathbf{K} = -\mathbf{A}^* + \mathbf{B}^*\mathbf{S}' + \left(\mathbf{C}^* + \omega^2\mathbf{D}^*\right)\mathbf{S}$$
$$\bar{\mathbf{L}} = \mathbf{B}^*\mathbf{L}' + \left(\mathbf{C}^* + \omega^2\mathbf{D}^*\right)\mathbf{L}$$

(25)

Taking into account Eqs. 15 and 18 we can establish a connection between the values of the vector **q** and **q'** on the right and left end of the element

$$\underbrace{\begin{bmatrix} \mathbf{q}'_M \\ \hline \mathbf{q}_M \end{bmatrix}}_{\mathbf{Q}_M} = \underbrace{\begin{bmatrix} S'_{M1}\mathbf{I} + \bar{S}'_{M1}\mathbf{I} & S'_{M2}\mathbf{I} + \bar{S}'_{M2}\mathbf{I} & S'_{M3}\mathbf{I} & \cdots & S'_{Mj}\mathbf{I} & \cdots & S'_{MM}\mathbf{I} \\ \hline S_{M1}\mathbf{I} + \bar{S}_{M1}\mathbf{I} & S_{M2}\mathbf{I} + \bar{S}_{M2}\mathbf{I} & S_{M3}\mathbf{I} & \cdots & S_{Mj}\mathbf{I} & \cdots & S_{MM}\mathbf{I} \end{bmatrix}}_{\mathbf{S}_M} \underbrace{\begin{bmatrix} \mathbf{p}_1 \\ \hline \mathbf{p}_2 \\ \hline \mathbf{p}_3 \\ \hline \vdots \\ \hline \mathbf{p}_j \\ \hline \vdots \\ \hline \mathbf{p}_M \end{bmatrix}}_{\mathbf{P}} + \underbrace{\begin{bmatrix} \mathbf{I} & \mathbf{0} \\ \hline l\mathbf{I} & \mathbf{I} \end{bmatrix}}_{\mathbf{T}} \underbrace{\begin{bmatrix} \mathbf{q}'_0 \\ \hline \mathbf{q}_0 \end{bmatrix}}_{\mathbf{Q}_0}$$

(26)

or

$$\mathbf{Q}_M = \mathbf{S}_M\mathbf{P} + \mathbf{T}\mathbf{Q}_0$$

(27)

Substituting Eq. 24 into Eq. 27 we get

$$\mathbf{Q}_M = \left(-\mathbf{S}_M\mathbf{K}^{-1}\bar{\mathbf{L}} + \mathbf{T}\right)\mathbf{Q}_0$$

(28)

At the beam ends, depending on the support conditions, boundary conditions are given by the forces and/or displacements. Consider the most general case of mixed boundary conditions at both ends of the beam. Taking into account that

$$M = EI_y\psi' + K\varphi'$$
$$Q = -Pv' + kFG\left(v' - \psi\right)$$
$$T = -P\frac{I_s}{\mu}\varphi' + K\psi' + GJ\varphi'$$

(29)

we can establish the following relations on the left and right end of the element

$$\underbrace{\begin{bmatrix} V_0 \\ \hline \Psi_0 \\ \hline \Phi_0 \\ \hline Q_0 \\ \hline M_0 \\ \hline T_0 \end{bmatrix}}_{\mathbf{R}_0} = \underbrace{\begin{bmatrix} & & & 1 & & \\ \hline & & & & 1 & \\ \hline & & & & & 1 \\ \hline -P + kFG & & & & -kFG & \\ \hline & EI_y & K & & & \\ \hline & K & -PI_s/\mu + GJ & & & \end{bmatrix}}_{\mathbf{E}} \underbrace{\begin{bmatrix} V'_0 \\ \hline \Psi'_0 \\ \hline \Phi'_0 \\ \hline V_0 \\ \hline \Psi_0 \\ \hline \Phi_0 \end{bmatrix}}_{\mathbf{Q}_0}$$

(30)

$$\underbrace{\begin{bmatrix} V_M \\ \Psi_M \\ \Phi_M \\ Q_M \\ M_M \\ T_M \end{bmatrix}}_{\mathbf{R}_M} = \underbrace{\begin{bmatrix} & & & 1 & & \\ & & & & 1 & \\ & & & & & 1 \\ -P+kFG & & & -kFG & & \\ & EI_y & K & & & \\ & K & -PI_s/\mu+GJ & & & \end{bmatrix}}_{\mathbf{E}} \underbrace{\begin{bmatrix} V'_M \\ \Psi'_M \\ \Phi'_M \\ V_M \\ \Psi_M \\ \Phi_M \end{bmatrix}}_{\mathbf{Q}_M} \qquad (31)$$

Or

$$\mathbf{R}_0 = \mathbf{E}\mathbf{Q}_0 \qquad (32)$$

$$\mathbf{R}_M = \mathbf{E}\mathbf{Q}_M \qquad (33)$$

Multiplying the left side of the matrices Eq. 28 with matrix $\mathbf{E}$ and taking into account the Eqs. 32 and 33, we obtain

$$\mathbf{R}_M = \mathbf{E}\left(-\mathbf{S}_M\mathbf{K}^{-1}\overline{\mathbf{L}}+\mathbf{T}\right)\mathbf{E}^{-1}\mathbf{R}_0 \qquad (34)$$

or

$$\mathbf{R}_M = \mathbf{F}\mathbf{R}_0 \qquad (35)$$

where

$$\mathbf{F} = \mathbf{E}\left(-\mathbf{S}_M\mathbf{K}^{-1}\overline{\mathbf{L}}+\mathbf{T}\right)\mathbf{E}^{-1} \qquad (36)$$

This is a system of six linear homogeneous algebraic equations for the 12 unknowns V_0, Ψ_0, Φ_0, Q_0, M_0, T_0, V_M, Ψ_M, Φ_M, Q_M, M_M, T_M. If homogeneous boundary conditions at the ends of the beam, which number is 6, enter into the Eq. 35 we get the homogeneous system of 6 equations with 6 unknowns.   This system, representing an algebraic eigenvalue problem, can have a nonzero solution only when the determinant of the equation system vanishes, and the natural frequencies ω can be determined as the roots of this determinant. When the frequencies are substituted back into Eq. 35 the components of vector $\mathbf{R}_0$ can be determined to the multiplicative constant factor. Now combining the equations 32, 24 and 13 the mode shapes vector $\mathbf{Q}$, corresponding to the natural frequencies ω can be found.

5.   NUMERICAL EXAMPLES

In this section, the introduced method will be employed in analyzing the free vibration of axially loaded cantilever composite Timoshenko beam with the following boundary conditions:

- The geometric boundary conditions at the cantilever end, $x = 0$
  $v = \psi = \varphi = 0$
- The natural boundary conditions at the free end, $x = l$

Bending moment (M): $EI_y\psi' + K\varphi' = 0$

Shear force (Q): $-Pv' + kFG(v' - \psi) = 0$

Torque (T): $-P\dfrac{I_s}{\mu}\varphi' + K\psi' + GJ\varphi' = 0$

To demonstrate the applicability of the proposed method, the beam model studied by Kaya and Ozgumus [10] is solved as an illustrative example. It is a cantilever glass-epoxy composite beam with a rectangular cross section with width 12.7 mm and thickness 3.18 mm. Unidirectional plies each having fibre angles of +15 are used in the analysis. The data used for the analysis are as follows:

bending rigidity (EI_y) = 0.2865 Nm2;
torsional rigidity (GJ) = 0.1891 Nm2;
bending±torsion coupling rigidity (K) = 0.1143 Nm2;
shear rigidity (kFG) = 6343.3 N;
mass per unit length (m) = 0.0544 kg/m;
mass moment of inertia per unit length (I_s) = 0.7770 x10^{-6} kgm;
length of the beam (l) = 0.1905 m.
$\rho I_y = 4.584 \times 10^{-8}$ kgm

The first six natural frequencies of the above composite Timoshenko beam are calculate and numrical results are shown in Table 1, along with the natural frequencies of Kaya and Ozgumus [10].

Table 1. The First Xix Natural Frequencies of Composite Timoshenko Beam

|	Natural frequencies [Hz]					
	P = 0		P = 7.5(compression)		P = -7.5 (tension)	
Mode	Present study	Kaya and Ozgumus	Present study	Kaya and Ozgumus	Present study	Kaya and Ozgumus
1	31.118	30.747	22.031	21.987	37.660	37.106
2	193.028	189.779	184.799	181.495	200.890	197.572
3	530.372	518.791	523.241	511.818	537.404	525.665
4	648.368	648.169	646.506	648.047	650.227	648.495
5	1013.914	986.199	1006.694	979.473	1021.075	992.878
6	1618.624	1564.751	1611.020	1558.134	1626.180	1571.338
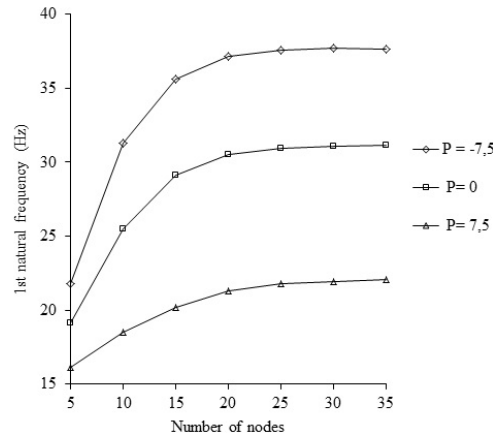
Figure 3. Convergence of the Natural Frequencies

Close agreements in natural frequencies are obtained between the proposed method and method by Kaya and Ozgumus [10]. For $k = 30$, the differences between the two methods are less than 3%. The convergence of the first natural frequency for P=0, P=7.5 and P=-7.5, is shown in the Fig. 3. It can be seen that the proposed methods converge fast–and a relatively small number of interior points are required for a good prediction of frequencies.

6.   CONCLUSIONS

In this paper a numerical method is presented for the analysis of axially loaded composite Timoshenko beam which exhibits bending-torsion coupling. The essential steps of the proposed method   includes transforming the basic governing differential equations of motion into integral equations, and then, using numerical procedure, it is possible to replace that equations with system of linear algebraic equations. The basic mathematical operation is simple and can be readily solved by the application of matrix calculus. Numerical verification demonstrates that the proposed method is reasonably accurate, i.e. the numerical approximations, in most cases, is accurate for quite low values of k.

Finally, it can be said that proposed method can serve as a convenient alternative to the similar numerical techniques in the analysis of coupled vibration of Timoshenko beam. Also it should be noted that the proposed method can be applied to all the problems of structural mechanics defined by a set of second-order ordinary differential equations of variable coefficients, with arbitrary boundary conditions, for example, to the problems of stability.

ACKNOWLEDGMENT

REFERENCES

[1]   Ansari, R., Gholami, R. and Hosseini, K., "A Sixth-order Compact Finite Difference Method for Free Vibration Analysis of Euler-Bernoulli Beams", Mathematical Sciences, 2011, Vol. 5, No. 4, pp.307-320.

[2]   Banerjee, J.R., "Dynamic Stiffness Formulation and Free Vibration Analysis of Centrifugally Stiffened Timoshenko Beams", Journal of Sound and Vibration, 2001, Vol. 247, No. 1, pp.97–115.

[3]   Banerjee, J.R., Su, H. and Jayatunga, C., "A Dynamic Stiffness Element for Free Vibration Analysis of Composite Beams and Its Application to Aircraft Wings", Computers and Structures, 2008, Vol. 86, No. 6, pp.573–579.

[4]   Berczynski, S. and Wroblewski T., "Vibration of Steel-Concrete Composite Beams Using the Timoshenko Beam Model", Journal of Vibration and Control, 2005, Vol. 11, No. 6, pp.829–848.

[5]   Biscontin, G., Morassi A. and Wendel, P., "Vibrations of Steel-Concrete Composite Beams", Journal of Vibration and Control, 2000, Vol. 6, No. 5, pp.691–714.

[6]   Borbón, F., Mirasso, A. and Ambrosini, D., "A Beam Element for Coupled Torsional-flexural Vibration of Doubly Unsymmetrical Thin Walled Beams Axially Loaded", Computers and Structures, 2011, Vol. 89, No. 13-14, pp.1406–1416.

[7]   Byron, F.W. and Fuller, R.W., "Mathematics of Classical and Quantum Physics", Dover Publications, Inc., New York, 1992.

[8]   Fu-le, L. and Zhi-zhong, S., "A Finite Difference Scheme for Solving the Timoshenko Beam Equations with Boundary Feedback", Journal of Computational and Applied Mathematics, 2007, Vol. 200, No. 2, pp.606- 627.

[9]   Hajdin, N., "A Method for Numerical Solution of Boundary Value Problems", Trans. Civ. Engng. Dept,. 1958, No. 4, pp.1-58.

[10]   Kaya, M.O. and Ozgumus Ozdemir, O., "Flexural-torsional-coupled Vibration Analysis of Axially Loaded Closed-section Composite Timoshenko Beam by Using DTM", Journal of Sound and Vibration, 2007, Vol. 306, No. 3-5, pp.495–506.

[11]   Li J., Shen, R., Hua, H. and Jin, X., "Bending–torsional Coupled Dynamic Response of Axially Loaded Composite Timoshenko Thin-walled Beam with Closed Crosssection", Composite Structures, 2004, Vol. 64, No. 1, pp.23–35.

[12]   Liu, Z., Yin, Y., Wang, F., Zhao, Y. and Cai, L., "Study on Modified Differential Transform Method for Free Vibration Analysis of Uniform Euler-Bernoulli Beam", Structural Engineering and Mechanics, An Int'l Journal, 2013, Vol. 48, No. 5, pp.697-709.

[13]   Mirtalaie, S.H., Mohammadi, M., Hajabasi, M.A. and Hejripour F., "Coupled Lateral-torsional Free Vibrations Analysis of Laminated Composite Beam using Differential Quadrature Method", Word Academy of Science, Engineering and Technology, 2012, No. 67, pp.117-122.

[14]   Pagani, A., Boscolo, M., Banerjee, J.R. and Carrera, E., "Exact Dynamic Stiffness Elements Based on One-dimensional Higher-order Theories for Free Vibration Analysis of Solid and Thin-walled Structures", Journal of Sound and Vibration, 2013, Vol. 332, No. 23, pp.6104-6127.

[15]   Pan, D., Chen, G. and Lou, M., "A Modified Modal Perturbation Method for Vibration Characteristics of Non-prismatic Timoshenko Beams", Structural Engineering and Mechanics, An Int'l Journal, 2011, Vol. 40, No. 5, pp.689-703.

[16]   Rajasekaran, S., "Free Vibration of Centrifugally Stiffened Axially Functionally Graded Tapered Timoshenko Beams Using Differential Transformation and Quadrature Methods", Applied Mathematical Modelling, 2013, Vol. 37, No. 6, pp.440-4463.

[17]   Reddy, J.N., "On Locking-free Shear Deformable Beam Finite Elements", Comput. Methods Appl. Mech. Engrg., 1997, Vol. 149, pp.113-132.

[18]   Vo, T.P., Lee, J. and Lee, K., "On Triply Coupled Vibrations of Axially Loaded Thin-walled Composite Beams", Computers and Structures, 2010, Vol. 88, No. 3-4, pp.144–153.

WIND-INDUCED RESPONSE ANALYSIS OF THE CYLINDRICAL RETICULATED MEGA-STRUCTURES

Yongjun He [1],*, Xuhong Zhou [1, 2]　and Haishun Wang [3]

[1] *Professor, College of Civil Engineering of Hunan University, Changsha 410082, P.R. China*
[2] *Professor, College of Civil Engineering of Chongqing University, Chongqing 400044, P.R. China*
[3] *graduate student, College of Civil Engineering of Hunan University, Changsha 410082, P.R. China*
*(Corresponding author: E-mail: hyj0087@163.com)

ABSTRACT: With the further increase of span of spatial structures, wind load becomes one of the governing factors in structural design. Attention is paid to wind-induced response analysis of spatial grid structures in the recent years. Research on the wind-induced responses of the cylindrical reticulated mega-structure with double-layer plane-plate grid substructures is conducted by time-history method in this paper. The basic distribution laws of the wind-induced member internal forces and nodal displacements of both the main structure and substructures are first analyzed. By detailed parametric analyses, the effect of the geometric parameters, damping ratio, load, boundary condition, and wind velocity on structural wind-induced response is then studied. Finally the structural wind-induced vibration coefficients are analyzed, and their rational values are recommended. All this work will provide theoretical guidance to the wind-resistance design of this kind of structure.

Keywords: Cylindrical reticulated mega-structure, Time-history method, Wind-induced response, Parametric analyses, Wind-induced vibration coefficient

1.　　INTRODUCTION

With the development of human society, people have put forward higher requirement for the span of spatial structures (Makowski [1]). Double-layer cylindrical reticulated structure is one kind of long span structures, which is used extensively. However, with further increase of the span, the double-layer cylindrical reticulated structure will meet some inevitable problems, such as the instability of the whole structure since the thickness-to-span ratio is too small, the buckling of struts for the members are too long and the internal forces are too large, as well as the increasing steel consumption and the corresponding economic problems. To break the restriction of large internal forces of members and structural overall instability to construct super-long-span structure, the concept of reticulated mega-structure has been proposed (He and Zhou [2]). The whole structure is made up of two levels. The first level is the large grid structure called the main structure consisting of the transverse and longitudinal latticed 3D beams, which bears all the loads and transfers them to the supporting structure. The second level is composed of substructures embedded in the large grids of the main structure, which only bears loads within the corresponding large grids and transfer them to the main structure. The structural configuration, support styles, mechanical model, static properties, and stabilities of this kind of structure have been comprehensively investigated (He and Zhou [2-3]).

Generally, the spatial structures are comparatively sensitive to wind for their long span and light weight (Lu et al. [4]). Thus, wind load is one of the governing factors in structural design. However, the research findings on wind-resistance of spatial structures are still inadequate, and the design parameters for wind-resistance of spatial structures are not perfect in the current design code. They are commonly determined by referring to those of the high-rise buildings (Mehta [5]), and this is

obviously unreasonable. Therefore, attention should be paid to the reasonable analysis and calculation of wind-induced response in design of long-span spatial structures (Chen et al. [6]). For the reticulated mega-structure, as an innovative long-span spatial structure, its wind-resistant performance is still obscure. Therefore, this paper is focused on research of the wind-induced response of the cylindrical intersecting-latticed-three-dimensional-beams-system (ILTDBS) reticulated mega-structure with double-layer plane-plate grid substructures as shown in Figure 1.

(a) Three-dimensional configuration

(b) Substructure embedded in large grid

(c) The plan of the structure with numbering of the substructures, latticed 3D arches, longitudinal beams, members, and the nodes

i: the upper chord members (UCM);
j: the lower chord members (LCM);
k: the upper diagonal braces (UDB);
m: the upper transverse members (UTM);
n: the web members (WM).

(d) Main node of the main structure, i.e. the intersection area of the latticed 3D beams

Figure 1. Cylindrical ILTDBS Reticulated Mega-structure with Double-layer Plane-plate Grid Substructures

2.   ANALYTICAL METHOD OF WIND-INDUCED RESPONSE

The calculation methods of structural wind-induced response can be divided into two categories, i.e., the frequency domain method and time history method (Oskoei and McClure [7]). The former is to solve the structural wind-induced response from power spectrum, and it can objectively reflect the regularity of strong wind (Soares and Mansur [8]). The calculation complexity of the frequency domain method is much less than that of the time history method, because it is to directly calculate the statistical result of random response in frequency domain. Nevertheless, it is difficult to determine the number of vibration modes accurately for the long span space grid structures

(Uematsua et al. [9]). For the time history method, the dynamic equilibrium equation is directly integrated according to the adopted wind velocity spectrum, and the nodal displacement, velocity as well as the acceleration at various moments under wind load can be calculated by step-by-step integration (Thai and Kim [10]). The stochastic simulation time history method (Zhang [12] and Masters et al. [13]), an effective analysis method for response of nonlinear structures under stochastic dynamic load, is adopted in this paper to study the structural wind-induced response characteristics. The analysis process can be described as follows.

(1) According to the statistical characteristics of wind load, the artificial wind velocity time history series (excitation samples) with specified spectral density and spatial correlation are generated and converted into wind pressure time history series applied on structure (Karmakar et al. [14]). And the improved AR (Auto-Regressive) method is adopted to realize the numerical simulation of random wind load with consideration of temporal and spatial correlation (Owen et al. [15]).

(2) The structural dynamic equilibrium equation under the stochastic wind load $P(t)$ is established by finite element method, which can be expressed as

$$[M]\{\ddot{U}\} + [C]\{\dot{U}\} + [K]\{U\} = \{P(t)\} \tag{1}$$

in which, $[M]$, $[C]$, and $[K]$ are the mass, Rayleigh damping [11], and stiffness matrices, respectively; $\{U\}$, $\{\dot{U}\}$, $\{\ddot{U}\}$, and $\{P(t)\}$ are the nodal displacement, velocity, acceleration, and the wind load vectors, respectively. The Newmark-β step-by-step integration method (Soares and Mansur [16]) is then adopted to solve the dynamic equation in time domain, and the structural geometrical nonlinearity is considered by Newton-Raphson iterative technique (Kim et al. [17]) to obtain the structural wind-induced response.

(3) Statistical analysis on the response samples is carried out to obtain the required statistical information, such as the means and standard deviations of the nodal displacements, velocities, accelerations and those of the member internal forces, as well as the corresponding spectrum characters. And the structural wind-induced response characteristics can thus be determined.

The Davenport's power spectrum (Davenport [18] and Iwatani [19]) is adopted to simulate the wind velocity time history series of various nodes of the structure with consideration of temporal and spatial correlation by AR model (Isyumov [20]). The corresponding computational program for simulation of stochastic wind field and analysis of structural wind-induced response is developed. Numerical examples indicate that this method is feasible and highly efficient for analysis of wind-induced response of long span spatial structures. Theoretically, this method can be adopted for any system and excitation. Also, the whole process information of structural dynamic response can be obtained.

3.   BASIC WIND-INDUCED RESPONSE CHARACTERS
OF THE RETICULATED MEGA-STRUCTURE

3.1   Analytical Model

Take the cylindrical reticulated mega-structure with span of 80m to do analysis. The basic model and concerned parameters can be described as follows. The ratio of rise to span of the main structure $F = 0.2$, height of the latticed 3D beams is 3.6m, numbers of large grids of the main structure is 4×4, and the number of upper chord small grids within a latticed 3D beam segment

$n = 6$, The double-layer plane-plate grid substructures are imbedded in the main structure by perimeter-points support style as shown in Figure 1(b), the number of the upper chord small grids of each substructure is 9×9. The whole structure consists of steel round tube members, and the members are connected by welded spherical joints. The cross section of members in the main structure (S_m) and that in the substructures (S_s) are $S_m = \varphi 140 \times 4.5$ and $S_s = \varphi 76 \times 4.0$, respectively. The yield stress of the steel is 235MPa and the damping ratio is taken as 0.02. The fixed-hinged supports are set on the upper and lower chord joints of the main nodes along the two longitudinal edges of the main structure as described in Reference (He and Zhou [2]), and the vertical uniform loads of $1\,\text{kN}/\text{m}^2$ are applied on the upper surface of the structure. The plan of the structure with numbering of some members is shown in Figure 1(c). In the figure, A1-A3, L1-L5, and S1-S8 denote the numberings of the latticed 3D arches, longitudinal latticed 3D beams, and the substructures, respectively. Only half of the structure is displayed for its symmetry. Also, not all the substructures braced in the large grids are shown in the figure for clarity.

The basic wind velocity under the standard condition, i.e. the 10-minute mean wind velocity at a height of 10m above the ground, is taken as 25m/s, and the direction of the wind is along the x-axis as shown in Figure 1. The air density is $1.225\,\text{kg/m}^3$. And the terrain roughness of C-class is considered. Obviously, the number of samples increases with increase of the wind duration in wind-induced response analysis, and thus the precision of the statistical result of the response increases. However, the increase of wind duration will inevitably result in decline of the calculation efficiency. Therefore, giving consideration to both the precision and calculation efficiency as discussed in detail in our previous work (He et al. [21]), the wind duration and time step in analysis are taken as 120s and 0.1s, respectively.

As we know, the wind load is composed of two parts, i.e., the mean and fluctuating ones. The average value of the structural response reflects the action effect of mean wind (the equivalent static wind) to a certain degree, whereas the standard deviation indicates the fluctuating effect of wind. The standard deviation of the structural response under the fluctuating wind velocity with a certain assurance rate is usually taken as the design value of fluctuating response in practical engineering (Jakobsen [22]). Thus the distribution and variation laws of means and standard deviations of the structural responses are taken as the main indices in analysis. Also, the calculated result shows that, the longitudinal (y-directional) displacement component of any node of the structure is extremely small in comparison with the transverse (x-directional) and vertical (z-directional) ones. Therefore, this paper is focused on the transverse and vertical nodal displacements in research of the structural displacement response characteristics.

3.2   Wind-induced Response of the Main Structure

3.2.1   Internal force response characteristics

From the calculated results (the concrete data are not listed), it is found that the wind-induced internal forces of various members of the latticed 3D arches at both ends of the structure are relatively smaller than those of the corresponding members of various middle latticed 3D arches. The internal force distribution laws of various latticed 3D arches are approximately identical. Therefore, the middle latticed 3D arch A3 of the structure is typically taken to study in this paper. The internal force means (IFM) and standard deviations (IFSD) of various types of members in the latticed 3D arch are displayed in Figures 2 and 3, respectively. In the figures, UCM, LCM, UDB, UTM, and WM denote the upper and lower chord members, upper diagonal braces, upper transverse members, and the web members, respectively, as shown in Figure 1(d), and the same as the following figures.
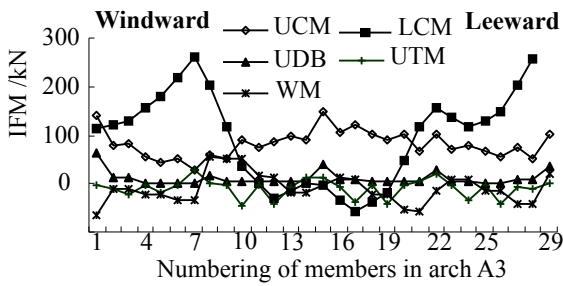
Figure 2. Distribution of the Internal Force Means (IFM) of Various Members in the Latticed 3D Arch A3
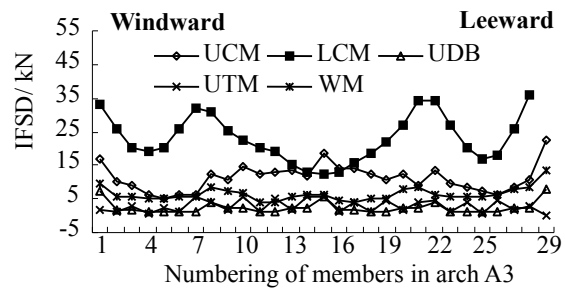
Figure 3. Distribution of the Internal Force Standard Deviations (IFSD) of Various Members in the Latticed 3D Arch A3

It can be seen that, the internal forces of the upper and lower chord members are comparatively large and thus they are the main load-bearing components. The maximum wind-induced internal forces exist in the lower chord members at the bottom of the leeward side of the latticed 3D arch. The wind-induced internal forces of various types of members basically show symmetrical distribution with respect to the top of the arch. The internal forces of various types of members all fluctuate along the arch and the local extrema emerge in the intersection areas of the transverse latticed 3D arch with various longitudinal latticed 3D beams. The internal force fluctuation range of the lower chord members is very large. The internal forces of the lower chord members at the middle of the windward side and the bottom of the leeward side of the latticed 3D arch are comparatively large, while those on the top of the arch are relatively small. The internal force fluctuation range of the upper chord members is slightly smaller than that of the lower chord members, and the internal forces nearly present W-shaped distribution along the latticed 3D arch with comparatively large values at the top and bottoms of both sides of the arch. The upward suction force of wind on the leeward side leads to increase of the tensile forces of the upper chord members and decrease of those of the lower chord members. This is the main reason for difference of the internal force distribution law between the upper and lower chord members. The internal forces of the web members, upper diagonal braces and the transverse members are relatively small. The fluctuation laws of them are not remarkable and the fluctuation ranges are very small.

Calculated results show that, the wind-induced internal forces of the upper and lower chord members of various longitudinal latticed 3D beams are greatly smaller than those of the latticed 3D arches. The internal forces of members of the top latticed 3D beam L3 are obviously larger than those of the corresponding members of the middle and lower latticed 3D beams. However, the internal force distribution laws of various parallel longitudinal latticed 3D beams are approximately identical and show symmetrical distribution with respect to the midpoints of the latticed 3D beams. Therefore, one half of the top latticed 3D beam L3 is taken to study, and the internal force means and standard deviations of various types of members in the latticed 3D beam are displayed in Figures 4 and 5, respectively.

Obviously, the largest internal force of the longitudinal latticed 3D beam exists in the upper transverse members. The internal forces of the upper transverse members fluctuate along the axial direction of the longitudinal latticed 3D beam with local extrema in the intersection areas with various transverse arches. Also, the internal forces of the lower chord members in the middle of the end segment (i.e., near by the Section A-A as shown in Figure 4(c)) are comparatively large, and there is not notable fluctuation in other place. The reason is that the constraint of the end latticed 3D arch on the longitudinal latticed 3D beams is comparatively weak, which increases the local

wind-induced vibration effect of the longitudinal latticed 3D beams in these places. The internal forces and their fluctuation ranges of other types of members are comparatively small.
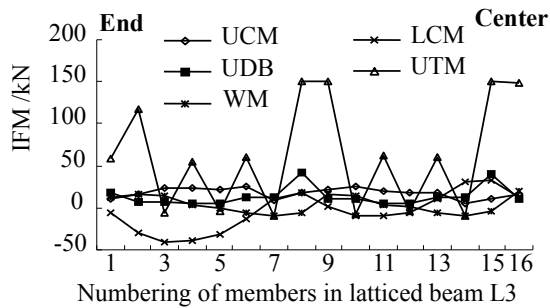

Figure 4. Distribution of IFM of Various Members in the Longitudinal Latticed 3D Beam L3
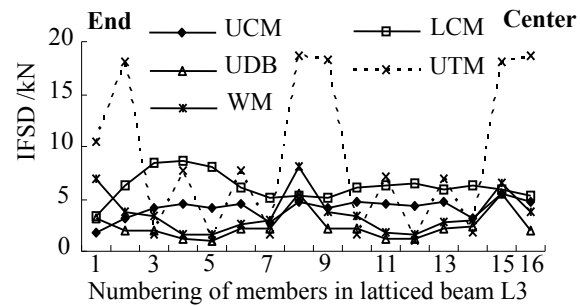
Figure 5. Distribution of IFSD of Various Members in the Longitudinal Latticed 3D Beam L3

3.2.2   *Displacement response characteristics*

From the calculated results (the concrete data are not listed) it can be seen that, the nodal displacement distribution laws of various latticed 3D arches are basically identical expect that the nodal displacements of various middle arches are slightly larger than those of the both end arches. Moreover, the nodal displacement distribution laws of various parallel longitudinal latticed 3D beams are also approximately identical. However, for various parallel longitudinal latticed 3D beams, the largest upper chord nodal displacement exists in the latticed 3D beam L4 located in the middle of the leeward side of the structure; while the largest lower chord nodal displacement exists in the latticed 3D beam L2 in the middle of the windward side. Here, the middle latticed 3D arch A3 and top longitudinal latticed 3D beam L3 are typically taken to study the nodal displacement distribution law of the structure in detail. The means and standard deviations of the horizontal and vertical displacements of various nodes of the latticed 3D arch A3 and beam L3 are shown in Figs. 6, 7, 8, and 9, respectively. In the figures, UH, UV, LH, and LV present the horizontal and vertical displacements of the upper chord nodes and those of the lower chord nodes, respectively; the numbering of nodes is identical with that of the corresponding members as shown in Figure 1(c); and the same as the following figures.

As shown in Figures 6 and 7, the vertical displacements of both the upper and lower chord nodes are larger than the horizontal ones, and the nodal displacement increases gradually from the bottom to top of the arch. Therefore, the vertical displacement of the node on the top of the latticed 3D arch is the major governing factor in wind-resistance design. It can be seen from Figures 8 and 9 that, the nodal displacements of the longitudinal latticed 3D beam show symmetrical distribution with respect to the midpoint of the latticed 3D beam, and the vertical component of each is greatly larger than the corresponding horizontal one. The vertical displacements of the upper chord nodes are basically consistent with those of the corresponding lower chord nodes, while the horizontal displacements of the lower chord nodes are slightly larger than those of the corresponding upper chord nodes. The vertical displacements of the nodes at the end of the longitudinal latticed 3D beam are slightly smaller than those of the others in it, but the different in horizontal displacements of various nodes is very small. In a word, for the longitudinal latticed 3D beam, the nodal displacement fluctuation along its longitudinal axis is not remarkable, and the vertical displacement is the major governing factor in design.
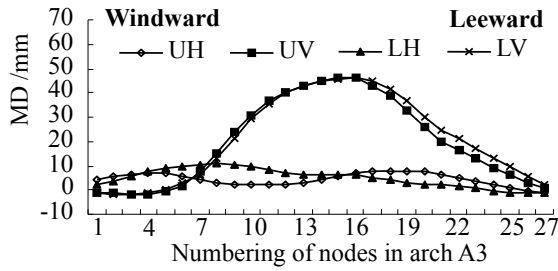
Figure 6. The Displacement Means (DM) of Various Nodes in the Latticed 3D Arch A3
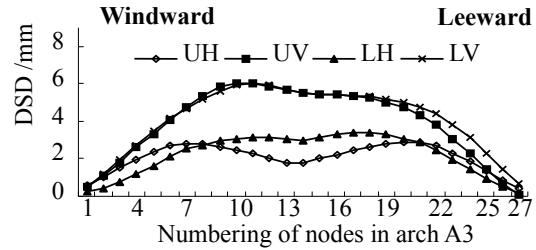

Figure 7. The Displacement Standard Deviations (DSD) of Various Nodes in the Latticed 3D Arch A3
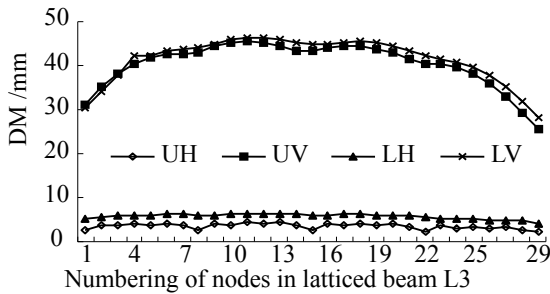

Figure 8. The DM of Various Nodes in the Longitudinal Latticed 3D Beam L3
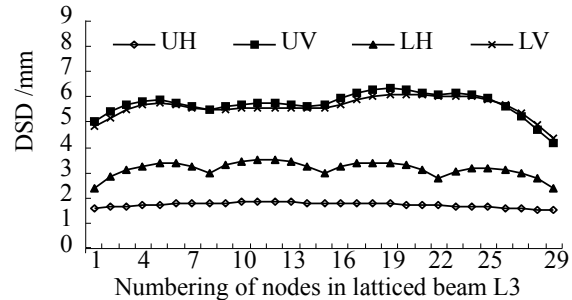
Figure 9. The DSD of Various Nodes in the Longitudinal Latticed 3D Beam L3

3.3   Wind-induced Response of the Substructures

3.3.1   Internal force response characteristics

Figures 10 and 11 depict the distributions of the wind-induced internal force means and standard deviations of various members in the substructures along the transverse section B-B. It can be seen that the internal forces of the transverse (x-directional) upper and lower chord members (TUCM and TLCM) in the upper substructure are obviously larger than those in the lower substructure. And the member internal forces of the lower substructure on the leeward side are larger than those on the windward side. The internal forces of the upper chord members are larger than those of the lower chord and other types of members, thus the upper chord members are the main load-bearing components. Also, the internal forces of the transverse upper chord members are obviously larger than those of the longitudinal (y-directional) members (LUCM). The internal force variation range of the web members is small, so these members can be designed according to the constructional requirement. The member internal force distribution laws of various substructures along the transverse direction are basically identical. That is, the closer to the center of the substructures, the larger the internal forces of the members are, except the internal forces of the web members, which scarcely fluctuate.

From Figures 12 and 13 it can be seen that, the member internal force distribution laws of various substructures with same height along the longitudinal direction are nearly identical. Moreover, the distribution laws of the fluctuating wind-induced internal forces are close to those of the mean internal forces. The internal force distribution laws of the longitudinal upper and lower chord members along the longitudinal direction are similar to those of transverse chord members along the transverse direction as shown in Figures 10 and 11, so they are not depicted again in here. Additionally, the internal forces of the transverse upper chord members basically do not fluctuate along the longitudinal direction.
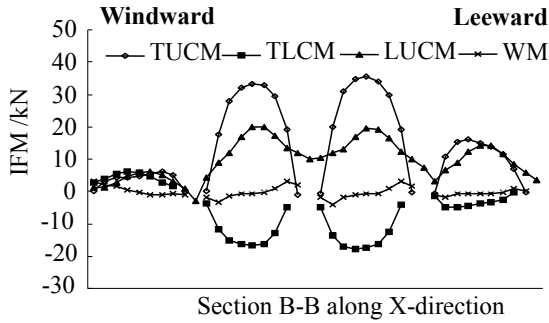
Figure 10. The IFM of Various Members in
the Substructures along Section B-B
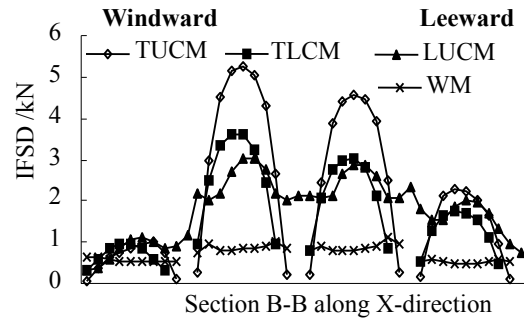
Figure 11. The IFSD of Various Members
in the Substructures along Section B-B
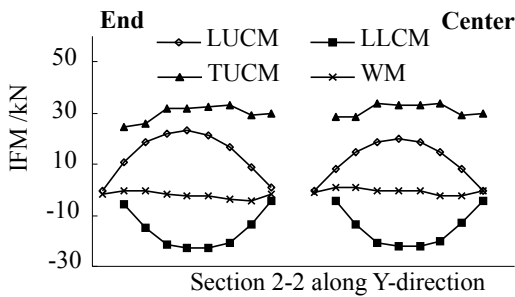
Figure 12. The IFM of Various Members in
the Substructures along Section 2-2
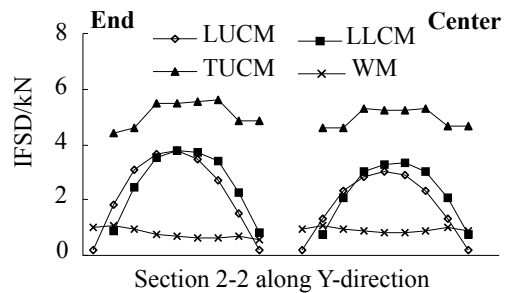
Figure 13. The IFSD of Various Members
in the Substructures along Section 2-2

3.3.2   *Displacement response characteristics*

Figures 14 and 15 depict the variation of the means and standard deviations of wind-induced nodal displacements of the substructures along the section B-B, respectively. It can be seen that, under the action of mean wind, there is not remarkable difference in the nodal transverse horizontal displacements between various substructures, while the difference in the nodal vertical displacements is notable. The nodal displacements of the upper substructures are larger than those of the lower substructures, and the displacements of the nodes on the leeward side are slightly larger than those on the windward side. The nodal vertical displacements of upper substructures are greatly larger than the horizontal ones. Under fluctuating wind load, the nodal displacement response of various substructures basically shows symmetrical distribution with respect to the top of the structure. The nodal displacements of the upper substructures are larger than those of the lower substructures. Additionally, the nodal vertical displacements are obviously larger than the horizontal ones, this indicates that the wind-induced vibration of the substructures is mainly along the vertical direction. Also, the nodal displacements of the lower substructures increase gradually from the bottom up, while those of each upper substructure decrease gradually from the center to both sides.
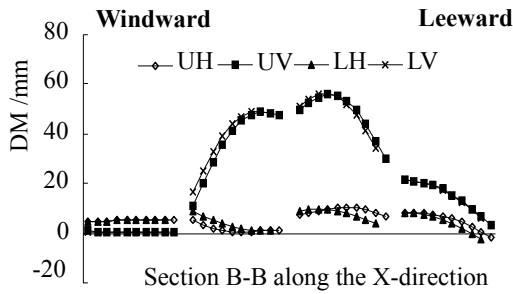
Figure 14. The Displacement Means (DM) of Various Nodes in the Substructures along Section B-B
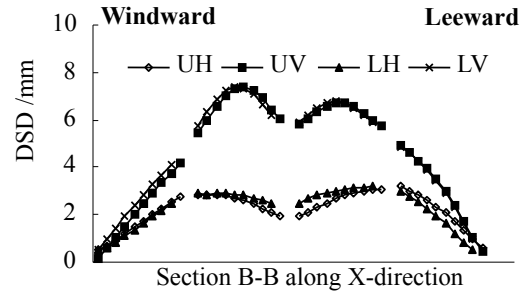

Figure 15. The Displacement Standard Deviations (DSD) of Various Nodes in the Substructures along Section B-B

Half of the structure is considered for the structural symmetry to investigate the nodal displacement distribution laws of the substructures with the same height along the longitudinal direction. The variation laws of the means and standard deviations of wind-induced nodal displacements of the substructures along the longitudinal section 3-3 are shown in Figures 16 and 17, respectively. It can be seen that, the magnitudes and distribution laws of nodal displacements of various substructures with same height are nearly identical along the longitudinal section. And the nodal displacements of the central substructures are slightly larger than those of the substructure at the end of the structure. Additionally, there is not remarkable variation in the nodal transverse horizontal displacements of each substructure along the longitudinal direction, while the nodal vertical displacements decrease gradually from the center to both sides of the substructure.
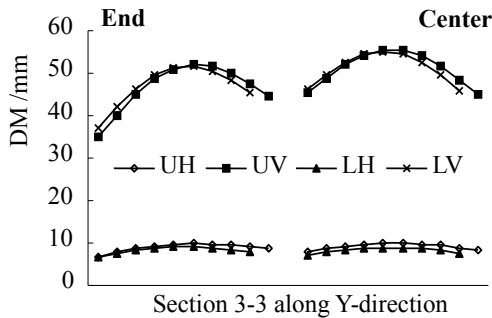

Figure 16. The DM of Various Nodes in the Substructures along Section 3-3
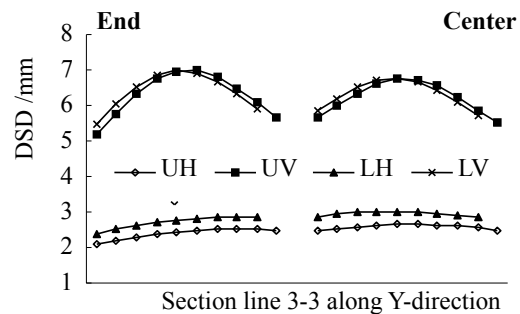
Figure 17. The DSD of Various Nodes in the Substructures along Section 3-3

4.   PARAMETRIC ANALYSES

For the structure with given span, the wind-induced response behaviors must be different if different values of various parameters are taken. Thereby, parametric analyses are carried out in the this section. The standard deviations of the structural maximum wind-induced responses (including the maximum member internal force and nodal displacement) are taken as the indices to study the influence of various parameters on the wind-induced dynamic behaviors. And the structure with span of 80m is still considered. When the influence of one parameter is investigated by changing its value to do analysis, the other parameters keep constant and identical with those described in *Section 3.1*.

4.1   Influence of the Structural Ratio of Rise to Span - *F*

Consider different values of the structural ratio of rise to span *F*, such as 1/8, 1/6, 1/5, 1/4, and 1/3, respectively. The relational curves of the wind-induced internal force and displacement versus *F* are displayed in Figures 18 and 19, respectively.
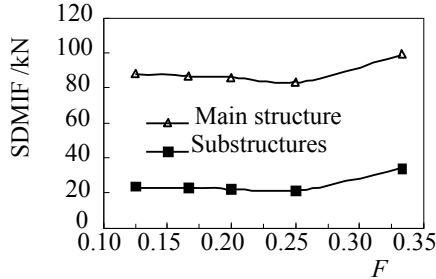

Figure 18. Relationship between the Standard Deviation of Maximum Internal Force (SDMIF) and the Ratio of Rise to Span of the Main Structure -*F*
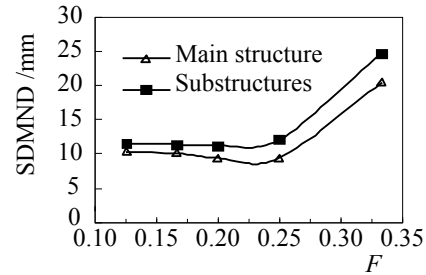
Figure 19. Relationship between the Standard Deviation of Maximum Nodal Displacement (SDMND) and the Ratio of Rise to Span of the Main Structure -*F*

It can be seen that, both the standard deviation of the maximum internal force and that of the maximum nodal displacement basically keep constant first but increase sharply when *F* exceeds 1/4 with increase of *F*. This indicates that the structural wind-induced dynamic effect will be very remarkable when the ratio of rise to span is large. Therefore, the structural ratio of rise to span should be no more than $1/4$ to keep good wind-resistant behavior.

4.2   Influence of the Cross section of Members

First, let the cross section of members in the substructures $S_s = \phi 76 \times 4.0$, and consider different cross sections of members in the main structure S_m such as $\varphi 140 \times 4.5$, $\varphi 152 \times 5.0$, $\varphi 168 \times 5.5$, and $\varphi 180 \times 7.0$, respectively. Then, let $S_m = \phi 140 \times 4.5$, and take different values of S_s such as $\phi 76 \times 4.0$, $\varphi 108 \times 4.5$, and $\varphi 140 \times 4.5$ to do analyses, respectively. The relational curves of the standard deviations of the maximum wind-induced internal force and displacement versus S_m and S_s are displayed in Figures 20, 21, 22, and 23, respectively.

It can be seen that, the standard deviation of the maximum wind-induced internal force of the main structure basically keeps constant and that of the substructures increases with increase of the cross section of members of the main structure, while the former increases and the latter basically keeps constant with increase of the cross section of members of the substructures. However, the standard deviation of the maximum wind-induced displacements of both the main structure and substructures decrease with increase in the cross section of members of whether the main structure or the substructures. On the whole, the structural rigidity can be enhanced by increase of the cross section of members, and the wind-resistant behavior of the structure can be improved, but the dynamic effect of member internal forces will also increase to a certain degree. Therefore, the increase of cross section of members should be moderate.
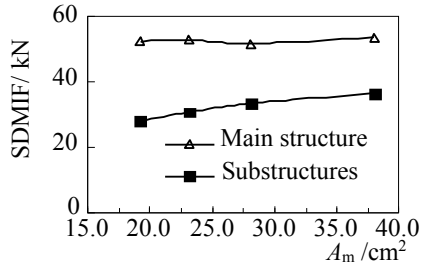
Figure 20. Relationship between the SDMIF and Sectional Area of Members in the Main Structure -A_m
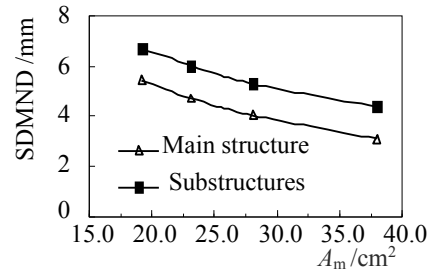
Figure 21. Relationship between the SDMND and Sectional Area of Members in the Main Structure -A_m
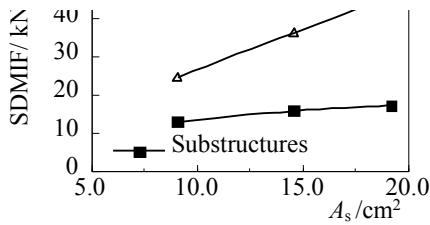
Figure 22. Relationship between the SDMIF and Sectional Area of Members in the Substructures -A_s
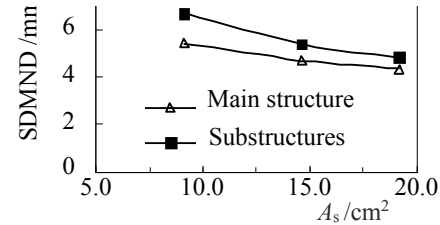
Figure 23. Relationship between the SDMND and Sectional Area of Members in the substructure -A_s

4.3   Influence of the Damping Ratio

In this section, different values of the damping ratio such as 0.01, 0.02, 0.03, 0.04, and 0.05 are considered, respectively. The relational curves of the standard deviations of the maximum wind-induced internal force and displacement with the damping ratio are displayed in Figures 24 and 25, respectively. It can be seen that both the standard deviation of the maximum wind-induced internal force and that of the maximum displacement decrease with increase of the damping ratio, but the magnitude of decrease is very small. Additionally, the variation in damping ratio of steel lattice shell structure is actually inappreciable. Therefore, the influence of change in damping ratio on structural wind-induced dynamic behavior can be basically ignored.
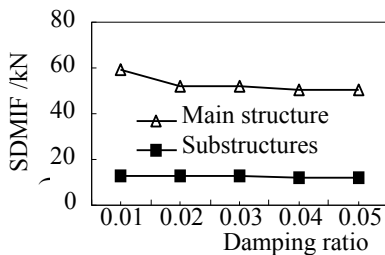
Figure 24. Relationship between the SDMIF and Damping Ratio
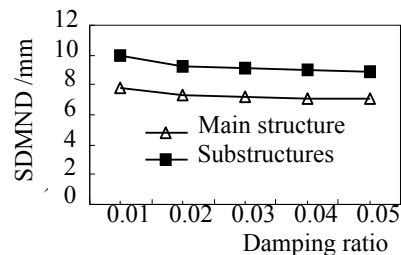
Figure 25. Relationship between the SDMND and Damping Ratio

4.4   Influence of the Load

Different values of the vertical uniform applied load such as 0.2, 0.5, 1.0, 2.0, and $3.0\,\text{kN}/\text{m}^2$, are considered in this section. The relational curves of the standard deviations of the maximum wind-induced internal force and displacement with the applied load are displayed in Figures 26 and

27, respectively. It can be seen that, the standard deviation of the maximum internal force and that of the maximum displacement slightly with increase of the applied load. That is, the fluctuating effect of structural wind-induced response increases slightly with increase of the applied load. Thus, for this kind of structure, the variation of the roof covering material has small influence on the structural wind-induced dynamic behavior.
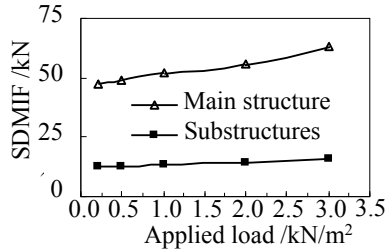

Figure 26. Relationship between the SDMIF and Applied Load
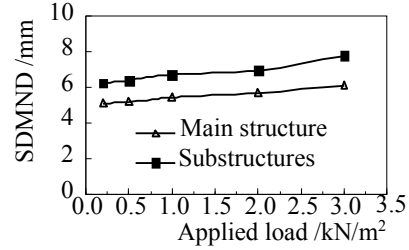
Figure 27. Relationship between the SDMND and Applied Load

4.5 Influence of the Mean Wind Velocity

Consider different standardized wind velocities such as 20, 25, 30, and 35m/s, respectively. The relational curves of the standard deviations of the maximum wind-induced internal force and displacement with the mean wind velocity are displayed in Figures 28 and 29, respectively. Obviously, the fluctuating effect of the wind-induced internal force and displacement increases linearly with increase of the mean wind velocity. That is, the magnitude of mean wind velocity has notable influence on dynamic effect of the structural wind-induced response.
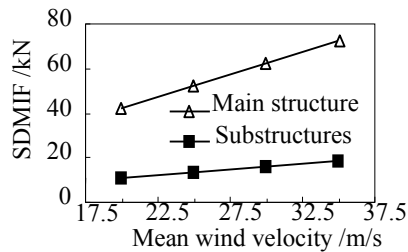

Figure 28. Relationship between the SDMIF and Mean Wind Velocity
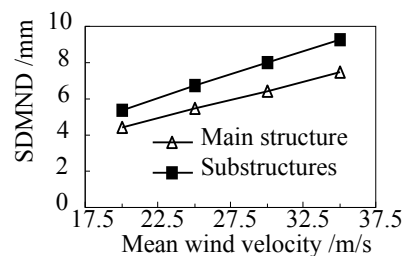
Figure 29. Relationship between the SDMND and Mean Wind Velocity

4.6 Influence of the Support Conditions

Different support styles are taken into consideration in this section, and the standard deviations of the maximum wind-induced internal forces and displacements under different support conditions are summarized in Table 1. In the table, the support styles B1 and B2 denote that the fixed-hinged supports are set on the lower and upper chord joints of the main nodes along the two longitudinal edges of the main structure, respectively; B3 presents that the fixed-hinged supports are set on both the upper and lower chord joints of the main nodes along the two longitudinal sides of the main structure; B4 means that the fixed-hinged supports are set on the lower chord joints of the main nodes along the four edges of the main structure; and B5 denotes that the fixed-hinged supports are set on the upper and lower chord joints of the main nodes along the two longitudinal edges and the lower chord joints of the main nodes along the two ends of the main structure. The details of various support styles were described in our previous work (He and Zhou [2]).

Table 1. The Wind-induced Responses of the Structures under Different Support Conditions

Support style		B1	B2	B3	B4	B5
The standard deviation of maximum member internal force /kN	In the main structure	61.613	61.074	45.894	49.463	66.509
	In the substructures	14.744	15.250	14.656	13.868	19.726
The standard deviation of maximum nodal displacement /mm	In the main structure	8.780	10.122	6.372	7.638	8.248
	In the substructures	10.164	10.420	7.940	8.960	11.003

It can be seen that, the dynamic responses of the structure with support style B4 are somewhat smaller than those with support style B1. That is, when the fixed-hinged supports are only set on the lower chord joints of the main nodes along the two longitudinal edges of the main structure, the setting of supports on the lower chord joints of the main nodes along the two ends of the main structure can slightly improve the structural wind-resistant behavior. However, comparing styles B3 with B5 indicates that, when the fixed-hinged supports are set on the upper and lower chord joints of the main nodes along the two longitudinal edges of the main structure, the supports set along the two ends of the main structure will cause not improvement but degeneration of the structural wind-resistant behavior remarkably. Therefore, style B3, in which the fixed-hinged supports are set on the upper and lower chord joints of the main nodes along the two longitudinal edges of the main structure, is the best arrangement of supports for good wind-resistant behavior of the structure. And the second one is the case that the fixed-hinged supports are set on the lower chord joints of the main nodes along the four sides of the main structure. Apparently, the support styles B1, B2, and B5 are all not good for wind-resistance of the structure for either overabundance or insufficiency of the supports.

5.   ANALYSIS OF WIND-INDUCED VIBRATION COEFFICIENT

The wind load is composed of the mean and fluctuating components. The response to the mean wind can be determined by static analytical method, which is relatively simple. However, the fluctuating wind is stochastic dynamic load, and the structural response should be solved by stochastic dynamic theory, which is obviously very complicated. In practical engineering, people always hope that the structural dynamic response can be dealt by static analytical method. Therefore, an equivalent static magnification coefficient, i.e. wind-induced vibration coefficient, should be introduced. Then the resultant response may be expressed as the product of the mean response and the wind-induced vibration coefficient.

The wind-induced vibration coefficients introduced in the current design code are determined based on the wind-induced vibration characteristics of high-rise structures, whose vibration displacements mainly depend on the first-order vibration mode. However, for a long span spatial structure, its natural frequency distribution is dense, and the structural response is not simply linear with the load. Therefore, the wind-induced vibration coefficient distribution in the structure is generally comparatively complicated.

Many scholars have studied the calculation method of wind-induced vibration coefficient of long-span spatial structures, and the wind-induced vibration coefficient was proposed based on responses, which was defined as the ratio of the possible maximum wind-induced response to the mean response of the structure in the wind duration (Chen et al. [23] and Uematsu et al. [24]). Also, the wind-induced vibration coefficient of element internal force and that of nodal displacement are commonly adopted. The wind-induced vibration coefficient of internal force β_{fi} of any element i and that of displacement β_{dj} of any node j can be expressed as follows.

$$\beta_{fi} = 1 + \mu \frac{\sigma_{fi}}{u_{fi}} \tag{2}$$

$$\beta_{dj} = 1 + \mu \frac{\sigma_{dj}}{u_{dj}} \tag{3}$$

in which, u_{fi} and σ_{fi} are the mean and standard deviation of wind-induced internal force of element i, respectively; u_{dj} and σ_{dj} are those of wind-induced displacement of node j; μ is the peak factor.

The method has rationality, but it is not convenient for being used in practical engineering since the wind-induced vibration coefficients are very numerous. Statistic result shows that, the fluctuating component corresponding to the large wind-induced response is generally relatively large. Figures 30 and 31 depict the relationship of the standard deviation with the maximum and mean of the wind-induced internal force of each member, respectively.

It can be seen that, the standard deviation, i.e., the fluctuating component of the wind-induced member internal force is nearly linear with the maximum and mean values, and the same as the characteristics of the nodal displacement response. This is also illustrated by the similarity in distribution patterns of the means and corresponding standard deviations of wind-induced responses as shown in Figures 2-17. Therefore, the difference of the wind-induced vibration coefficients at different places in a structure given by Eq. 2 or 3 is not very remarkable. The concrete data are omitted. Accordingly, a singe wind-induced vibration coefficient can thus be adopted to reflect the whole wind-induced vibration character of this kind of structure except for several singular points.
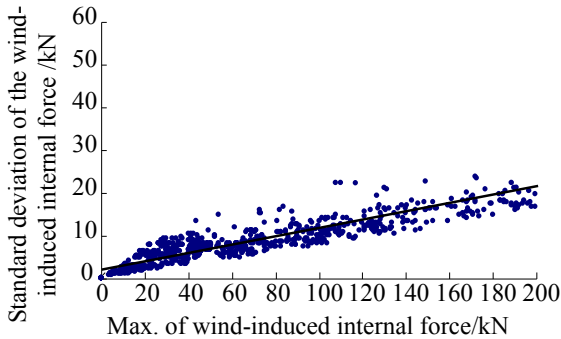

Figure 30. Relationship between the Standard Deviation and Max. of the Wind-induced Internal Force of Member
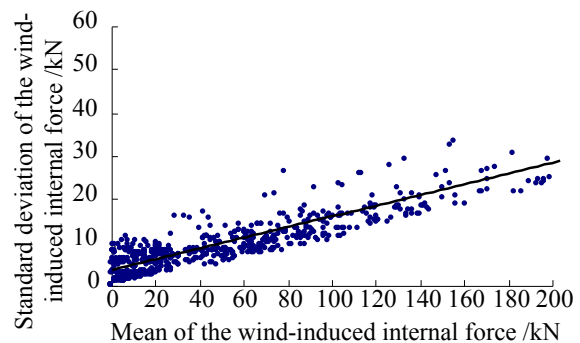
Figure 31. Relationship between the Standard Deviation and Mean of the Wind-induced Internal Force of Member

Results show that some wind-induced vibration coefficients may be too large, those are so-called singular points. The main reason is that the means of the responses are small, while the corresponding standard deviations of the fluctuating responses are relatively large. Actually, the resultant responses of these nodal displacements or element internal forces are generally comparatively small, so they are not the governing factors though their wind-induced vibration coefficients are large. Obviously, it is the peak nodal displacements and member internal forces of the structure that play a dominant role in design. Hence, for the structural governing wind-induced vibration coefficient β can be defined as follows based on the envelope idea,

$$\beta = \frac{(u)_{max} + \mu(\sigma)_{max}}{(u)_{max}} = 1 + \mu\frac{(\sigma)_{max}}{(u)_{max}} \tag{4}$$

in which, $(\sigma)_{max}$ and $(u)_{max}$ are the maximum standard deviation and mean of various responses, and the peak factor $\mu = 3.5$ (Lu et al. [25])。

The formula of the governing wind-induced vibration coefficient depends on the maximum standard deviation and mean of various responses, and it is reasonable to take it as the single design wind-induced vibration coefficient to avoid the inconvenience of numerous wind-induced vibration coefficients. Actually, this governing wind-induced vibration coefficient is safe in structural design, since the standard deviation corresponding to the maximum mean response is not always just the maximum one and thus the calculated maximum resultant response $(u)_{max} \cdot \beta = (u)_{max} + \mu(\sigma)_{max}$ will be larger than the actual value.

Based on above discussion, the governing wind-induced vibration coefficient of the cylindrical reticulated mega-structures given by Eq. 4 is investigated in detail in this section based on large numbers of numerical examples with different parameters. The results show that, the displacement or internal force governing wind-induced vibration coefficient increases first and then decreases gradually with increase of the ratio of rise to span, and reaches the maximum value when the ratio of rise to span is 1/5. It also increases gradually with increase of the structural span and the average wind velocity. Nevertheless, the governing wind-induced vibration coefficients of the structures with different parameters basically keep between 1.4 and 1.7. Therefore, it can be safely taken as 1.5-1.8 to simplify the design process in practical engineering.

6.   CONCLUSION

The wind-induced responses of the cylindrical LITDBS reticulated mega-structure braced with plane-plate grid substructures are studied by time history method in this paper. The basic distribution laws of the wind-induced internal forces and displacements of both the main structure and substructures are first analyzed. Then the influence of various parameters on the wind-induced responses is investigated in detail. Finally the structural wind-induced vibration coefficient is studied. The main conclusions can be drawn as follows.

(1) The upper and lower chord members of various latticed 3D arches are the main load-carrying elements. The largest wind-induced internal forces appear in the lower chord members of the bottom of the arches on the leeward side of the structure. Additionally, the intersection areas of the latticed 3D arches and longitudinal beams are the main load-carrying places of the main structure, to which more attention should be paid in design. Also, the wind-induced internal forces of the substructures are far smaller than those of the main structure, and the transverse upper chord members are the main stressed elements of the substructures.

(2) The main governing displacement in wind-resistance design exists on the top of the arches, and the peak displacement of the substructures is slightly larger than that of the main structure under the action of wind. Moreover, the distribution of the wind-induced nodal displacements, whose main component is the vertical one, is relatively uniform.

(3) The structural wind-induced dynamic effect will be very remarkable when the ratio of rise to span is large, and the structural ratio of rise to span should not be more than $1/4$ to keep good wind-resistant behavior. The variation of the dead load and mean wind velocity has small influence on the structural wind-induced dynamic behavior, but the impact of change in damping ratio on it can be basically ignored.

(4) The structural rigidity can be enhanced by increase of the cross section of members, and the wind-resistant behavior of the structure can be improved, but the dynamic effect of member internal forces will also increase to a certain degree. Therefore, the increase of cross section of members should be moderate. The best arrangement of supports for good wind-resistant behavior of the structure is to set the fixed-hinged supports on the upper and lower chord joints of the main nodes along the two longitudinal edges of the main structure.

(5) The governing wind-induced vibration coefficient of this kind of structure basically keeps between 1.4 and 1.7, and it can be safely taken as 1.5-1.8 in design of practical engineering.

ACKNOWLEDGEMENTS

REFERENCES

[1]   Makowski, Z.S., "Space Structure-A Review of Development in Last Decade", Space Structure IV, London, 1993, pp. 2-15.
[2]   He, Y.J. and Zhou, X.H., "Static Properties and Stability of Cylindrical ILTDBS Reticulated Mega-structure with Double-layer Grid Substructures", Journal of Constructional Steel Research 2007, Vol. 63, No. 12, pp. 1580-1589.
[3]   Zhou, X.H., He, Y.J. and Xu, L., "Formation and Stability of a Cylindrical ILTDBS Reticulated Mega-structure Braced with Single-layer Latticed Membranous Shell Substructures", Thin-Walled Structures, 2009, Vol. 47, No. 5, pp. 537-546.
[4]   Lu, C.L., Li, Q.S., Huang, S.H., Chen, F.B. and Fu, X.Y., "Large Eddy Simulation of Wind Effects on a Long-span Complex Roof Structure", Journal of Wind Engineering and Industrial Aerodynamics, 2012, Vol. 100, pp. 1-18.
[5]   Mehta, K.C., "Wind Load Standards", Wind Effects on Buildings and Structures-Proceedings of Jubileum Conference on Wind Effects on Building and Structures, Porto Alegre, Brazil, 1998, pp. 307-313.
[6]   Chen, B., Wu, Y. and Shen, S.Z., "A New Method for Wind-induced Response Analysis of Long Span Roofs", International Journal of Space Structures, 2006, Vol. 21, No. 2, pp. 93-101.
[7]   Oskoei, S.A.G. and McClure, G., "Dynamic Analysis of Cable Roofs under Transient Wind: A Comparison between Time Domain and Frequency Domain Approaches", Tsinghua Science & Technology, 2008, Vol. 13, No. S1, pp. 53-57.
[8]   Soares, Jr. D., and Mansur, W.J., "A Frequency-domain FEM Approach Based on Implicit Green's Functions for Non-linear Dynamic Analysis", International Journal of Solids and Structures, 2005, Vol. 42, No. 23, pp. 6003-6014.
[9]   Uematsua, Y., Kuribaraa, O., Yamadab, M., et al., "Wind-induced Dynamic Behavior and Its Load Estimation of a Single-layer Latticed Dome with a Long Span", Journal of Wind Engineering and Industrial Aerodynamics, 2001, Vol. 89, No. 14-15, pp. 1671-1687.
[10]   Thai, H.T. and Kim, S.E., "Nonlinear Inelastic Time-history Analysis of Truss Structures", Journal of Constructional Steel Research, 2011, Vol. 67, No. 12, pp. 1966-1972.

[11]   Trombetti, T. and Silvestri, S., "On the Modal Damping Ratios of Shear-type Structures Equipped with Rayleigh Damping Systems", Journal of Sound and Vibration, 2006, Vol. 292, No. 1-2, pp. 21-58.

[12]   Zhang, Z.Q., Chen, Y., Su, G.X. and Zhu, X.G., "Analysis of Wind-induced Vibration Control of Long-span Space Structure", Advanced Materials Research, 2011, Vol. 255-260, pp.1204-1208.

[13]   Masters, F., Gurley, K., and Kopp, G.A., "Multivariate Stochastic Simulation of Wind Pressure over Low-rise Structures through Linear Model Interpolation", Journal of Wind Engineering and Industrial Aerodynamics, 2010, Vol. 98, No. 4-5, pp. 226-235.

[14]   Karmakar, D., Ray-Chaudhuri, S. and Shinozuka, M., "Conditional Simulation of Non-Gaussian Wind Velocity Profiles: Application to Buffeting Response of Vincent Thomas Suspension Bridge", Probabilistic Engineering Mechanics, 2012, Vol. 29, pp. 167-175.

[15]   Owen, J.S., Eccles, B.J., Choo, B.S. et al. "The Application of Auto–regressive Time Series Modeling for the Time-frequency Analysis of Civil Engineering Structures", Engineering Structures, 2001, Vol. 23, No. 5, pp. 521-536.

[16]   Soares, D. and Mansur, W.J., "A Time Domain FEM Approach based on Implicit Green's Functions for Non-linear Dynamic Analysis", International Journal for Numerical Methods in Engineering, 2005, Vol. 62, No. 5, pp. 664-681.

[17]   Kim, S.E., Kim, Y. and Choi, S.H., "Nonlinear Analysis of 3D Steel Frames", Thin-Walled Structures, 2001, Vol. 39, No. 6, pp. 445-61.

[18]   Davenport, A.G., "The Relationship of Wind Structure and Wind Loading", Proceeding of the Symposium on Wind Effect on Building and Structures, Vol. 1, London, 1965, pp. 54-102.

[19]   Iwatani, Y., "Simulation of Multidimensional Wind Fluctuations having any Arbitrary Power Spectra and Cross Spectra", Journal of Wind Engineering, 1982, Vol. 11, pp. 5-18 [in Japanese].

[20]   Isyumov, N., "Alan G. Davenport's Mark on Wind Engineering", Journal of Wind Engineering and Industrial Aerodynamics, 2012, Vol. 104-106, pp. 12-24.

[21]   He, Y.J., Zhou, X.H. and Wang, H.S., "Numerical Simulation of Wind Speed on Super-long-span Roof Structures", Journal of Hunan University (Natural Sciences), 2008, Vol. 35, No. 9, pp. 1-5 [in Chinese].

[22]   Jakobsen, J.B., Andersen, T.L., Macdonald, J.H.G., Nikitas, N., Larose, G.L., Savage, M.G. and McAuliffe, B.R., "Wind-induced Response and Excitation Characteristics of an inclined Cable Model in the Critical Reynolds Number Range", Journal of Wind Engineering and Industrial Aerodynamics, 2012, Vol. 110, pp. 100-112.

[23]   Chen, F.B., Li, Q.S., Wu, J.R. and Fu, J.Y., "Wind Effects on a Long-span Beam String Roof Structure: Wind Tunnel Test, Field Measurement and Numerical Analysis", Journal of Constructional Steel Research, 2011, Vol. 67, No. 10, pp. 1591-1604.

[24]   Uematsu, Y., Yamada, M., Inoue, A. and Hongo, T., "Wind loads and Wind-induced Dynamic Behavior of a Single-layer Latticed Dome", Journal of Wind Engineering and Industrial Aerodynamics, 1997, Vol. 66, No. 3, pp. 227-248.

[25]   Lu, F., Lou, W.J. and Sun, B.N., "Wind-induced Dynamic Response and Wind Load Factor for Long-span Flat Roof Structures", Engineering mechanics, 2002, Vol. 19, No. 2, pp. 52-57 [in Chinese].